Functionalized photochromic surfaces switched by organic light-emitting diodes

Dissertation

zur Erlangung des akademischen Grades
Doktor der Ingenieurwissenschaften
(Dr.-Ing.)
der Technischen Fakultät
der Christian-Albrechts-Universität zu Kiel

Matthias Bremer

Kiel
März 2018

1. Gutachterin:	Prof. Dr. Martina Gerken
2. Gutachter:	Prof. Dr. Rainer Adelung
Datum der mündlichen Prüfung	1. Dezember 2017

Hiermit versichere ich, dass ich die vorliegende Dissertation

Functionalized photochromic surfaces switched by organic light-emitting diodes

selbständig und ohne unzulässige fremde Hilfe angefertigt habe und dass ich alle von anderen Autoren wörtlich übernommenen Stellen wie auch die sich an die Gedankengänge anderer Autoren eng anlehnenden Ausführungen meiner Arbeit besonders gekennzeichnet und die entsprechenden Quellen angegeben habe. Weiterhin wurde die Arbeit bisher nicht im Rahmen eines Prüfungsverfahrens vorgelegt, jedoch wurden Teile in Form von Beiträgen in Fachzeitschriften und Tagungsbänden veröffentlicht sowie auf Konferenzen präsentiert. Diese Arbeit ist unter Einhaltung der Regeln guter wissenschaftlicher Praxis der Deutschen Forschungsgemeinschaft entstanden.

Matthias Bremer

Abstract

Photochromic molecules are reversibly switchable between two states with the help of light and allow the change of surface properties upon light irradiation. Potentially, these surfaces could be used for optically reconfigurable microfluidics and biosensors. Currently, lasers, mercury vapor lamps or light-emitting diodes (LEDs) are employed for the switching of photochromic molecules. This work describes the development of photo-switchable surfaces based on the two most common photochromic molecules. Additionally, these surfaces are excited with thin organic LEDs (OLEDs). With this combination an intelligent and programmable surface is realizable.

Here, a flexible PDMS copy of a lotus leaf covered with a single molecule layer of azobenzenes enables a 200 times higher relative transparency switching for a 355 nm laser beam compared to a flat glass substrate. Thereby a simple spatially resolved mapping of the azobenzene state on the surface becomes possible. A reversible contact angle switching between 138° and 95° is achieved with a non-covalently bound spiropyran layer on a candle soot surface. Then, a blue OLED is designed and fabricated that possesses a radiant flux of up to over 10 mW/cm². It is used to switch both photochromic surfaces. With the aim to increase the switching speed, the light outcoupling from OLEDs is enhanced. Tetrapodal zinc oxide particles are used to couple out trapped substrate modes. In order to use many OLEDs efficiently next to each other for the switching of a photochromic layer, it is necessary to direct the light of their usually more Lambertian emitting profile. For this, optical gratings are integrated into OLEDs. Here, it is shown how the change of emitter position, refractive index contrast and absorption increase the resonances of these gratings. In addition, grating effects on a fully flexible PDMS substrate are investigated and the first goniometric electroluminescene measurement of an OLED with an integrated multi-periodic grating is presented.

Kurzfassung

Photochrome Moleküle lassen sich mit Hilfe von Licht reversibel zwischen zwei Zuständen schalten und ermöglichen dadurch die Änderung von Oberflächeneigenschaften. Dies könnte zur Entwicklung von optisch konfigurierbaren Mikrofluidiken und Biosensoren genutzt werden. Bisher kommen für das Schalten photochromer Moleküle Laser, Quecksilberdampflampen oder Leuchtdioden (LEDs) zum Einsatz. Diese Arbeit beschreibt die Entwicklung von photoschaltbaren Beschichtungen auf Basis der beiden gängigsten photochromen Moleküle. Zusätzlich werden diese Schichten mit organischen LEDs (OLEDs) angeregt. Durch diesen Integrationsschritt lässt sich eine „intelligente“ und programmierbare Oberfläche erzeugen.

Eine mit einer einfachen Azobenzol-Molekül-Schicht versehene Kopie eines Lotusblattes aus flexiblem PDMS erlaubt hier ein um den Faktor 200 verstärktes Schalten der relativen Transmission eines Laserstrahles mit 355 nm Wellenlänge gegenüber einem glatten Glassubstrat, welches ebenfalls funktionalisiert wurde. Dadurch wird eine einfache Kartierung der Azobenzolzustände auf der Oberfläche möglich. Eine reversible Kontaktwinkelschaltung zwischen 138° und 95° wird mit nicht-kovalent aufgebrachten Spiropyranen auf Kerzenrußoberflächen erzielt. Im Anschluss wird eine blaue OLED designt und hergestellt, die eine Strahlungsleistung von bis zu über 10 mW/cm² aufweist. Beide Oberflächen werden mittels dieser OLED geschaltet. Mit dem Ziel einer Steigerung der Schaltgeschwindigkeit wird versucht, die Lichtauskopplung aus OLEDs zu erhöhen. Für die Auskopplung gefangener Substratmoden werden tetrapodale Zinkoxidpartikel verwendet. Um später möglichst viele OLEDs unter einer photochromen Schicht nebeneinander betreiben zu können, ist es zudem notwendig, deren eher Lambertsches Abstrahlprofil zu richten. Dafür eignen sich in OLEDs eingebrachte optische Gitter. Hier wird mittels verschiedener Experimente dargelegt, wie sich die Resonanzen der Gitter durch Veränderung von Emitterposition, Brechungsindexkontrast und Absorption verstärken lassen. Des

Weiteren wird der Gittereffekt in OLEDs auf flexiblen PDMS untersucht und zum ersten Mal eine goniometrische Elektrolumineszenzmessung einer OLED mit einem integrierten multiperiodischen Gitter gezeigt.

Scientific publications

Journal articles

M. Bremer, C. Kallweit, A. F. K. Iwers, M. Gerken, "An Optically Programmable Surface Realized with Azobenzene-Functionalized Lotus Leaf and OLEDs", Accepted in IEEE Photonics Technology Letters, Feb. 2018, DOI: 10.1109/LPT.2018.2811041.

M. Bremer, R. Reinke, B. Hesseler, M. Taale, D. Ingwersen, S. Schwarzer, C. Selhuber-Unkel, and M. Gerken",Non-Covalent Spiropyran Coatings for Photo-Induced Wettability Switching", Hindawi Journal of Nanomaterials Vol. 2017, 6498601, 2017.

C. Kallweit, **M. Bremer**, D. Smazna, T. Karrock, R. Adelung, M. Gerken, "Photoresponsive hierarchical ZnO-PDMS surfaces with azobenzene-polydopamine coated nanoparticles for reversible wettability tuning", Vacuum Vol. 146, pp. 386-395, 2017.

Conference presentations

H. Lüder, **M. Bremer**, and M. Gerken, "Simulation of nanostructured emission layers for tailoring the angular radiation pattern of OLEDs," ICEAA, Verona (Italy), pp. 1871, 2017.

C.Kallweit, R. Adelung, **M. Bremer**, M. Gerken, T. Karrock and D. Smazna "Effect of deposition process of photoresponsive nanoparticles and substrate choice on wettability properties" Euro Intelligent Materials 2017, Kiel (Germany) 2017.

M. Bremer, "OLEDs for Functional Devices – More than a Display Technology", Hannover Messe, Hannover (Germany) 2017.

C. Kallweit, **M. Bremer**, T. Karrock, M. Gerken, "Nanoparticle-enhanced photoresponsive surfaces for wettability switching in integrated systems", Symposium D: Nanomaterials - electronics & -photonics E-MRS Fall Meeting, Warsaw (Poland) 2016.

M. Bremer, C. Kallweit, A. Iwers, M. Köpke, M. Gerken, "Switching azobenzene-functionalized surfaces with organic light-emitting diodes", SPIE Photonics West, San Francisco, CA (United States) 2016.

M. Bremer, N. Beck, H. Lüder, M. Gerken, "Organic Light-Emitting Diodes with Multi-Periodic Extraction Gratings", Light Energy and the Environment Congress - SOLED, pp. DTu2D.4, Suzhou (China) 2015.

M. Bremer, J. Schmalz, T. Karrock, M. Gerken, "Photonic crystals for flexible OLEDs", Thinface Summer School, Alsion Sonderburg (Denmark) 2014

Conference poster

M. Bremer, A. Cojocaru, I. Hölken, I. Paulowicz, M. Köpke, R. Adelung, H. Schmidt-Niepenberg, and M. Gerken, "Tetrapodal ZnO Particles for Substrate Mode Scattering in Flexible Organic Light-Emitting Diodes", Light Energy and the Environment Congress - SSL, , pp. JW4A.8, 2016, Leipzig (Germany) 2016.

Students advised

Parts of the presented results in Chapter 4, 6 and 7 have been generated in the following Bachelor and Master theses that were supervised by me.

Bachelor thesis:

[1] **Lazaros Sotiriou**,
Vorrichtung zur Bestimmung von Oberflächenkontaktwinkeln bewegter Tropfen

Master theses:

[2] **Julius Schmalz**,
Herstellung und Charakterisierung nanostrukturierter OLEDs auf flexiblem Substrat

[3] **Andre Fritz Klaus Iwers**,
Blue OLEDs with integrated spectral filter

[4] **Melanie Storr**,
Experiments for embedment of tetrapodal zinc oxide particles in organic light emitting diodes

[5] **Nicolai Beck**,
Charakterisierung und Optimierung von Auskoppeleffekten multiperiodisch strukturierter Organischer Leuchtdioden

[6] **Ruprecht Reinke**,
Schalten photochromer Moleküle auf strukturierten Oberflächen mittels organischer Leuchtdioden

[7] **Mesut-Ömür Özden**,
Absorption und Auskopplung in multiperiodisch nanostrukturierten organischen Leuchtdioden

External Master thesis

[8] **Rico Kelz**, Ferdinand-Braun-Institut Berlin,
Degradation von UV-B LEDs

Acknowledgements

The research results presented in this thesis were generated since April 2013 and were mostly financed by the European Research Council within the project "Photosmart" (Starting Grant Agreement 307800).

I would like to thank Prof. Dr. Martina Gerken for giving me the chance to prepare my doctoral thesis within her group, as well as for her advice and support.

I am grateful for the technical support by Markus Köpke, who helped me a lot with the service of the evaporation system and the OLED production, especially during the last two years. Special thanks are also going to my other two colleagues whom I shared my office with: Dr.-Ing. Sabrina Hein (née Jahns) and Dr. Christine Kallweit. Thanks for all your help and advice! Moreover, thanks to all three for being such wunderful "officemates".

Very important was the work of my fantastic students listed the page before and I am thankful for the help of all involved research assistants: Gordon Axnick, Frauke Block, Marlena Draheim, Ron-Marco Friedrich, Ursula Krabbe, Leon Pohl, Christian Renn, Karolina Wilma and Danbi Yoo.

Additional thanks are going to my other collogues of the group for Integrated Systems and Photonics for their help and useful discussions: Prof. Dr.-Ing. Jost Adam, Hendrik Block, Melanie Bork, Jülf Buschmann, Torben Karrock, Hannes Lüder, Dr.-Ing. Philipp Metz, Moritz Paulsen, Sigrid Thielbörger and Dr.-Ing. Daniela Bechtold (née Threm).

Further, I would like to acknowledge the support of the cleanroom (Kieler Nano Labor) team, Dr. Michele Holz (Organic Chemistry, Kiel University), Dr.-Ing. Sören Gutekunst, Dr. Britta Hessler, Mohammadreza Taale, Prof. Dr. Christine Selhuber-Unkel (all four from the group for Biocompatible Nanomaterials, Kiel University),

Prof. Dr. Stefan Schwarzer (Leibnitz Institute for Science and Mathematics Education, Kiel; Now: LMU Munich), Daria Smazna (Functional Nano Materials, Kiel University), the botanical garden of Kiel University and the team of the Phi-stone AG, Kiel (former FUMT R&D; Dr. Ala Cojocaru, Dr.-Ing. Iris Hölken, Ingo Paulowicz).

I would like to thank Dr. Klaus Jäger (Helmholtz Zentrum Berlin) for measurements and helpful discussions and Dr. Dieter Ness (Joanneum Research, Austria) for the supply of their shark skin foil and additional advice.

Very special thanks are going to my good friend Inger-Marit Eriksen for all the corrections in terms of language and spelling!

Finally, I would like to acknowledge the mental support of my friends and my family, especially of my parents, my sister Margit and my aunt Dr. Hanna Förster (née Bremer).

Contents

Chapter 1.

Introduction

Stimuli responsive surfaces are able to change their physiochemical properties upon an external stimulus as, e. g., light, electrical potential, mechanical force, temperature or pH [1], [2]. Functional layers with photochromic molecules offer the possibility to alter surface properties reversibly by light irradiation [3]–[6]. This can be used for optical data storage, switching electrical currents, changing the adsorption of biomaterial, surface wettability etc. and could lead to the development of spatially controllable biosensors [7] and microfluidics [8].

Organic light-emitting diodes (OLEDs) are thin layers of unsaturated hydrocarbons sandwiched between two electrodes that are able to emit light. Their importance is currently growing a lot in the area of display technology and also gradually in lighting, where design aspects are important [9]. It has already been shown that they can be at least as efficient as fluorescent tubes [10] and possess unique features as being a very thin planar light source and can be fabricated on flexible [11], [12] or transparent [13], [14] substrates. Their current densities are lower compared to inorganic LEDs, which is the main reason for their lower luminance.

This thesis investigates photochromic surface functionalizations for technical applications. Currently, mostly laser, mercury vapor lamps or high-power LEDs are in use for switching photochromic molecules. As soon as a photo-switchable surface is fabricated on a transparent substrate, it becomes possible to excite the photochromic molecule layers through the substrate from the back. The main aim of this thesis is to combine this with an OLED irradiation, which then allows the fabrication of a "smart"

and programmable surface, such as depicted in Figure 1-1. The schematic shows a single-molecule layer on a structured surface, which is used to enhance the property changes of the photochromic molecules between their state *A* and state *B*. First, the molecules have to be brought into state *B*, which can be caused, e. g., by flashing with an ultraviolet (UV) LED. Parts of the surface can then be switched back to state *A* by an OLED on the other side of the substrate. To increase the spatial resolution of this programmable matrix, the emitted light of the OLED needs to be directed, because otherwise the molecules above the next OLED pixel could be switched as well.

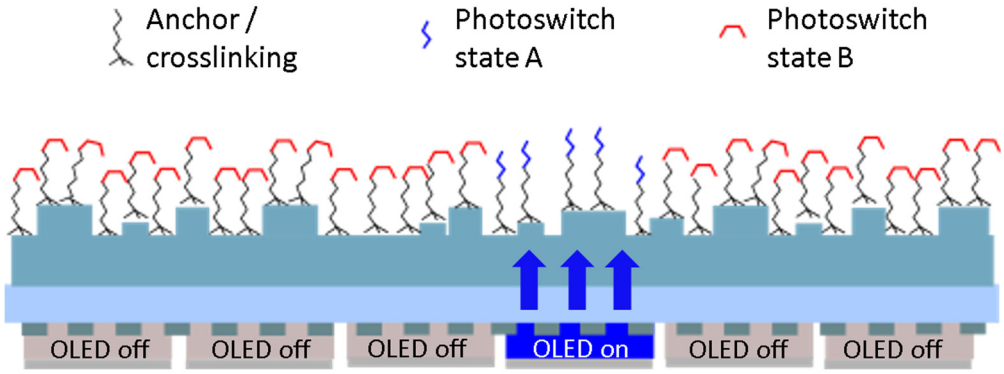

Figure 1-1: Schematic of device aimed for a photo-switchable surface with a structure that enhances physiochemical property changes of the molecule and an OLED with directed light emission caused by integrated gratings.

Photochromic molecules can also be integrated into OLED stacks or other devices based on organic semiconductors [15]–[17] to influence the current flow but this is not concerned for the present work.

Especially, the photo-control of the surface wettability is aimed here. Although there have already been presented a plenty of surfaces that are able to supply this feature [8], [18]–[20] , no surface has been available that was transparent at the same time. As follows, the development of a suitable functionalized surface was needed first. This brings us to the specifications of the photo-switchable layer: The most important properties are transparency and a low scattering. Ideally, the involved molecules can be switched very fast and induce a strong shift of a physical or chemical surface property. Unfortunately, the switching speed generally slows down when

photochromic molecules are transferred from a solution to a fixed position in a matrix or as single layer on a surface. The scattering cannot easily be circumvented because for amplifying dipole changes of a photochromic molecule micro- and nanostructuring is necessary. This will be further explained in Chapter 2. Here, mainly two different surface types are presented, which are schematically depicted in Figure 1-2 and base on the two most common photochromic molecules: azobenzenes and spiropyrans.

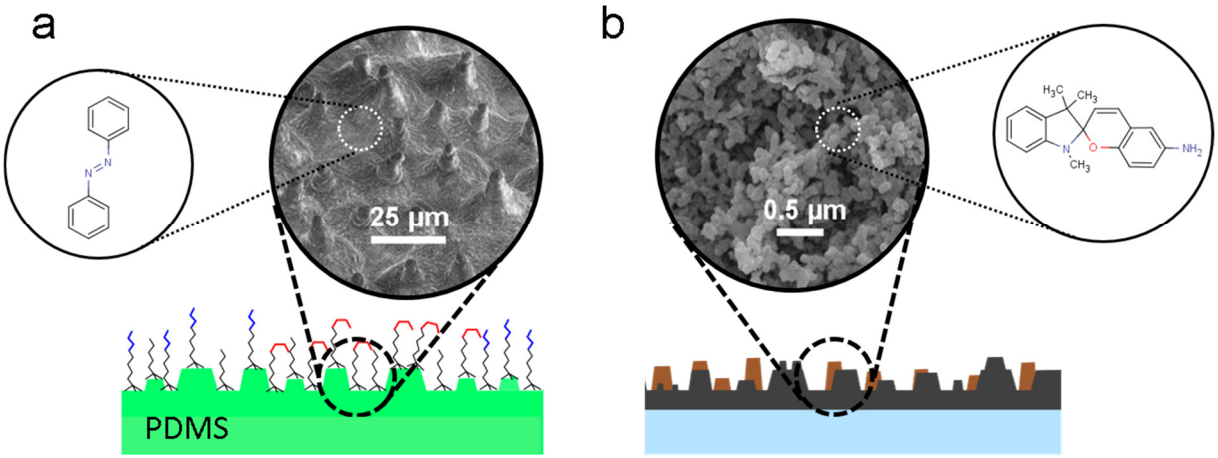

Figure 1-2: Surface with photo-switchable molecule layer based on either lotus structure with azobenzene (a) or candle soot with spiropyran (b).

The first surface is fabricated by combining the biomimetic approach of copying a lotus leaf structure into a flexible polymer with a covalently bound single molecule layer (Figure 1-2a) and the second one by candle soot and a non-covalent functionalization (Figure 1-2b). Both surface structures are well-known examples for being able to produce superhydrophobic surfaces [21]–[23] and are here engineered to become transparent as well. Additionally, they are covered with azobenzene and spiropyran molecules. The surface from Figure 1-2a is used for transparency switching and its spatial switching characteristics are studied intensively, while the one from Figure 1-2b enables the reversible contact angle switching of water droplets.

The switchable surfaces are then excited by OLEDs. Regarding these devices the most important parameters that are looked at here are: the radiant flux they provide, the fit of their emission spectrum to the spectral band in which the used

photochromophores can be switched effectively and a directed emission profile. To switch a photochromic molecule from its usually more stable state *A* to its state *B*, mostly UV light is needed. Unfortunately, organic UV emitters are currently not stable enough for technical applications [24], [25], which is why only blue emitters are used here to achieve the back switching from *B* to *A*.

A lot of the light generated inside the OLED is trapped in the substrate and in the organic layers. Only about 20 % are able to leave the device [26]. The outcoupling of substrate and guided modes are highlighted in two chapters at the end. Scattering particles can help to couple out trapped substrate modes as depicted in Figure 1-3a [27], [28] and here tetrapodal ZnO particles are employed for this.

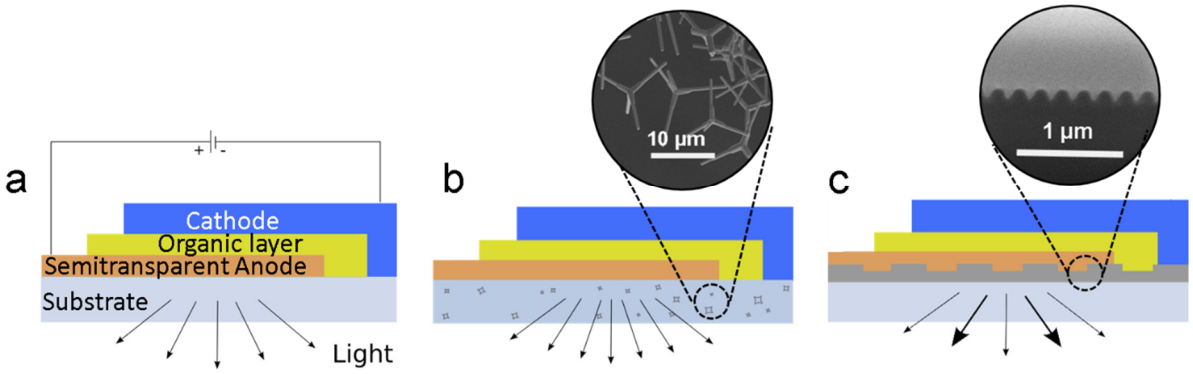

Figure 1-3: Light outcoupling from a (a) standard OLED: (b) substrate mode outcoupling with scattering particles and (c) directed outcoupling with integrated gratings (insets with SEM images by Phi-Stone AG, Kiel and Torben Karrock / Dr. Sabrina Jahns).

The emitted light of the OLED can also be directed into a specific direction by coupling out guided modes with integrated gratings in the OLED stack (Figure 1-3b) [29]. This concentrates the OLED light to smaller areas on the photo-switchable surface (Figure 1-1) and thereby the energy density increases, while the switching time should decrease.

Outline

The following part of this thesis provides the fundamental background needed for the experimental work shown in the later chapters. The topics range from organic and surface chemistry to the device physics of OLEDs. Chapter 3 describes covalent azobenzene functionalizations of a copied lotus leaf structure in polydimethylsiloxane (PDMS) and after that follows a chapter about non-covalent spiropyran functionalization of candle soot, which allows wettability switching. The excitation of the developed photo-switchable surfaces with OLEDs is then described in Chapter 5. Next, the substrate mode scattering of trapped OLED light by tetrapodal zinc oxide particles is covered. Then the guided mode outcoupling with 1D gratings is optimized by different experimental approaches in Chapter 7, which also provides specials as gratings in OLEDs on a fully flexible substrate and multi-periodic gratings in OLED stacks. Finally, the summary and conclusion follow in Chapter 8.

Chapter 2.

Fundamental background

This chapter will provide the reader with the basic background behind the functionalities of photochromic molecules and organic light emitting diodes (OLEDs). This includes important basics from organic chemistry and surface chemistry science. The chapter starts with a brief introduction to chromophores as both, photochromic molecules and organic semiconductors exhibit subgroups of them. Then, the two different photochromic molecules azobenzenes and spiropyranes are highlighted and afterwards general implications for surface functionalizations are given. As an important example for the switching of surface properties, the wettability switching is illustrated. The last part describes the function of OLEDs and loss mechanisms of these devices.

Chromophores

Parts of a molecule, which are responsible for its color, are called chromophores. They absorb light in a certain range of the spectrum and their perceived color will be the complementary color of what was absorbed. There are inorganic and organic chromophores. In both cases, the ability to absorb light depends on excitable electrons. In organic compounds, these electrons are coming from so-called conjugated π-bonds, which are a result of a deviation from the normal electron configuration of atomic carbon $1s^2 2s^2 2p^2$. Deviations from this configuration are hybridizations, which result from a linear combination of the wave functions of atomic orbitals. For carbon there are three possible hybrid electron configurations: sp^3, sp^2 and sp. The interesting π-bonds are only occurring in sp^2 and sp configurations. A prominent and simple example with a $2sp^2$ hybridization is the ethylene molecule where one $2s$ and two $2p$ orbitals are forming three $2sp^2$ orbitals. Together with the $2sp^2$ orbital of a neighboring carbon atom or a $1s$ orbital of a hydrogen atom they are forming a very strong σ-bonding. The non-hybrid $2p_z$ orbitals sit uprightly on the hybrid orbitals and create the π-bonds with a $2p_z$ orbital of the neighboring carbon atom. This bonding is weaker [30], [31].

In unsaturated systems, which possess π-bonds, the energy needed to excite an electron is lower (1.5 eV to 3 eV [32]), because the π orbital represents their highest occupied orbital (HOMO) and the excited antibonding state π* their lowest unoccupied molecular orbital (LUMO). In saturated systems without π-bonds the HOMO is represented by the σ orbital and LUMO by the σ* orbital. Due to the stronger bonding, the energy gap that has to be overcome is larger and for this reason, optical excitation in the visible range is not possible [33], [34]. Additionally, there are non-bonding (n) orbitals that do not contribute to the bond order. Transitions in form of $n \rightarrow \pi^*$ or $n \rightarrow \sigma^*$ are possible as well.

A system that is conjugated has got alternating double and single bonds. There, the p-orbitals of the double bond are able to overlap. Systems with only one double bond

or with several double bonds that have no or more than one single bond in between, are called isolated. Electrons can be highly delocalized in a conjugated system, which means that the probability of finding the electrons is spatially distributed over the whole σ-system [32], [33]. The longer the chain of the conjugated bonds, the longer gets the wavelength of the light that can be absorbed [30].

Photochromic molecules

Photochromism is characterized by a light-induced reversible change of the absorption spectrum of a molecule. It was first observed by FRITSCHE in 1867 [1] in a tetracene solution, which lost its orange color upon sun light irradiation. The term "photochromism" was first defined by HIRSHBERG in 1950 [35]. Since then there have been found many other molecules, which can undergo a structural change upon light exposure of a specific wavelength from a stable state *A* to a usually metastable state *B*. This process is here depicted in a potential energy diagram in Figure 2-1. Exciting a photochromic molecule from state *A* requires a higher energy than from state *B* and therefore a lower wavelength (typically in the UV range) is needed. After being excited, the photochromic molecule has got a chance of 50 % either to end up in state *B* or to fall immediately back to state *A*. The stability of state *B* depends on the height of the potential barrier (ΔE) between *A* and *B*.

One of the first commercial applications for photochromic molecules were sunglasses, which darken under the exposure to direct sun light and become clear under diffuse sun light. Nowadays, these molecules promise many new functionalities, in particular for, e. g., molecular motors, optical storage, switches for electrical current or ion transport through membranes and switchable surface properties [36], [37].

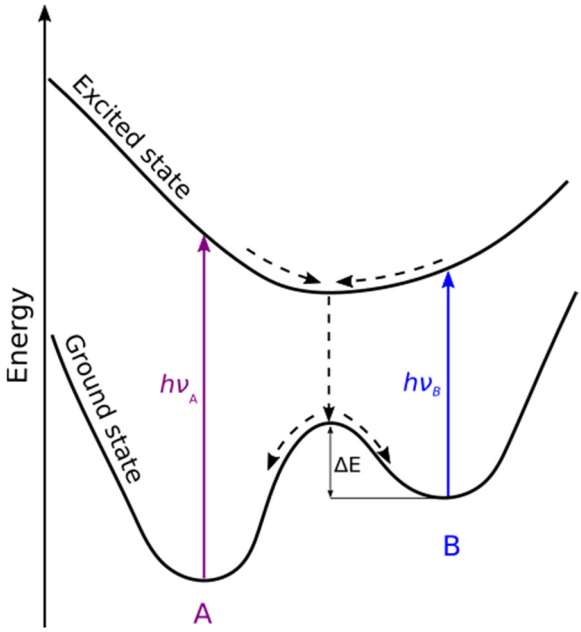

Figure 2-1: Potential energy diagram of photochromic molecules with state *A* and *B* (Adapted from [38]).

Azobenzene

The most studied photoswitches are the azobenzene and its derivatives. They exhibit a very simple molecular structure [6]. An azobenzene was first synthesized in 1834 by MITSCHERLICH [39] and DEMSELBEN [40] almost at the same time, but it took over 100 years until the reversible isomerization was first discovered by HARTLEY [41].

Azobenzene consists of two phenyl rings connected by a nitrogen double bond. Once its thermodynamically stable *trans* isomer is exposed to UV light, it converts to a meta stable *cis* state as depicted in Figure 2-2. The back switching can be achieved by visible light or may also occur spontaneously due to thermal energy.

With the change of the molecule state a change of the polarity occurs. While in *trans* state the dipole moment is around 0 D to 1.2 D, it switches to 3.1 D to 4.4 D in the *cis* configuration depending on the molecule substituents [6]. In addition, the distance between the two carbon atoms in *para* position lowers from 9.0 Å to 5.5 Å from the *trans* to the *cis*-isomer.

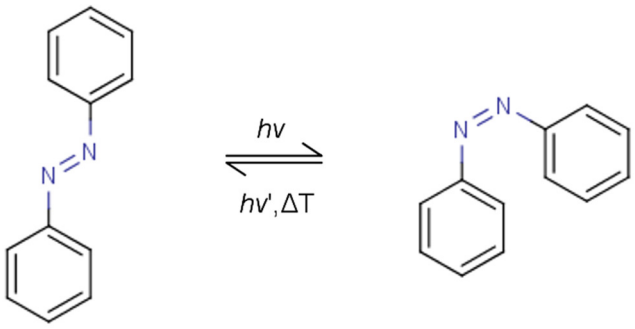

Figure 2-2: Chemical structure and isomerization of azobenzene (*trans* (left) and *cis* (right)).

The switching process itself was already described as rotation, inversion or a combination of these two mechanisms and depends also on substituting groups, solvents used or packaging on surfaces or in hosting materials [42], [43]. This fact is also valid for the switching time needed for the isomerization and it shall be additionally mentioned that in solvents the switching from *trans* to *cis* may happen within picoseconds and might then stay in this configuration for seconds or even days without exposure to visible light [44].

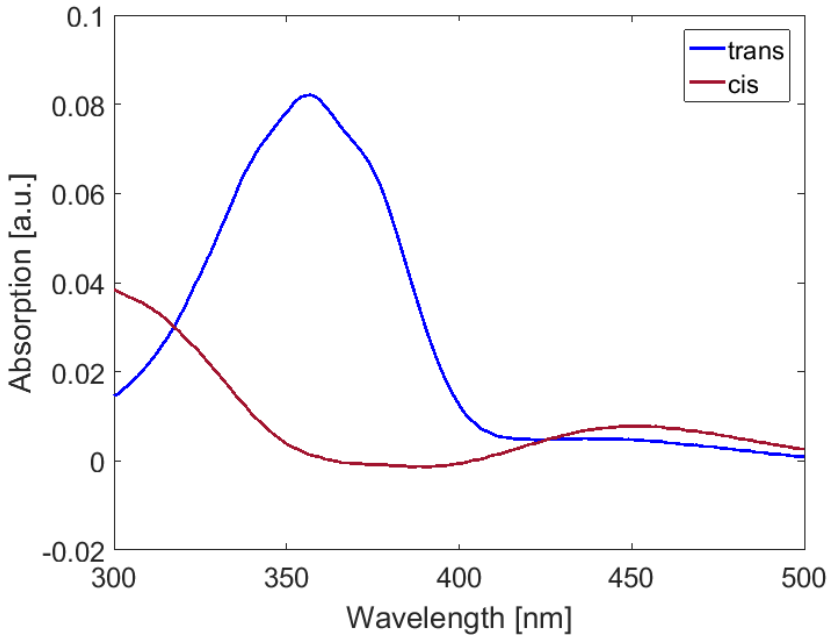

Figure 2-3: Absorption spectra of *trans* and *cis* (4'-Hexyl-phenyl)-[4(propyl-butoxy)-phenyl]-diazene (ether-2) [45] in PMMA (Sample fabrication by Dr. Christine Kallweit).

Figure 2-3 illustrates the absorbance difference of a *trans* and a *cis* azobenzene on an azobenzene derivative in a polymethyl methacrylate (PMMA) matrix. Most interesting are the π-π* transition band (here around 365 nm) and the n-π* transition band (here around 455 nm) as their positions also determine the spectral range of light that allows to switch the azobenzene between its isomers. The position of the transition bands depends strongly on substituting groups of the molecule and even strong red-shifts up to the green for the π-π* band have been shown [46], [47]. Unfortunately, with a redshift follows an intense reduction of the half-lives of the *cis* isomer [48].

Spiropyran

The next important photochromic molecule after azobenzene is the spiropyran. It is also characterized by a chemically simple structure and the advantage is that both isomers show very different properties [5]. Spiropyran consists of an indoline and a chromene moiety connected perpendicular to each other with a spiro junction. Once irradiated by UV light the chromene ring at the spiro junction opens and converts the spiropyran to merocyanin as shown in Figure 2-4. This isomerization induces a large shift of the dipole moment from 4.3 D to 17.7 D for merocyanin. The whole mechanism of this switching process is a bit more complex. If the reader is interested in this, the review by KLAJN [5] is recommended for further information.

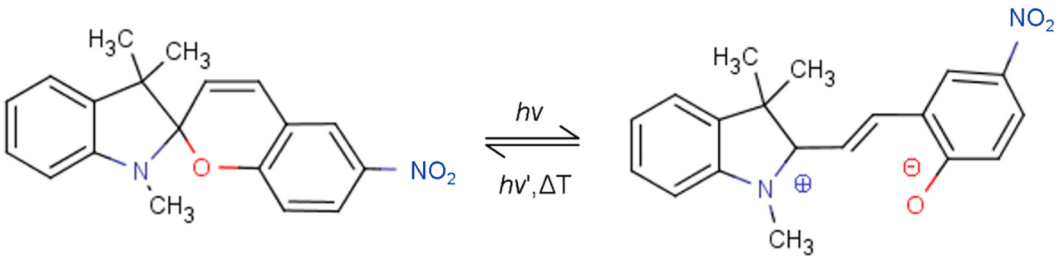

Figure 2-4: Isomerization of spiropyran (left) to merocyanin (right).

Merocyanin is metastable and returns back to spiropyran due to surrounding thermal energy. Also visible light can fasten this process in solvents, where its half-live is mostly in the range of seconds to minutes. Solvents including spiropyran are quite

transparent, but switched to merocyanin the solution gets an intensive color. The color depends strongly on the used solvent and varies from blue for toluene to almost red for ethanol [49].

Surface functionalizations

Properties of photochromic molecules were characterized in solvents intensively. This is usually easier, because the concentration of molecules is much better predictable. On surfaces the switching properties are more complicated and the density of molecules harder to determine. This is caused by the dependencies of the switching properties on the molecule density, which often results in steric hinderance. Some of the most important surface functionalization methods are described here, summarized under non-covalent and covalent surface bindings.

Non-covalent

Non-covalent are all surface functionalizations without complete chemical bonding to a surface. For the usage with photochromic molecules it is often argued that these functionalizations are less robust and they would be of less technical importance for this reason [5]. At this point, this fact shall not be completely disproved, but chapter 4 will show that non-covalently bound photochromic molecules can provide functionalities as well.

The bonding is caused by a physical adsorption to the surface [50]. Deposition methods based on solutions are drop casting, spin coating, doctor blade, dip coating, Langmuir-Blodgett and spray coating. In principle also a few deposition techniques without the use of a solution could be used for non-covalent molecule layers, as there are, e. g., Organic Vapor Phase Deposition (OVPD), Organic Molecular Beam Deposition and thermal evaporation.

Covalent

Covalently coupled molecules are bound by chemical adsorption to a surface and usually they thereby form monolayers. These are called self-assembled-monolayers (SAMs) and there are typically two major substrates for this, which are gold and silicon oxide based materials (e. g. activated glass, quartz and silicon surfaces). A SAM layer consist always of three substituting groups: The first one next to the substrate is the anchor, which is essential for the adsorption on the surface. Then follows a spacer group of individual length and at the end the functional head group. Functionalizations on gold can be easily obtained by mounting a molecule to a thiol, disulfites or sulfites and these anchor groups bind strongly to a gold surface. Due to a quick and easy preparation of the SAMs on gold, they have been extensively studied, especially for azobenzenes [37], [51]. On the other hand, gold absorbs a huge amount of energy and additionally induces surface quenching [52], which leads to a need for extremely long excitation duration by a strong power source as, e. g., a laser, to switch photochromophores. This does of course not come into agreement with the aim of using low power sources in technical applications and therefore this approach shall not be further investigated here.

Using silicon oxide based materials has the advantage of a high transparency (except for pure silicon) in the visible and partly also in UV range. Thus, much less power is needed for exciting the switching process of photochromic molecules and additionally these functionalizations are more stable. The anchor group for a chemical adsorption is in this case usually a silane, and nowadays there exists quite a large variety of them. These chemicals are able to bind themselves to free hydroxide groups on top of the oxide substrate. As a consequence, there are many free hydroxide groups needed on top of the surface. This can be achieved by a surface treatment with a strong acid or an oxygen plasma and is called “activation”. Additionally, this leads to a very hydrophilic surface and an adsorption of surface water, which is important for a well-ordered silane monolayer. Too much water during the silanization is instead

counterproductive, because of the risk of forming polysiloxanes, which reduce the quality of the monolayer. This is why this process has to be executed under inert atmosphere. In addition, the silane concentration and the time are critical parameters for the layer quality. It follows that many parameters have to be adjusted in order to form a suitable SAM with a silane, but once this is done, they are very stable.

There are also few other possibilities for the production of SAMs as, e. g., a so called "platform approach", which should allow a very easy functionalization [53]. On the other hand, this requires a much more complicated synthesis and would have had increased the cost for a first demonstrator device where photochromic molecules and OLEDs were combined.

Surface wettability

One surface property most wanted to be changed with photochromic molecules is the wettability. For that reason it will be explained here, how a droplet is formed on a surface. The contact angle (CA) ϑ is defined by the surface tension of the boundary layers between liquid and gas γ_{LG}, liquid and solid γ_{LS} and solid and gas γ_{SG}. This is schematically depicted in Figure 2-5.

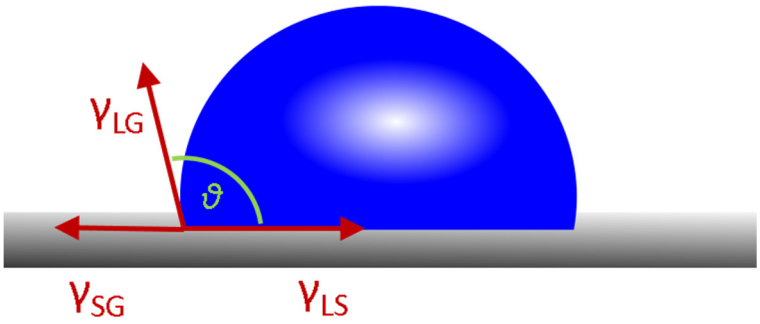

Figure 2-5: Schematic illustration of surface tensions at the three-phase contact line of a droplet on a solid surface (Adapted from [54]).

The relation of these parameters in equilibrium is described by Young's equation:

$$\cos\vartheta = \frac{\gamma_{SG} - \gamma_{LS}}{\gamma_{LG}} \qquad \text{(Eq. 2-1)}$$

In case $\vartheta > 90°$ the surface is called hydrophobic or oleophobic and if $\vartheta < 90°$ it is called hydrophilic or oleophilic, depending on if it is a water or an oil droplet. The highest CA that water can achieve on a simply flat surface is 115.2° on a CF_3 terminated surface, resulting from a surface energy of 6.7 mJ/m², which is the lowest measured so far [55], [56]. Nevertheless, it is possible to achieve a much higher CA up to almost 180°, while complete 180° are actually not possible, because at this point there would be no contact between the droplet and the surface. Is the CA over 150° the surface is called superhydrophobic or superoleophobic and if the CA is close to 0° it is superhydrophilic or superoleophilic, respectively. The high CAs are possible due to an enhancement by surface roughness. Is the roughness very high and the surface tension low, a surface can be both superhydrophobic and superoleophobic, which is expressed by the term superamphiphobicity. The extreme opposite is called superamphiphilicity and requires a high surface tension combined with a high roughness. So, it means that changing the surface tension on a very rough surface should allow for very strong changes in wettability. Therefore, stimuli-responsive materials can be used, which can then be switched by light, solvents, electrical potential, magnetic field or a change of temperature or the pH value [1], [2], [18], [20]. Also a change of the geometrical structure of a surface allows for wettability switching [57], [58].

The most common and basic theories to describe the influence of the surface structure on the CA were described by WENZEL in 1936 [59] and CASSIE and BAXTER in [60]. In case of a Wenzel wetting mode, which is depicted in Figure 2-6 on the left, the liquid fills all holes and grooves of the structure. The result is an apparent CA ϑ_W that is influenced by the surface roughness factor *r* as follows:

$$\cos \vartheta_W = r \cos \vartheta \qquad \text{(Eq. 2-2)}$$

In this case the roughness factor can be seen as an amplifier for chemical properties of a surface and it means that if $\vartheta < 90°$, ϑ_W is lower and more hydrophilic and if $\vartheta > 90°$ the surface becomes more hydrophobic ($\vartheta_W > \vartheta$).

In the Cassie and Baxter mode the droplet sits like a fakir on a nail board on top of the structure and therefore air will be left in the recess of the structure. As a result, one fraction f_s of the droplet is in contact with the solid and the other one f_v with the vapor. With $f_s + f_v = 1$, $\vartheta_S = \vartheta$, and $\vartheta_C = 180°$ the apparent CA ϑ_C can be written as:

$$\boldsymbol{\cos \vartheta_C = -1 + f_S (\cos \vartheta + 1)} \qquad \text{(Eq. 2-3)}$$

An illustration of this wetting mode is also given in Figure 2-6. Sometimes this state is metastable, because an equilibrium is not reached and this means that the droplet will end up in the Wenzel state after some time. Other experiments showed that it is even possible to use pressure to force the droplet from Cassie-Baxter to the Wenzel state [61], and some even possess both or transition states [62]–[65].

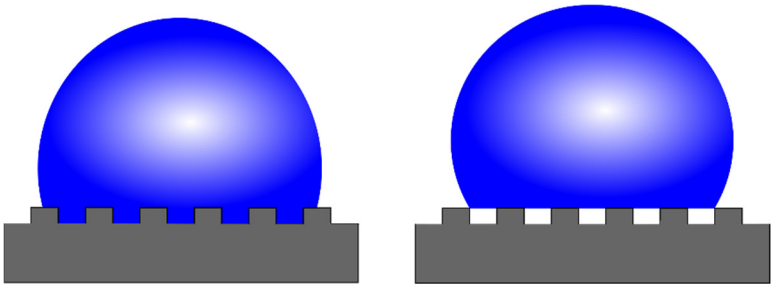

Figure 2-6: Illustration of Wenzel and Cassie-Baxter state (Adapted from [62]).

It should be mentioned that there is an ongoing discussion about the accuracy of the theories of the two described models [66]–[72]. Especially, the equation by Cassie and Baxter has often been criticized [73], [74]. The mostly shared view on this is that the Cassie equation is not ideal for all kinds of surfaces, but it still holds a strong relevance and is sufficient enough to understand most effects described in this thesis.

Measuring the contact angle

The measurement of CAs on a surface requires a camera for taking a picture of the droplet from the side, a small sample table, a background illumination to enhance the contrast at the droplet edges and a suitable dispenser for the liquid. All these components are commercially available in a complete system including also a software for analysis of the drop shape. For the results shown in this thesis an OCA 50 by

Dataphysics was used. To be analyzed, the drop is usually put carefully on the top of the solid, using the sessile drop method. Unfortunately, the CA can depend on the size of the droplet. If it is too small, evaporation will affect the shape of the droplet and therefore change the CA, and if it is too big, it will be influenced by the gravitational force. This force plays a strong role, especially if the diameter of the droplet becomes larger than the capillary length of the applied liquid [75]. Beneath this value, gravity can be neglected. Only in case of a very high CA, it becomes important again, because in case of a CA of 180° the pressure at the contact area would be infinite [54].

The capillary length, κ, is defined as follows:

$$\boldsymbol{\kappa} = \sqrt{\frac{\boldsymbol{\gamma_{LG}}}{\boldsymbol{\rho g}}} \qquad \text{(Eq. 2-4)}$$

where ρ is the density of the liquid and g the acceleration of gravity. The capillary length is in the millimeter range for most systems [75].

The drop shape has then to be analyzed with the help of mathematical fitting models, of which the circle, ellipse, tangential and Young-Laplace methods are the most common. The circle and the ellipse methods are easy to implement, but are only giving suitable results up to $\vartheta = 60°$. The tangential method instead is more accurate, if the taken photo provides a high resolution around the three-phase point. The most exact one is actually the Young-Laplace method, because it considers the gravity. Therefore, it is the method to be used for very hydrophobic surfaces.

Basic design criteria for superhydrophobic surfaces

The most important point, when designing structures to enhance the CA is that its scale has to be smaller than the capillary length, which is 2.7 mm for water. There are also a few other important points which should be considered:

- Pillars tend to form surfaces for easier sliding or rolling than holes, which is due to a lower solid surface fraction [63].

- Tall, sharp features increase the change of inducing bridging state, but weaken the surface against abrasion [63].

- Overlaid structures with multiple scale roughness are more effective to create more stable high contact angles, which has been proven theoretically [76] and experimentally [77].

- Single, small, length scale structures considerably less than the wavelength of visible light, are good for optical transparency [63].

- The base material can be chosen for its properties and then coated to render it hydrophobic if necessary [63].

Apart from these remarks different structures are possible. Some are shown in Figure 2-7. Many examples can already be found in the nature, e. g. on plant leaves (lotus, nasturtium, ivy, alchemilla, lupin etc.), on butterfly wings or on water spiders, and often these structures are simply copied or mimicked [78].

If now photochromic molecules can be put as a thin layer on top of such structures, it should in principle be possible to switch them from highly hydrophobic to hydrophilic. The back switching is hardly possible due to the problem that the liquid would have to be pushed out of the structure against gravity.

As not one of the structures shown in Figure 2-7 was fabricated into a transparent, they are all highly absorbing light. For the applications aimed in this theses they would have first to be engineered to become transparent. An additional problem is that surface functionalizations cannot be applied to all kinds of materials or structures.

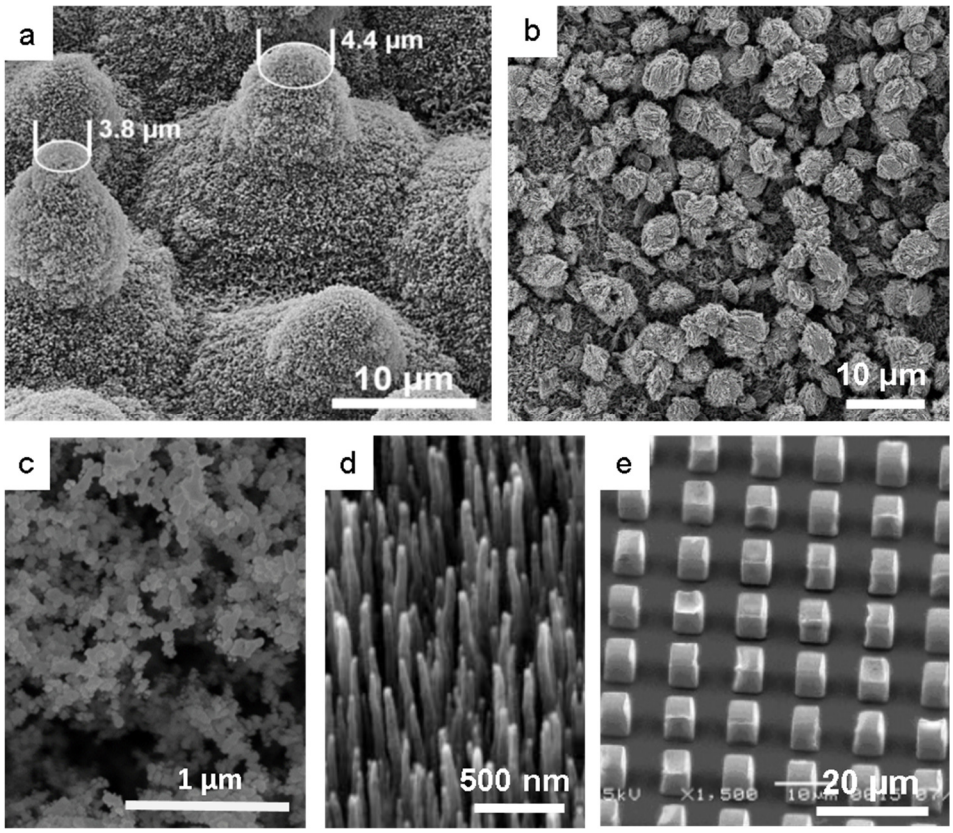

Figure 2-7: SEM images of different superhydrophobic surfaces, (a) lotus leaf with clearly visible wax tubules, adapted from [79]; (b) cupper etched by potassium persulfate and functionalized with lauric acid (Printed with permission of Ron Blonder, Weizmann Institute of Science); (c) candle soot; (d) Carbon nanotubes, adapted with permission from [80] Copyright 2005 EDP Sciences; (e) square pillars prepared with evaporation of Hyflon AD H80 solution on mold from, adapted with permission from [81] Copyright 2006 American Chemical Society.

Organic light emitting diodes (OLEDs)

Like the well-known light-emitting diode (LED), OLEDs are also thin-film devices which are able to emit light. The difference of these devices is that the inorganic materials of the LED stack are exchanged with organic semiconductors.

Organic semiconductors

Like the photochromic molecules, organic semiconductors can be assigned to a subgroup of chromophores. Their semiconducting properties are originating from delocalized π-electron systems with their HOMO and LUMO bands as described in the part about Chromophores in this chapter. These bands actually match to the valence and conducting bands in inorganic materials. Organic semiconductors possess the advantage of a designable energy band gap by chemical synthesis, and therefore the electronic and optical material properties can be changed according to one's needs. There are two different kinds of organic semiconductors: small molecules and conjugated polymers. This subdivision is important because they require different processes for their thin film fabrication. Due to their low molecular weight, small molecules can be thermally evaporated, which is up to now still the best controlled fabrication process for OLEDs. Using co-evaporation, even doped layers can be realized. Polymers consist of 10 to 100 000 monomers in a row and their long chains can be destroyed if exposed to higher a temperature. They have to be processed out of a solution employing methods as spin coating [82], ink-jet printing [83] or slot-die coating [84]. Ideally, electrons in polymers would be delocalized over the whole length of a molecular chain, but in reality, this only happens over a length of about 10 monomers [85]. For this reason, the intramolecular conductivity of the molecule is reduced. More about conductivity and general electronic properties can be found in the next part.

Electronic properties

Because the electronic properties of organic semiconductors are less important for this thesis, only the main points will be briefly covered in this part. Readers with further interest in this topic may have a look into [33]. The electronic properties are divided into charge carrier injection, transport and energy transfer.

The current in organic semiconductors can be either injection limited or space charge limited, while the first ones can be neglected once an operating voltage of the device is reached. The current injection is usually explained by a mixture of thermionic emission and Fowler-Nordheim tunnel injection in combination with a reduced Schottky barrier by an applied field [86]. The transfer from metal to organic semiconductor can then be described as a hopping motion [87]. This denotation came from the tunneling processes involved in this case. Thermal energy helps to overcome molecule and conjugation boundaries by non-coherent transfer events [88]. This hopping transfer is a rather slow process and is additionally slowed down by an amorphous material structure. Although the mobility of carriers can be quite high in crystalline organic semiconductors with values around 5 cm^2/Vs for pentacene or antacene [89], the mobility for amorphous materials that are used in OLEDs is very low and in the range of 10^{-8} cm^2/Vs to 10^{-1} cm^2/Vs [90]. This disadvantage can be partly overcome by doping which nowadays is often used for transport layers in OLEDs and organic solar cells [91]. The mobility of holes is much higher in organic semiconductors because the electrons can easily fall into traps [33].

The charge carrier transport is usually described by the model of Bässler [33], [88] with a Gaussian distribution of the localized states on the HOMO and LUMO levels. The transport is then performed in form of hopping motion, is increasing with higher temperatures and guidance occurs by the applied field (Poole-Frenkel theory).

In doped layers, two energy transfer processes are important: the Förster resonant energy transfer (FRET) and the Dexter energy transfer. The FRET is a nonradiative process and requires a dipole overlap of the involved molecules and an overlap of the emission and the absorption spectra. Its distance reaches from three to four

nanometers and the process retains the spins of each exchanged charge carrier. The Dexter transfer appears in a shorter range (1 nm) and preserves only the overall spin.

Optical properties and radiative decay processes

The optical properties of an organic semiconductor are also determined by the HOMO and LUMO levels. In case there is no electron in the LUMO and the HOMO is fully occupied, this is defined as ground state S_0. Once an electron is excited, it depends on the spin of the electron which state is achieved. If the overall spin of both electrons is zero, which means that the excited electron possesses an opposite spin compared to the spin in the HOMO, it is the singlet state S_n. On the other hand, the chance is higher to get an overall spin $S = 1$. There are three different forms of this case and all are known as triplet states (T_n). Triplet states must have an antisymmetric wave function. As the square of the wave function gives the probability of finding the electrons, they must be more far away from each other than in for $S = 0$. As follows, the energy of the triplet states is lower than the one of the singlet states. Three different possibilities exist to excite an electron: photon absorption, electron injection and chemical reactions. After the excited state is achieved, the electron relaxes back to the ground state, which can occur together with emission of a photon (radiative decay). Depending on the excitation form the following luminescence is called either photoluminescence, electroluminescence or chemiluminescence. Differences are also made between the radivative decay from singlet and triplet states. The photon emission from $S_1 \rightarrow S_0$ is called fluorescence and is a fast decay that happens within nanoseconds due to the short life time of the S_1 state. The lifetime of the T_1 state is much longer and can last from microseconds to seconds [92]. The emission from $T_1 \rightarrow S_0$ is called photoluminescence. Both processes are depicted in Figure 2-8.

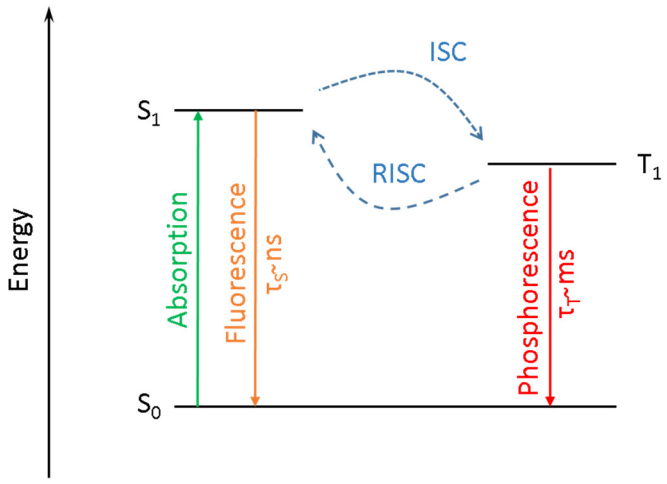

Figure 2-8: Energy levels of singlet and triplet states and radiative decay processes; Intersystem crossing (ISC) and reverse ISC (RISC) require special conditions (Adapted from [93]).

Photoluminescence and transitions between singlet and triplet states are spin-forbidden. This means that triplet states usually decay nonradiatively and just produce heat. With the help of spin-orbit interaction, this quantum mechanical rule can be compassed [94]–[96]. The higher the spin-orbit interaction is, the more intersystem crossing (ISC) occurs and the more singlets are converted to triplet states. Thereby more phosphorescence is possible. This can be achieved with heavy metal atoms inside the organic molecule complex [95]. With a very careful design of organic molecule, it is also possible to realize a reverse intersystem crossing (RISC) from triplet to singlet states. In order to achieve this, the energy gap between S_1 and T_1 level has to be smaller than 100 meV and a radiative decay rate of over 10^6 s^{-1} is needed [97]. This leads to more fluorescence by converted triplets and is called thermally activated delayed fluorescence (TADF).

Now we will have a closer look on the spectral properties of organic semiconductors. Figure 2-9 shows a Morse plot with the potential wells of the ground state S_0 and excited state S_1 of an organic material. Each state possess different vibrational levels. A suitable photon can excite an electron from S_{0-0} to one of the vibrational states of S_1. In case it is not already there, the electron falls within 10^{-13} s to the lowest level of the excited state in a nonradiative process [92]. From there the

electron can go back to a vibrational level of the ground state by emitting a photon. The energy of the emitted photon is lower than of the absorbed one, which is known as Stokes-shift.

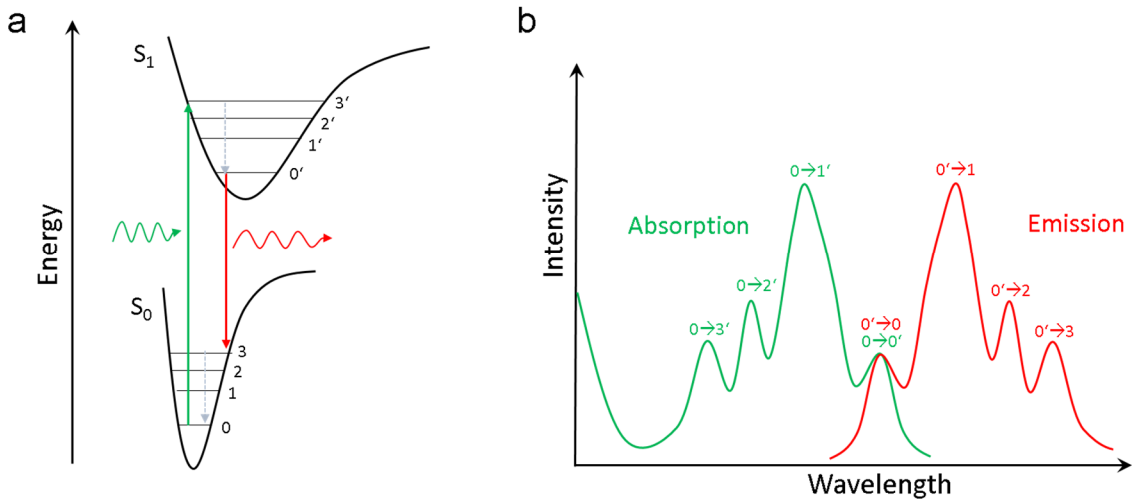

Figure 2-9: Absorption and emission processes (here fluorescence) schematically illustrated with (a) the Morse curve and (b) typical resulting spectra (Adapted from [98]).

Figure 2-9b depicts a schematic of the resulting absorption and emission spectra. The mirror-image relationship is typical for organic compounds.

The OLED stack

In the following paragraph, the function of the OLED device is explained. In Figure 2-10 a very simple OLED stack is shown. The OLED consists of an organic light emitting layer sandwiched between two electrodes (anode and cathode), where at least one of them has to be semitransparent. In this case, it is the anode which is partly transparent and the device emits light through the substrate material once a sufficient current is supplied to the electrodes. This is called a bottom-emitting device. OLEDs not emitting through the substrate but in the opposite direction are called top-emitting. The size of the device can be freely chosen from μm^2 to m^2 depending on your available coating devices. The most used substrate material is glass. In addition, the use of partly flexible thin glass on plastic became more important in the recent years. Glass cannot

be easily waived as it is still the best transparent barrier towards oxygen and humidity from the surrounding air, which organic semiconductors are highly sensitive to. For the same reason an encapsulation is needed on top of the OLED stack.

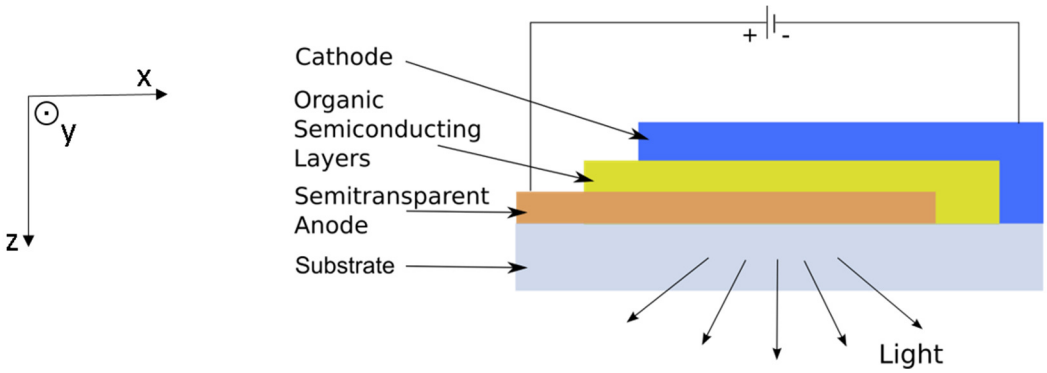

Figure 2-10: Schematic of basic OLED stack without encapsulation (Adapted from [32]).

A typical material for the anode is indium tin oxide (ITO) because it is conductive and transparent, which is a rare combination. Additionally, its low work function allows an efficient injection of holes into the HOMO level of the organic semiconductor. This conductive and transparent solid has been popular in the display technology since many years. It just has two major disadvantages: It is expensive and does not fulfill the requirements for the upcoming trend of flexible devices because it is too brittle. Classically, for the cathode a metal is selected, mostly together with a material for the optimization of its work function as, e. g., lithium fluoride (LiF) [99]. By that, a lower driving voltage and higher efficacy can be obtained. As depicted in Figure 2-11 there is not only the organic emitting layer. Many other organic layers were introduced within the last 25 years of OLED research in order to improve the current injection and overall efficacy of the device. Nowadays, you can find hole transport (HTL), electron transport (ETL), electron blocking (EBL) and hole blocking (HBL) layers in the OLED stack [100].

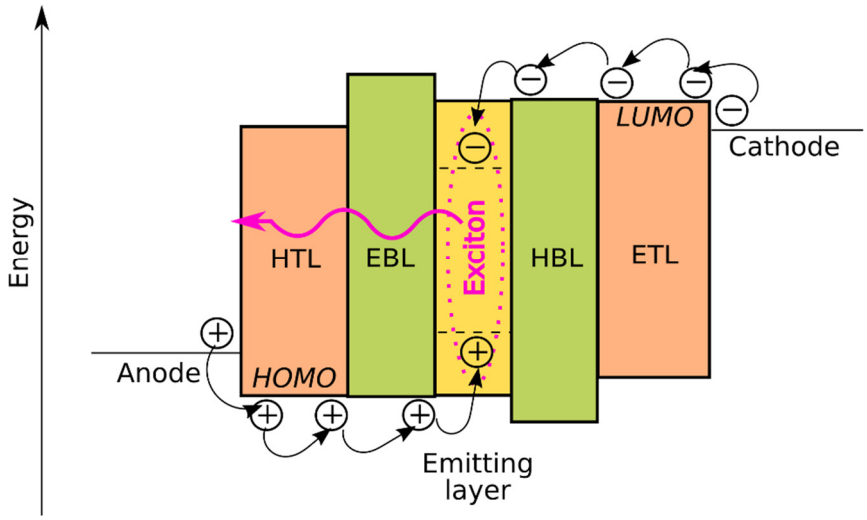

Figure 2-11: Schematic of OLED function with charge carrier transport and exciton formation (Adapted from [98]).

After the holes and electrons are transported to the emitting layer they form so-called Frenkel excitons, which are nothing else than electron-hole pairs that stick together due to their Coulomb attraction. Depending on the spin of both carriers, the hole and the electron are then recombining and eventually creating a photon. The probability for the photon generation at this point is called the quantum yield η_q. In case of a simple fluorescent emitter as, e. g., (8-hydroxyquinoline)-aluminuim (Alq_3) the quantum yield is maximum 25 % because only singlet states can cause fluorescence and the chance for the exciton to be a triplet is three times higher. This factor is also intensively influencing the internal quantum efficiency (IQE), which is the total number of photons generated divided by the number of electrons injected [101]. It is given by:

$$\boldsymbol{\eta_{int} = \gamma r_x \eta_q} \qquad \text{(Eq. 2-5)}$$

where γ is the charge carrier balance factor and r_x the exciton generation rate. In order to retain the quantum yield from severe reductions, the emissive layer has to be kept away from the electrodes and impurities of the material have to be reduced. Otherwise non-radiative fluorescence quenching might occur [102].

Out-coupling efficiency and loss mechanisms

The ratio of the total number of emitted photons from the device to the number of electrons injected is the external quantum efficiency (EQE). It includes the IQE and the efficiency of the light out-coupling η_C:

$$\boldsymbol{\eta_{ext} = \eta_{int}\eta_C} \quad \text{(Eq. 2-6)}$$

For the OLED characterization a few more efficiencies are important and in general use. This variety is often causing confusion and in case of any uncertainty or deeper interest in this topic it is strongly advised to have a look into [103]. In a quick sum up, there are the luminous power (luminous flux divided by input power), luminance (luminous intensity per square) and the wall plug efficiency (output power divided by input power). As the first two include a weighting with the photoptic function of the human eye, they are important when dealing with perceived brightness for humans. On the other hand, these values might give a less reliable interpretation and for the usage as light source in sensors or for the excitation of photochromic molecules the wall plug efficiency $\eta_{W/W}$ is more suitable.

To get a quick rough estimate of a typical value for η_C one can use a simple model from ray optics and get [26], [104]:

$$\boldsymbol{\eta_C = \frac{1}{2n^2}} \quad \text{(Eq. 2-7)}$$

where n is the refractive index of the OLED stack. Considering typical values for the refractive index of the OLED stack that lie between 1.6 and 1.8, one ends up with out-coupling efficiencies of just 15 % to 20 %. This makes clear that the main reason for the low out-coupling efficiency is the high refractive index of the involved materials in the device. Thereby, a wave guiding layer is produced in which most of the light is trapped. One big part is not able to leave the substrate and another gets stuck in guided modes of the organic stack. A small part is simply absorbed and then there are the so-called surface plasmon polaritons (SPPs). The influence of each effect depends on the layer thickness, the position, type and orientation of the emitter [26], [105], [106] .

Substrate losses

The thickness of the substrate is in most cases much larger than the wavelength of visible light. For this reason, normal geometrical optic can be used to describe the substrate losses. The effect is comparable with the guiding of light in simple glass fibers for data transmission where it is desired—but here it is not. Due to the higher refractive index of the substrate (for glass $n_{\mathrm{glass}} \approx 1.5$) it comes to a total reflection at the substrate-air interface. By employing Snell's law, the minimum angle for the total reflection can be calculated. The higher the refractive index of the substrate, the more light will get stuck in the substrate.

Guided modes

Organic layers are much thinner and in the range of the wavelength of the produced photons. As the consequence, the rules of geometrical optic cannot be applied anymore. Now the solutions of Maxwell's equation have to be considered. These solutions are called "modes" and do not change their shape during propagation [107]. From the Maxwell's and materials equations one can get a wave equation for the electric field $\vec{E}(\vec{r})$ which then leads to the Helmholtz equation that delivers stationary solutions for the electric field for an isotropic, linear, homogeneous and time-independent material [98]:

$$\left(\Delta + \boldsymbol{n^2}\frac{\boldsymbol{\omega^2}}{\boldsymbol{c_0^2}}\right)\vec{\boldsymbol{E}}(\vec{\boldsymbol{r}}) = \boldsymbol{0} \qquad \text{(Eq. 2-8)}$$

where c_0 is the speed of light in vacuum. One gets then with the dispersion relation:

$$\boldsymbol{\omega^2} = \frac{\boldsymbol{c_0^2}}{\boldsymbol{n^2}}\vec{\boldsymbol{k}}^2 \qquad \text{(Eq. 2-9)}$$

where $\vec{k}$ is the wavevector, to elementary solutions of the Helmholtz equations for a forward (*f*) and backward (*b*) going wave:

$$\vec{\boldsymbol{E}}_{\boldsymbol{f}}(\vec{\boldsymbol{r}},\boldsymbol{t}) = \boldsymbol{E}_{\boldsymbol{f_0}}\boldsymbol{e}^{\boldsymbol{i}(\boldsymbol{\omega t}-\vec{\boldsymbol{k}}\vec{\boldsymbol{r}})} \quad \text{(Eq. 2-10)}$$

$$\vec{\boldsymbol{E}}_{\boldsymbol{b}}(\vec{\boldsymbol{r}},\boldsymbol{t}) = \boldsymbol{E}_{\boldsymbol{b_0}}\boldsymbol{e}^{\boldsymbol{i}(\boldsymbol{\omega t}+\vec{\boldsymbol{k}}\vec{\boldsymbol{r}})} \quad \text{(Eq. 2-11)}$$

which are orthogonally polarized to the direction of $\vec{k}$. In a waveguide there can be two parts for both of these equations: The transverse electric mode (TE) where the electric field stands orthogonal on the wave vector $\vec{k}$ and the transverse magnetic mode (TM) where it is the magnet field. If one can find solutions for (Eq. 2-8) that fulfill the continuity condition for the electric and magnetic field at all of the material borders of the waveguide, this solution can be called a mode which exists at specific wavelength [98].

The emission of the dipoles is often plotted as a function of the (normalized) in-plane wavevector k_x/k_{EML}, where k_x is the x-component of the wavevector and k_{EML} the absolute value of the wavevector in the emitting layer [105]. An example for this is given in Figure 2-12. The shown power dissipation spectrum is wavelength dependent. If $k_x/k_{\mathrm{EML}} = 1$, it corresponds to the in-plane propagation of light in the bulk emitting layer. All the power in $k_x/k_{\mathrm{EML}} < k_{\mathrm{air}}$ is coupled out of the device and can be used. By integrating over this area, the outcoupling efficiency can be calculated. Then there are the substrate modes ($k_{\mathrm{air}} < k_x/k_{\mathrm{EML}} < k_{\mathrm{sub}}$) and the guided modes ($k_{\mathrm{sub}} < k_x/k_{\mathrm{EML}} < 1$). The closer the emitting layer gets to a metallic electrode the higher the chance for an energy coupling to electron plasma oscillations on the surface of the metallic layer. These plasmon modes are called surface plasmon polaritons or evanescent modes and in this case $k_x/k_{\mathrm{EML}} > 1$.

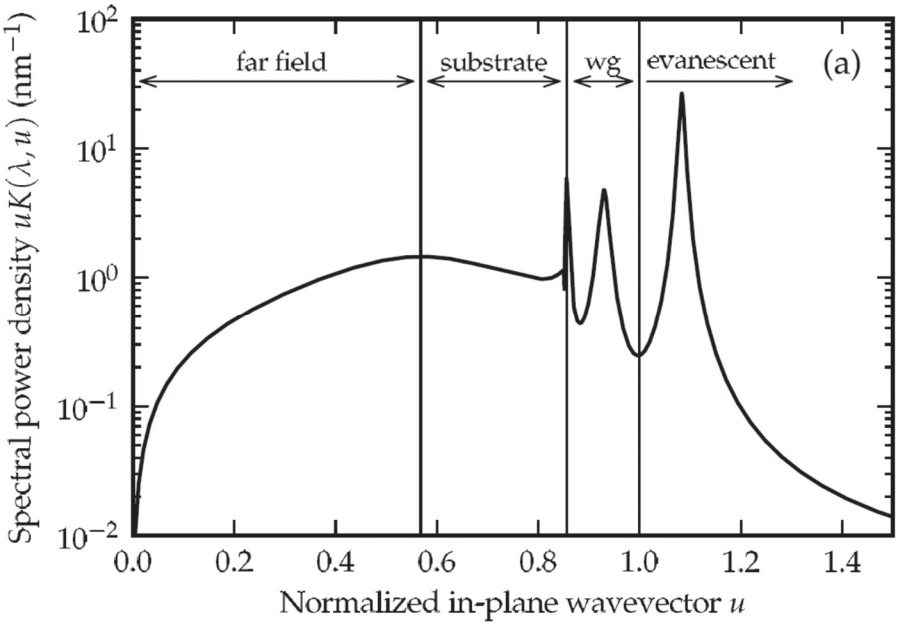

Figure 2-12: Example for power dissipation spectrum for an OLED with a red emitter at a wavelength of 610 nm; $u = k_x/k_{EML}$. Reprinted with permission from [108] Copyright 2012 by the American Physical Society, confirmed by Karl Leo.

In contrast to the substrate, where a continuous spectrum of modes can be found, the spectrum of guided modes is discrete. Another identification for a mode is the effective refractive index:

$$\boldsymbol{n_{\mathrm{eff}} = \frac{k_x}{k_0} = \frac{k_x \lambda_0}{2\pi}} \qquad \text{(Eq. 2-12)}$$

where λ_0 is the wavelength and k_0 modulus of the wavevector in vacuum.

Absorption

Most of the light in guided modes will be absorbed after a while, which is due to the imaginary part of the refractive index of the involved materials. The average length that the photon of a mode is able to travel is called the mean free path L and is invers proportional to the absorption coefficient:

$$\boldsymbol{\alpha = \frac{1}{L} = \frac{4\pi}{\lambda_0} \mathrm{Im}\{n_{\mathrm{eff}}\}} \qquad \text{(Eq. 2-13)}$$

In organic layers, the mean free path of a photon is usually in the micrometer range [109].

Surface plasmon polaritons

At the interface of a dielectric material and a metal, a special case of a guided mode might appear, which is a combination of an electromagnetic wave with a surface charge (plasmon-electron density oscillation). This is called a surface plasmon polariton (SPP) mode and it only exists as a TM mode. The coupling to this mode depends on the frequency and the polarization and is therefore more relevant for small molecule emitters than for polymers [110]. Perfectly horizontally oriented dipoles would only very weakly couple to a SPP mode [106]. A scattering of a SPP mode back to a photon is possible and can be achieved by different kinds of structures [111]. The coupling to SPPs is high for a frequency ω that asymptotically approaches the cutoff frequency ω_s in the dispersion relation curve with:

$$\boldsymbol{\omega_s = \frac{\omega_P}{\sqrt{1+\varepsilon_r}}} \qquad \text{(Eq. 2-14)}$$

where $\omega_P$is the plasma frequency and ε_r the dielectric constant.

Microcavity effects

The emitter material of the OLED is embedded in a dielectric thin-film stack. Additionally, the use of metallic electrodes introduces a mirror into the structure and at the substrate interface reflections are occurring as well. For these reasons micro cavity effects cannot be neglected [112]–[115]. The effect of the cavity can be even worse in top emitting OLEDs as they often employ a second metallic electrode. The result is a strong angular dependence of the OLED spectrum [105]. Some of the drawbacks of the second metallic layer can be in this configuration leveled out by the introduction of a passive capping layer that could be made of an organic or another dielectric material [116], [117]. It can reduce the cavity effect and improve the outcoupling. The microcavity does not only change the spectral emission properties of the OLED, it also has strong effects on spontaneous emission rates [118]. The emission

of a dipole can be maximized by putting it in the maximum of the standing wave produced by the reflection of its own field [119], [120]. The distance between the dipole and a metallic cathode can be changed for example by a variation of the electron transport layer. This also reduces SPP losses and increases the outcoupling [121].

Chapter 3.

Azobenzene functionalization of artificial lotus leaves

This chapter describes and compares two different covalent functionalization processes for the binding of azobenzene molecules to silicone-based materials. The main difference between both azobenzene couplings lies in the crosslinking strategies from silane to azobenzene either by "click chemistry" or by using glutaraldehyde. Both processes proved their suitability to maintain the switching capability of the photochromic molecule after it has been fixed as single layer to a surface. An optimized functionalization method was then applied to the fully stretchable polydimethylsiloxane (PDMS) and combined with a micro- and nanostructuring. The texture was realized with a biomimetic approach: The surface structure of a lotus leaf was molded into PDMS. The resulting surface (schematically shown in Figure 3-1) exhibits a relative absorption difference between trans and cis azobenzene of over 100 % *(around a wavelength of* 355 nm*) compared to just* 0.5 % *on plane glass.*

In the second part of this chapter, an easy measurement setup for creating maps of switched and non-switched surface areas and the characterization of the azobenzene-functionalized lotus PDMS by this device are shown. This setup was additionally used to validate the influence of differently structured areas of the lotus leaf on the optical transmission of the fabricated surfaces.

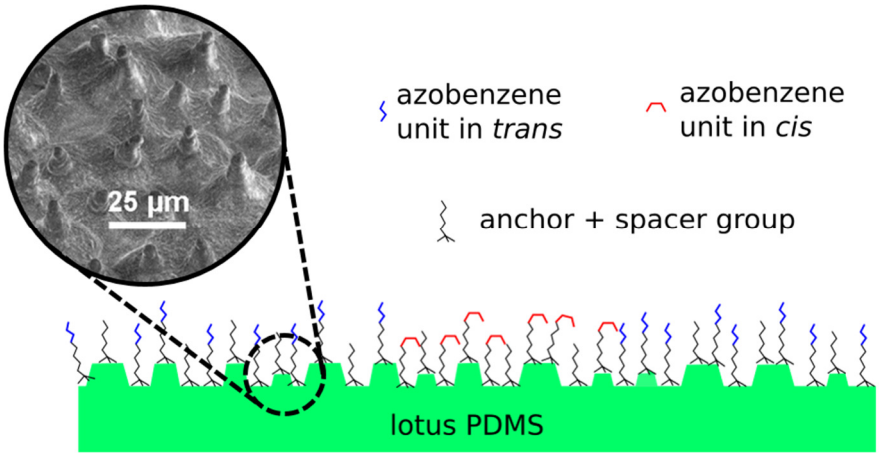

Figure 3-1: Schematic of azobenzene-functionalized lotus PDMS.

Azobenzenes are very basic photoswitches and have therefore been used for a first attempt of creating a surface that is able to change its physical properties upon light excitation. Here, the molecules were covalently functionalized. As the resulting surface needed to be as transparent as possible and the best substrate materials for molecule fixation are either gold or silicon-based materials, a silane-based functionalization process was chosen. Still, there are different possibilities for the fixation of the azobenzene to the silane, while the most prominent one is an amide bonding [122]–[124]. Unfortunately, this bonding is famous for its formation of hydrogen bonds between each molecule and those are reducing the switching properties of the azobenzene [125]. Alternative approaches are the use of a glutaraldehyde coupling and the 1,3-dipolar cycloaddition, also known as "click chemistry". The performance of the two methods are both described and compared on glass substrates in the following part. Flowcharts for checking the process details can be found in Appendix A.

Azobenzene coupling with "click chemistry"

The 1,3-dipolar cycloaddition, commonly known as "click reaction", was developed by Sharpless in 2001 [126] with the aim of a fast, process-orientated reaction with a high output. It was first realized on surfaces by Lummerstorfer and Hoffmann in 2004 [127] and then further developed for azobenzene fixation to surfaces at the Weizmann institute, Tel Aviv (Israel) and the University of Kiel [128], [129]. Also the

switching of cell attachments has been already shown with azobenzenes coupled to a surface with this strategy [130]. Here, this process was further modified in order to be able to functionalize surfaces that are more sensitive.

First, more free hydrogen groups were created on the glass by using a gentle plasma treatment, which subsequently allows a better attachment of the trichlorsilane. For that, a small bottle of 11-bromoundecyltrichlorosilane (ABCR) was first opened under atmosphere for a second and then transferred with the samples and dry toluene into a glovebox filled with nitrogen. Silanes are in general very reactive and clump together very quickly if exposed to atmospheric humidity. A little bit of water instead increases the quality of the silane layer [129]. 11-bromoundecyltrichlorosilane was added to dry toluene, then mixed and the samples were placed into the solution for 30 min, subsequently the sample were taken out and cleaned with dry toluene. The result was a single layer of the silane on the glass surface as shown in Figure 3-2.

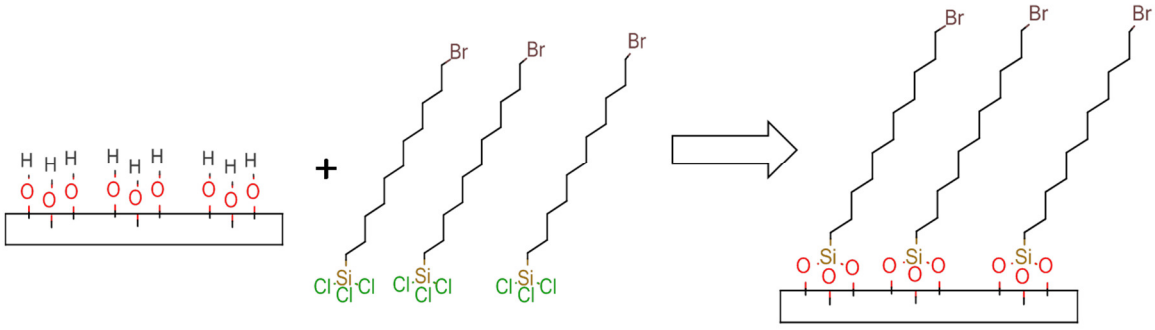

Figure 3-2: Silanization process of glass with 11-bromoundecyltrichlorosilane (30 min. in toluene, under nitrogen atmosphere, 21 °C).

The bromide substituent of silane was now exchanged with an azide group (Figure 3-3). Other publications describe the usage of dimethylfomamide (DMF) for this step [128], [129]. DMF is toxic and additionally resolves many polymers. These two disadvantages were eliminated by choosing another aprotic solvent, the dimethyl sulfoxide (DMSO). Therefore, the samples were placed into a sodium azide saturated DMSO solution for two days at room temperature. Afterwards, the samples were cleaned with the help of an ultrasonic bath in DMSO, water and isopropanol.

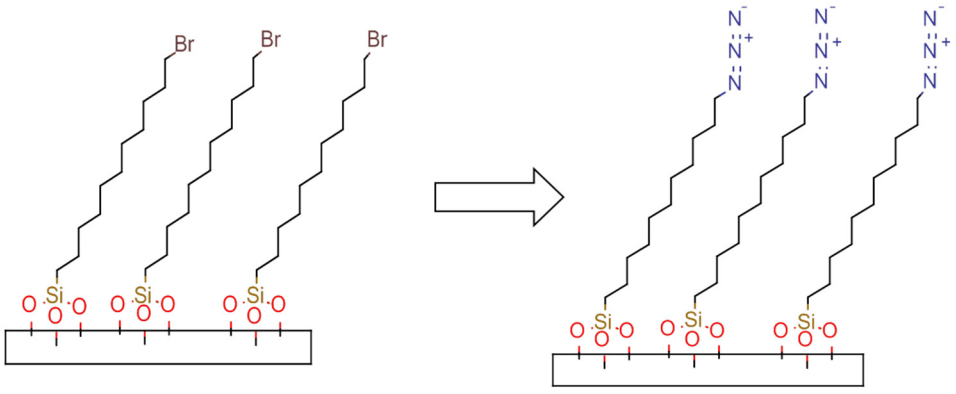

Figure 3-3: Azide exchange (two days, sodium azide in DMSO, 21 °C).

Now the samples were ready for the 1,3-dipolar cycloaddition with the azobenzene. The azobenzene (4-pent-4-ynyloxy-phenyl)-(4-trifluoromethoxy-phenyl)-diazene (OCF_3-AZO) was synthesized by ChiroBlock GmbH, Wolfen (Germany) according to instructions described in LIM [123] and RIVARA [131].

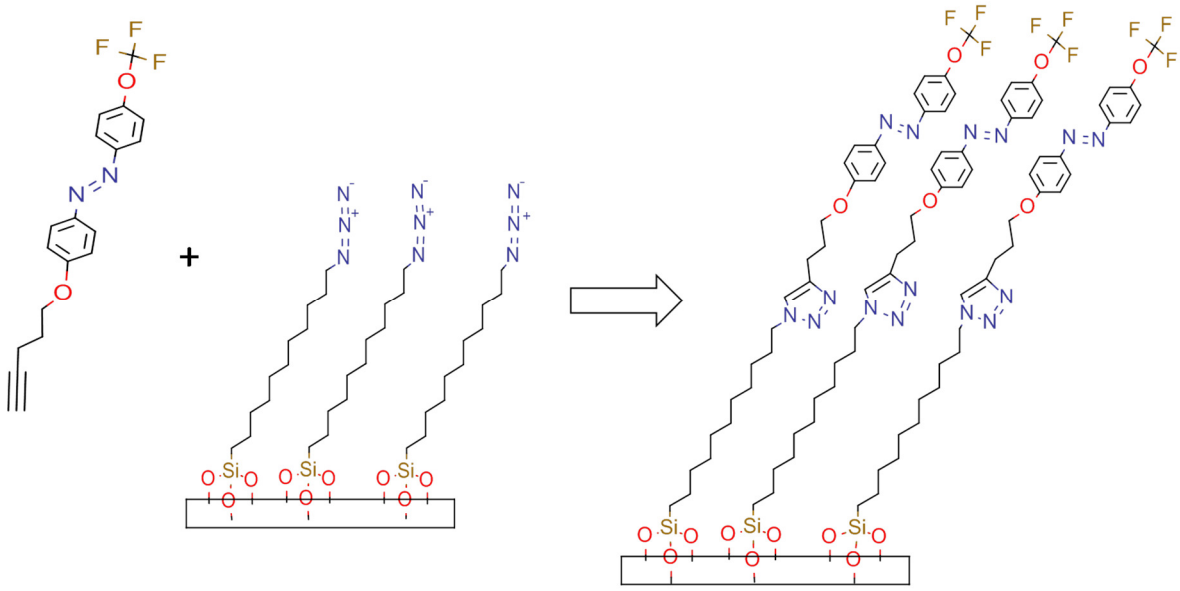

Figure 3-4: „Click reaction" of (4-pent-4-ynyloxy-phenyl)-(4-trifluoromethoxy-phenyl)-diazene to the surface (2 days, aqueous solution of sodium ascorbate and copper sulfate pentahydrate, ethanol, stirring, 21°C).

An ethanolic solution with 2.0 mM concentration of the azobenzene was then given into a small glass vessel together with the samples and an aqueous solution of sodium ascorbate and copper sulfate pentahydrate, which is necessary for the reaction. This

process step was performed at room temperature with stirring for two days and is schematically depicted in Figure 3-4. After a final cleaning procedure with ethanol, acetone, isopropanol and water, the samples were ready for the characterization. For this, absorption measurements with a spectrophotometer (Perkin Elmer Lambda 650) were executed. To switch the azobenzene layer to its *cis* state, an ultra violet LED (Nichia NSCU033B, 365 nm) was turned on for 30 s in front of the samples. The results are depicted in Figure 3-5. If compared to the absorption measurements of an azobenzene in a matrix material (Figure 2-3) one can see that the absorption difference between the two isomeric states of the azobenzene molecule could be higher, which indicated a steric hinderance [132] of the molecules. For this reason, another iteration step was included where an alkyne, 3-phenyl-1-propyne, was introduced in the 1,3-dipolar cycloaddition reaction [124]. As depicted in Figure 3-6 the introduced alkyne coupled to the silane as well and formed a phenyl derivative that guarantees more space for the azobenzene molecule to revoke the steric hinderance. This assumption was stated by the absorption measurement on the resulting samples, which is shown in Figure 3-7. The density of the azobenzene molecule was reduced to the half, but on the other hand the absorption difference between *trans* and *cis* azobenzene around 350 nm was enlarged by this step. Thus, a better switching is achieved.

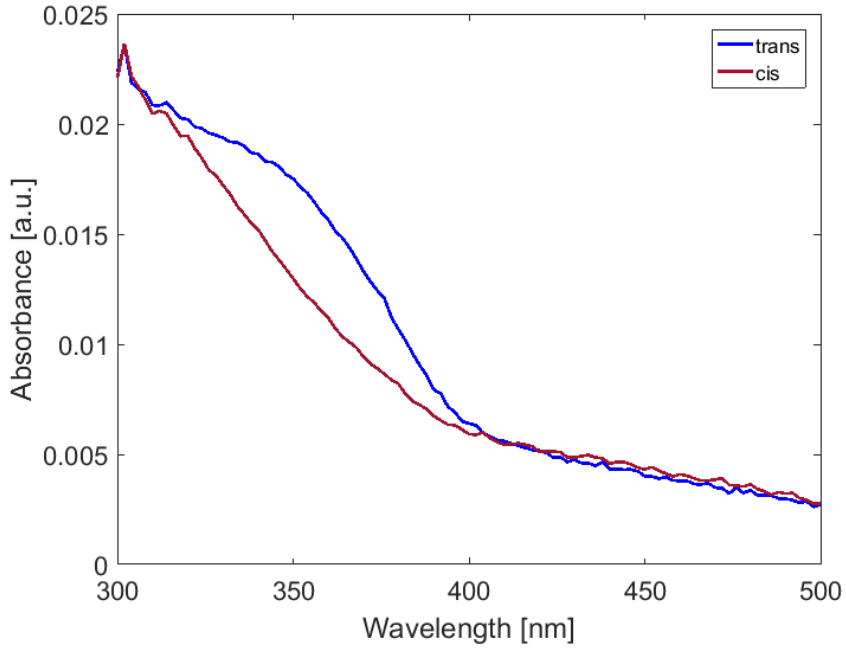

Figure 3-5: Absorption measurement of *trans* and *cis* azobenzene mounted as single layer with trichlorsilane by "click reaction".

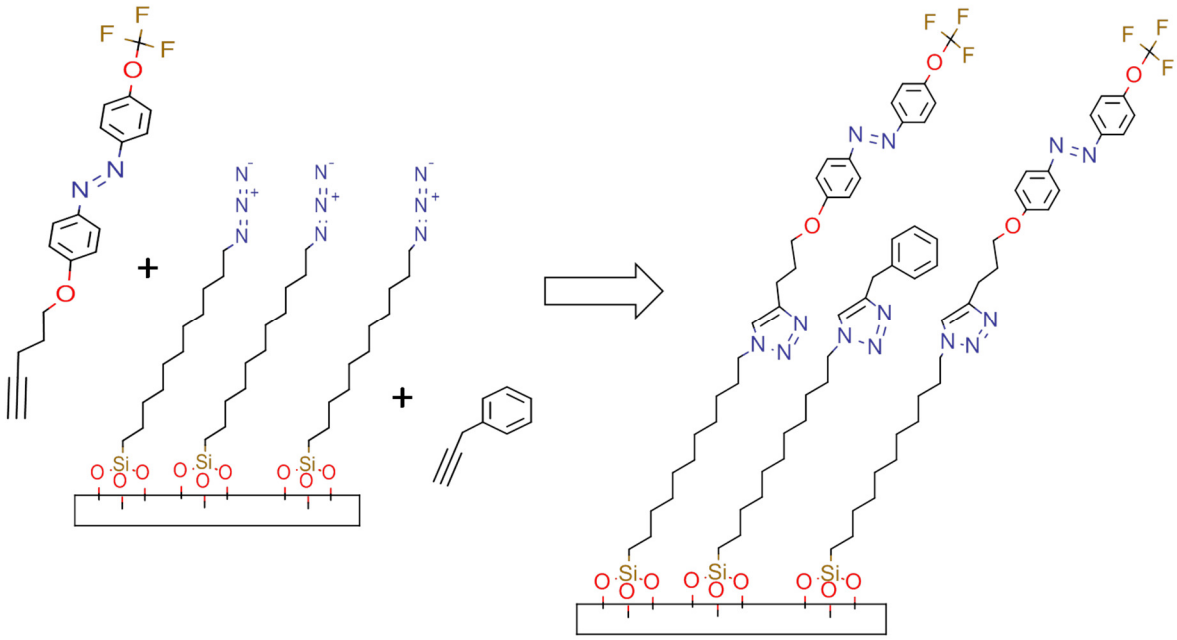

Figure 3-6: Modified "click reaction" of OCF_3-AZO with 3-phenyl-1-propyne to the surface (2 days, aqueous solution of sodium ascorbate and copper sulfate pentahydrate, ethanol, stirring, 21°C).

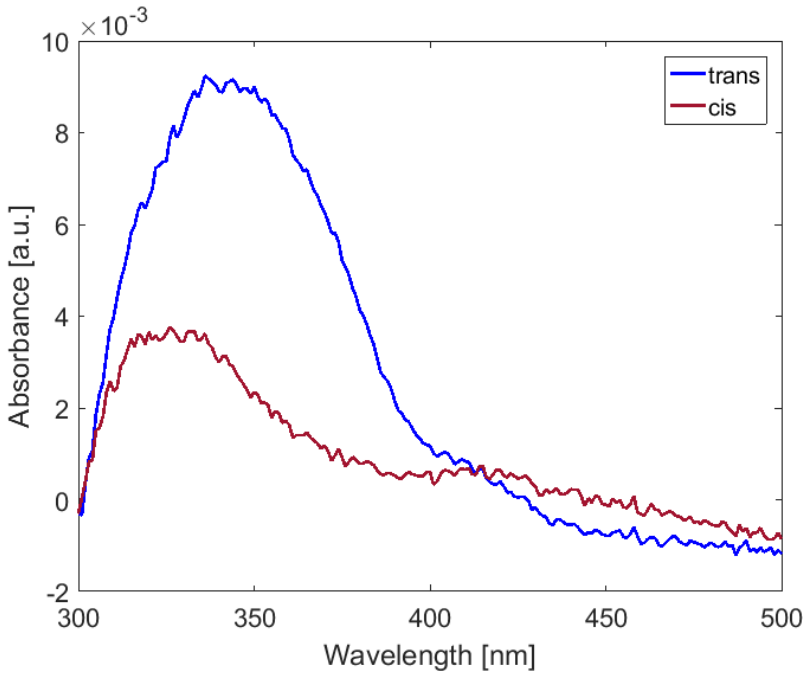

Figure 3-7: Absorption measurement of *trans* and *cis* azobenzene mounted as single layer with trichlorsilane and "click reaction" after alkyne introduction (made by Dr. Christine Kallweit).

Azobenzene coupling with glutaraldehyde

This process was developed by a modification of a functionalization method for aptamer-based protein biochips [133]. Aptamers are oligonucleotides or peptides with a three-dimensional structure that allows to bind specific molecules. Here, these aptamers have been exchanged with an azobenzene molecule. Future application could combine both.

Clean glass substrates were treated with a gentle oxygen plasma to create more free hydrogen groups on top of the glass surface. Afterwards, the samples were put into a mixture of methanol and 3-aminopropyltriethoxysilan (APTES) for one hour under a pure nitrogen atmosphere. This created a single layer of APTES molecules on the glass surface. After washing and drying, the amino group at the top end of the molecule was modified with glutaraldehyde and the help of sodium chloride and sodium hydrogenphosphate. This process step was stopped after one hour by cleaning with a phosphate-buffered saline (PBS) solution, which helped to remove the glutaraldehyde

that did not bind to the silane. Then the samples were dried again and finally, the azobenzene was coupled to the surface. This was performed overnight in a 2.0 mM solution of 2-[4-(4-trifluoromethoxy phenylazo) phenoxy]ethanamine in ethanol. The azobenzene molecule was synthesized by Squarix GmbH, Marl (Germany) according to synthesis instructions taken from Groten et al. [134]. The next day, the samples were rinsed in an ultrasonic bath with ethanol, isopropanol and double distilled water one after the other. The final chemical structure mounted on the glass surface after the described process can be found in Figure 3-8.

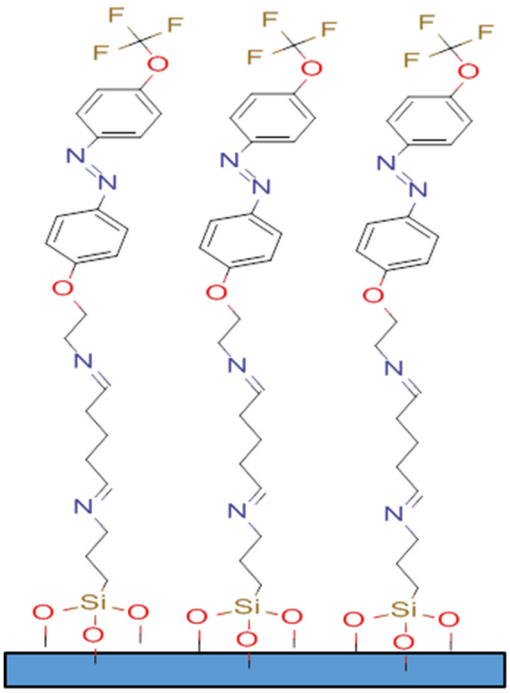

Figure 3-8: Azobenzene bound to surface with the help of APTES and glutaraldehyde.

The absorption spectra of the layer then revealed that azobenzene was bound to the surface (Figure 3-9). The absorption band around 350 nm is decreased after a 30 s exposure to ultra violet light from a high power LED (Nichia NSCU033B, 365 nm). That means that the azobenzene could be successfully switched from its *trans* to its *cis* state.

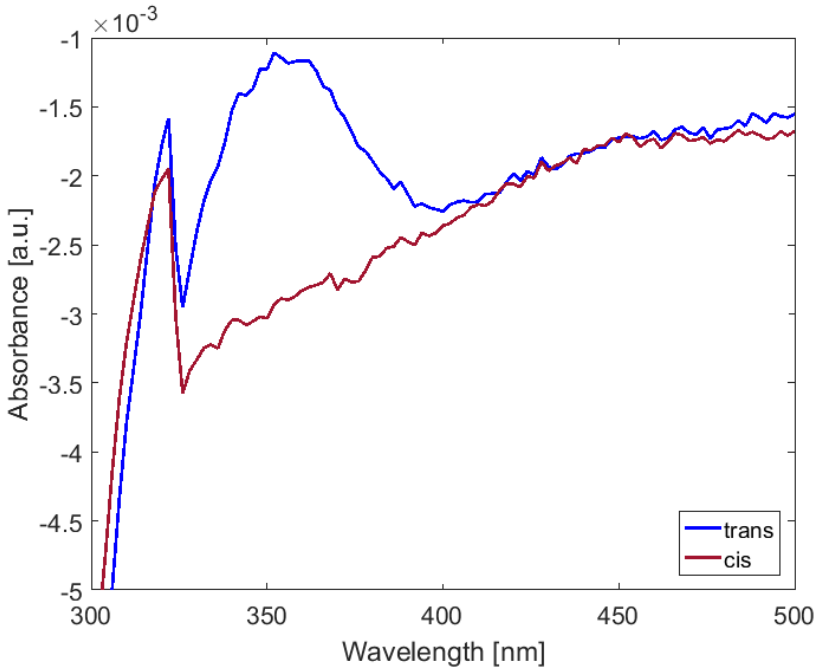

Figure 3-9: Absorption spectra of *trans* and *cis* azobenzene mounted as single layer with APTES and glutaraldehyde on glass.

PDMS molding of lotus leaf

As it was an initial aim to switch the contact angle of water droplets on surfaces functionalized with photochromic molecules, it was watched out for structures that are suitable to enhance the contact angle change resulting from the different polarities of *trans* and *cis* azobenzene. As this is a rather difficult task and it was already partly investigated [129], it was decided to choose a more promising and complex structure. The most famous example from nature is actually the leaf of the lotus, which shows superhydrophobicity with contact angles for water of over 160° [78], [79], [135], [136]. For this reason, the idea came up to functionalize a lotus leaf or at least its structure. Therefore, the surface relief of a leaf has to be transferred into a material that can be functionalized with SAMs. Sun et al. [137] presented a method for producing copies of a lotus leaf into polydimethylsiloxane (PDMS). PDMS has the advantage of being fully biocompatible, flexible and transparent [138]. Additionally, if the surface of PDMS is treated with an oxygen plasma, functional groups can be obtained [139], which allow a subsequent silane bonding to the surface. For these reasons, the process of Sun et al.

was used – just with the little modification of using a very thin gold layer instead of the CVD treatment described in the paper[137]. A detailed flowchart for the fabrication of the positive PDMS copies of a lotus can be found in Appendix A. The main process steps are also depicted in Figure 3-10.

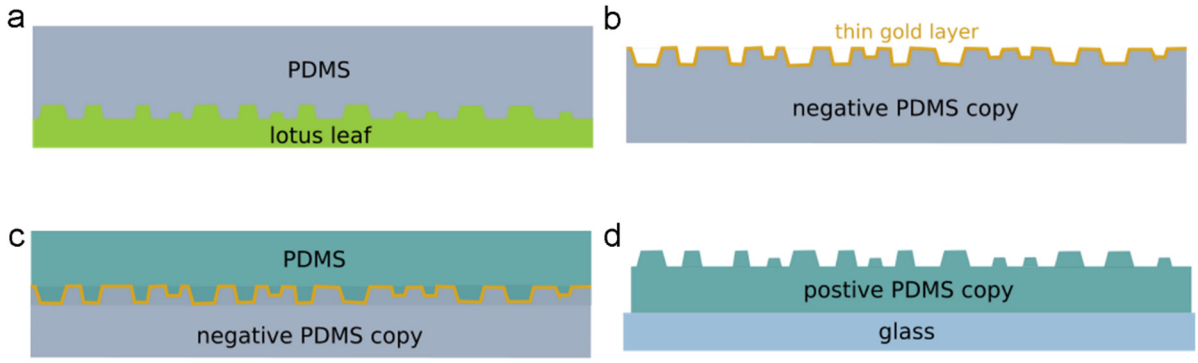

Figure 3-10: Fabrication process for positive PDMS copy of lotus leaf.

First, PDMS was poured on a very fresh leaf of the Indian lotus, Nelumbo nucifera, and cured at room temperature (Figure 3-10a). Two days were needed until the PDMS was fully cured without heating. By heating the water in the leaf it would have been evaporated and disappeared through the fluid PDMS, which would have destroyed the PDMS negative. After the PDMS was removed, 5 nm of gold were evaporated on top of the negative PDMS copy (Figure 3-10b). This layer acted as an anti-sticking layer to be able to separate the second PDMS mold from it later. Then PDMS was poured on the negative PDMS copy (Figure 3-10c) and after an adequate evacuation step in a low vacuum to remove bubbles from the PDMS, the sample was cured at 90 °C within two hours. Now, it was possible to separate the negative from the positive PDMS copy. Due to handling reasons for the later functionalization, the PDMS was additionally bonded on a glass slide (Figure 3-10d). Therefore, the glass slide and the non-separated PDMS sample (back of positive side up) were treated with an oxygen plasma of 100 W RF power for one minute. Immediately afterwards, the PDMS sample and the glass slide were pressed together and then heated to 110 °C on a hotplate for 15 min. Then the sample rested until the next day and the negative PDMS copy was finally removed.

PDMS functionalization

Now, the azobenzene functionalization described at the beginning of this chapter was about to be applied on the lotus PDMS as well. The first used functionalization was the one that employs the trichlorsilane and the "click chemistry". The process parameters were the same as described for the glass slides and are listed with all details in Appendix A.

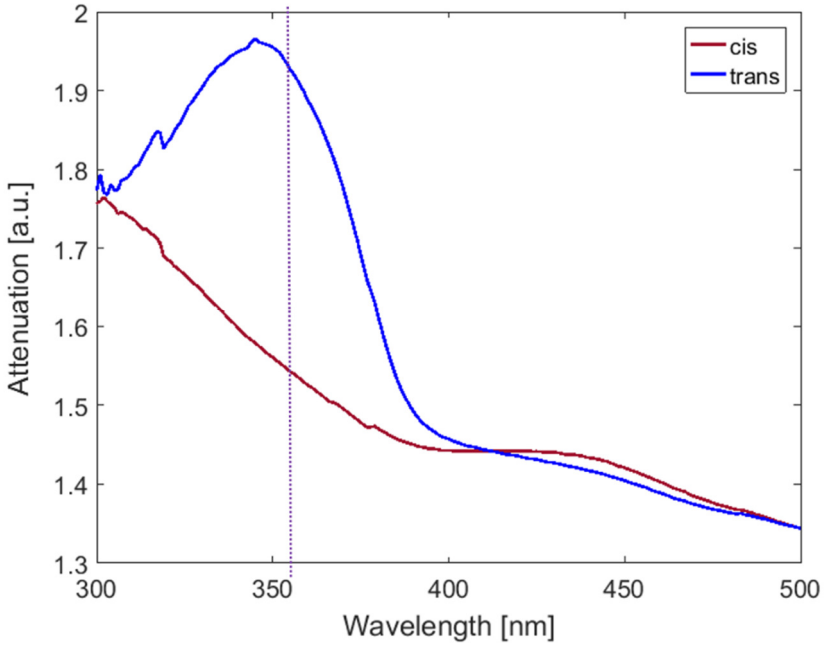

Figure 3-11: Absorption measurement of *trans* and *cis* azobenzene and phenyl derivative mounted as single layer with trichlorsilane and "click reaction" on PDMS (PDMS absorption not subtracted); violet dotted line shows emitting wavelength of laser for characterization.

The absorption measurement of the resulting azobenzene layer on the lotus PDMS is shown in Figure 3-11. Only the absorbance of the glass substrate was subtracted from this measurement because of the thickness variation of the PDMS. Still, the amount of azobenzene molecules is much higher on this PDMS than on glass (Figure 4-7) while the switching works pretty well.

The coupling method with glutaraldehyde was applied onto the lotus PDMS as well. Again, the process was executed as described for the functionalization on the

glass substrates. The resulting absorption measurement of the fabricated SAM can be found in Figure 3-12. The amount of azobenzene molecules is a bit lower than on the samples that were prepared with the "click chemistry" approach. This effect was also already visible on glass when comparing Figure 3-9 with Figure 3-7. The switching capabilities were a bit less distinctive, which is surprising because they have been better on glass (Figure 3-9).

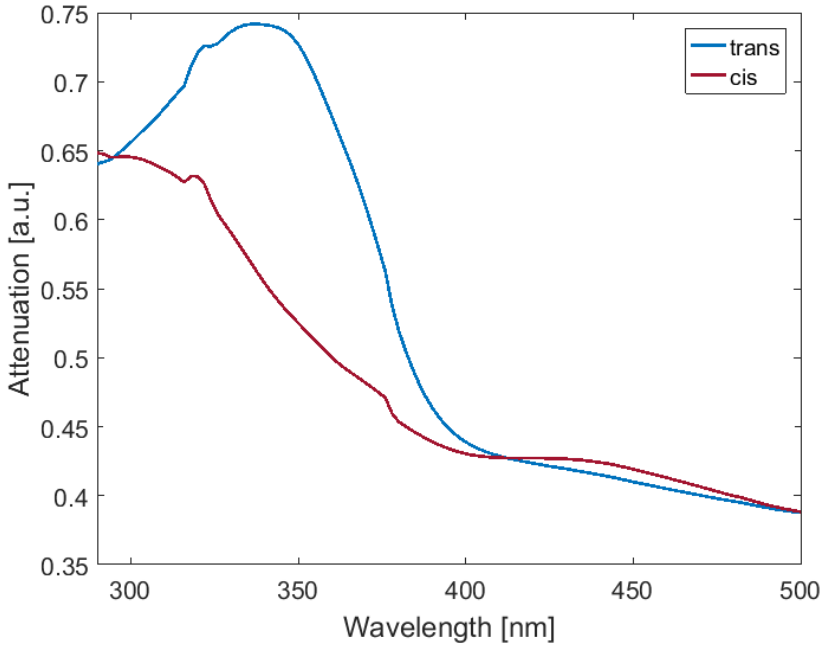

Figure 3-12: Absorption spectra of *trans* and *cis* azobenzene mounted as single layer with APTES and glutaraldehyde on the lotus PDMS; PDMS absorption not subtracted.

Structure and wettability characterization

The nonfunctionalized lotus PDMS had quite comparable properties in terms of the wettability issues as the natural one: Over 150° were measured for the contact angle of water droplets on these surfaces (with an OCA50AF from dataphysics). This value is close to the contact angles on a natural lotus leave [135], [136]. After the treatment with oxygen plasma the surface wettability was checked again. As expected, the contact angle was reduced, which is due to the formation of free silanol groups (Si-OH) on the surface [140]. The precise value was 110° - measured about two hours after plasma

treatment. To check if the surface structure fully survived the plasma treatment, SEM images were prepared. For this purpose an additional silver layer of 20 nm was evaporated onto the lotus PDMS. The SEM images of the surface are given in Figure 3-13, which shows a lotus PDMS surface before (a) and after (b) the treatment with oxygen plasma. As visible when comparing both pictures, the nano roughness on the micro pillars is clearly reduced. As a consequence of this it is also expected that the contact angle on top of the surface will be reduced.

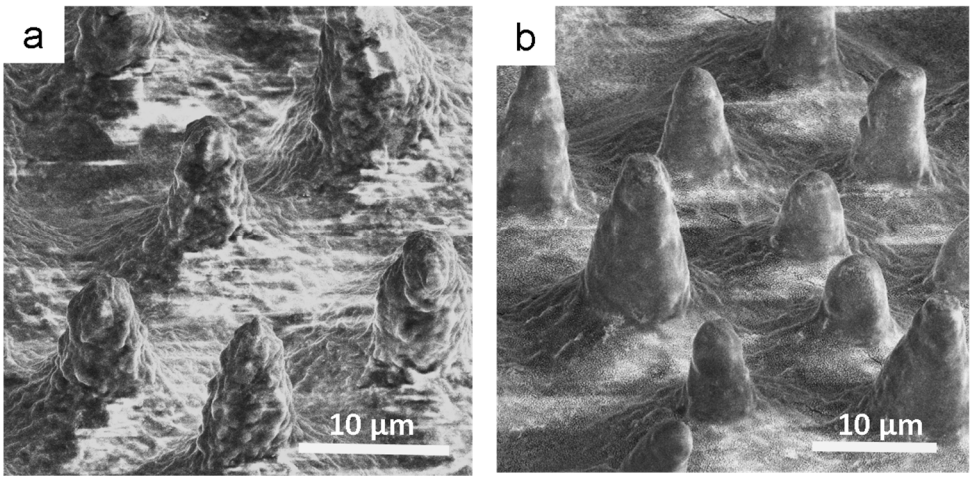

Figure 3-13: SEM image of lotus PDMS (a) before and (b) after treatment with oxygen plasma.

The lotus PDMS was then functionalized with azobenzene molecules as described before. The contact angle of water droplets stayed around 110° with both functionalization procedures. Additionally, the surfaces were exposed to UV light to switch the azobenzene molecules to their *cis* state and to check if the contact angle would change with this, but that did not happen.

Time and location dependent characterization of switching performances

When developing photoswitchable surfaces there are a few more questions coming up for the characterization once the deposition proved to work and the photochromic molecules are attached to the surface. One question is the temporal behavior of the

photowitchable layer. As already described in Chapter 2, the switching speed of a photochromic molecule is highly reduced on a surface compared to the switching speed in a solvent [44]. This allows rather simple measurements, for example by integrating LEDs for the switching into a spectrophotometer and then simply measure at one specific wavelength [53]. In case there is no spectrophotometer available, it is also possible to measure the absorption of a laser beam with a photodiode. For this case, the laser wavelength is selected such that it lies directly at the maximum absorption difference between the different states of the photochromic molecule. The laser spot on the surface is smaller than the usual spot of the beam in spectrophotometer, which leads to a reduced detection limit. But in case of the functionalized lotus PDMS the amount of azobenzene molecules is high enough, and no beam expanding is needed.

Instead, the small laser beam has another advantage: a higher planar resolution. This raised the idea to build a scanning setup for the photoswitchable surfaces that allows detecting of switched and non-switched areas on the surface. This capability is also very practical for the development of sensors etc. comprising photochromic molecules. A schematic of the setup for scanning the azobenzene-functionalized surface is shown in Figure 3-14.

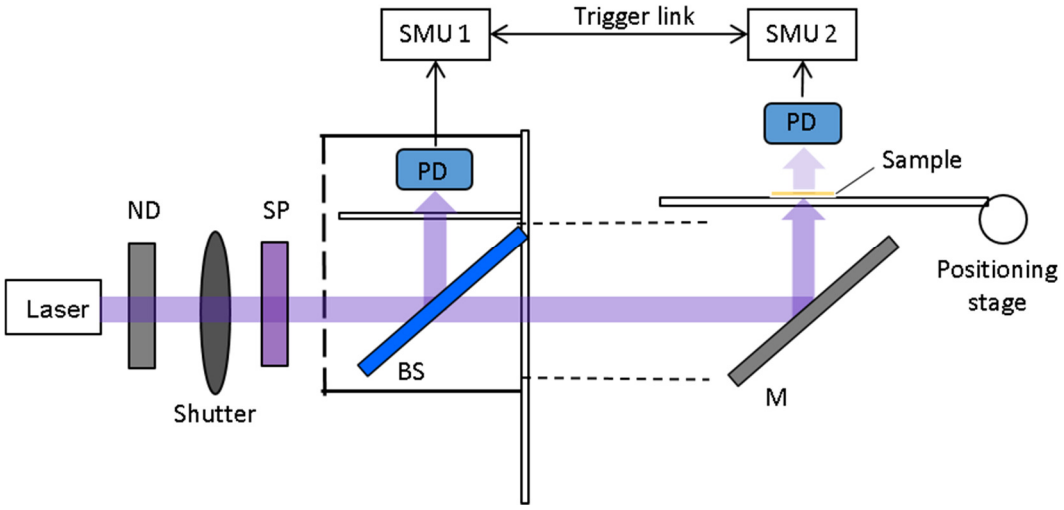

Figure 3-14: Schematic of setup for laser scanning of samples.

The laser used for the scanning setup was a Cobolt Zouk CW that emits at a wavelength of 355 nm, which is well positioned in the difference maximum of *trans* and *cis* azobenzene (compare to Figure 3-11). To drive the laser as stable as possible it was working with 5 mW (maximum 10 mW) external power, but this is still a high value and would have already caused a strong switching effect on the layer. Therefore, a neutral density filter (ND) was used, which filtered 80 % of the light. In addition, a shutter controlled the exposure to the sample and a shortpass filter (SP) with a cut-off at 400 nm blocked laser emission at higher wavelength that might appear due to a non-complete up-conversion process in the laser. The beam was then divided by a beam splitter (BS) and directed to two photodiodes (PD). The signals of the photodiodes were measured with two source measurement units (Keithley SourceMeter 2400) that were connected via a trigger link to guarantee a completely synchronized measurement. One beam passes through a mirror and an objective before going through the sample and then exciting the photodiode. The power of the laser beam was measured with 10 μW at the position of the sample, while the beam spot covered an area of 0.64 mm². The sample was placed on a positing stage (Prior ProScan II) of a microscope during the measurement. The whole setup was controlled with the help of National Instruments LabView. To ease the measuring sequences a bit, the program calculated a relative Transmission *T* from the data given by the photodiodes in the form of:

$$\boldsymbol{T = \frac{I_1 R}{I_2}} \qquad \text{(Eq. 3-1)}$$

where I_1 is the current measured of the photodiode behind the sample, I_2 the current of the reference photodiode and *R* a reference factor. Before starting a measurement, *R* is determined so that *T*=1. The triggering of the SMUs is controlled such that for each measurement point, a series of seven current values is obtained. All of them are transferred to the LabView program, which then calculated the average value in order to reduce noise. Additionally, the program supported further binning for noise

reduction, but this comes also with an unwanted longer exposure of the sample to the laser beam. The performance of the setup was checked with the help of thin layers of the fullerene C60 evaporated on float glass. These samples were scanned with the setup and the results can be found in Figure 3-15. The measurements always started in the upper left corner and ended in the lower right corner. They showed that very low absorption differences can be determined with this setup. In Figure 3-16 shows that even 0.8 nm of C60 on glass were made visible.

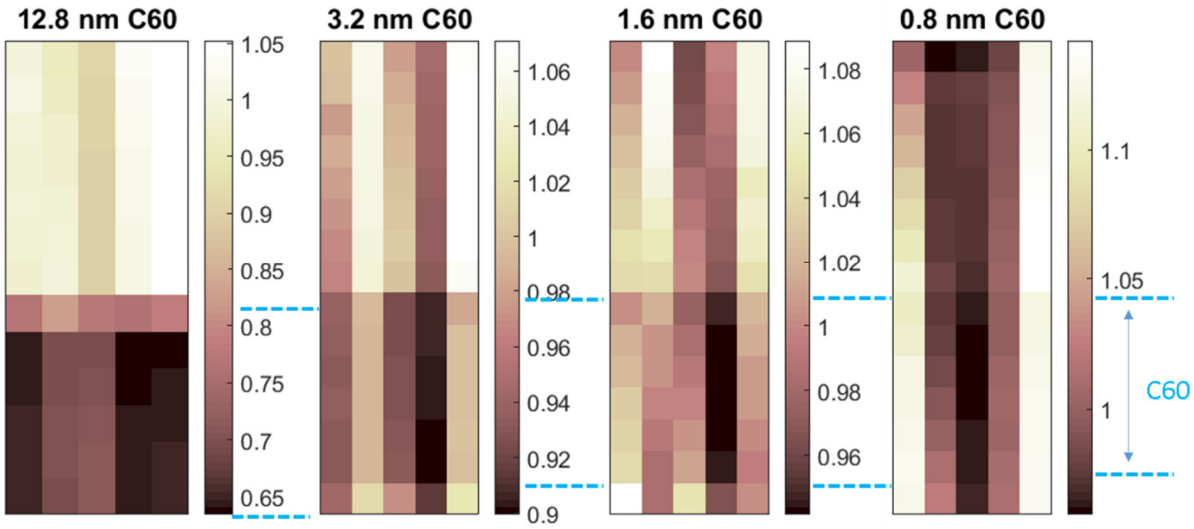

Figure 3-15: Scans of C60 stripes (bottom of each scan) with different thicknesses.

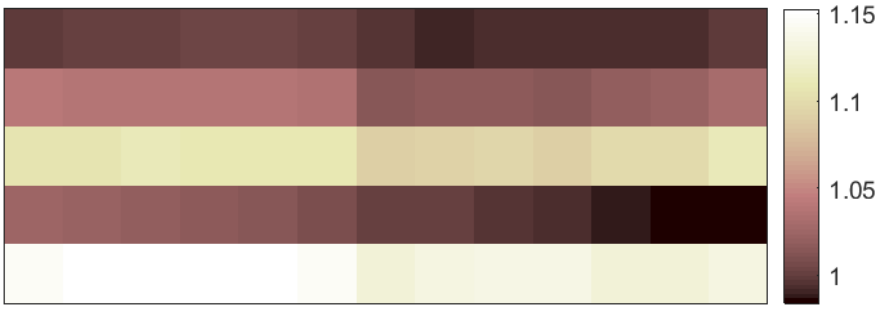

Figure 3-16: Scan of rotated C60 stripe (on the right) with a thickness of 0.8 nm.

As Figure 3-16 shows a rotated sample, it illustrates also the main limiting factor for this measurement: absorption differences of the substrate. The stripes with the strong color difference (white to yellow to dark red) are mapping the thickness differences of the glass substrate. Although these substrates were of a high quality and were also used for OLED fabrication, grooves were formed by the fabrication process.

On a highly polished quartz wafer, it was possible to detect C60 layers of 0.4 nm. The comparison of C60 layers with the absorption of azobenzene shown in Figure 3-17 states that the detection limit of the setup is quite close to the absorption differences of *trans* and *cis* azobenzene. Unfortunately, is was not possible to differentiate between switched and non-switched azobenzene areas mounted on simple glass or quartz.

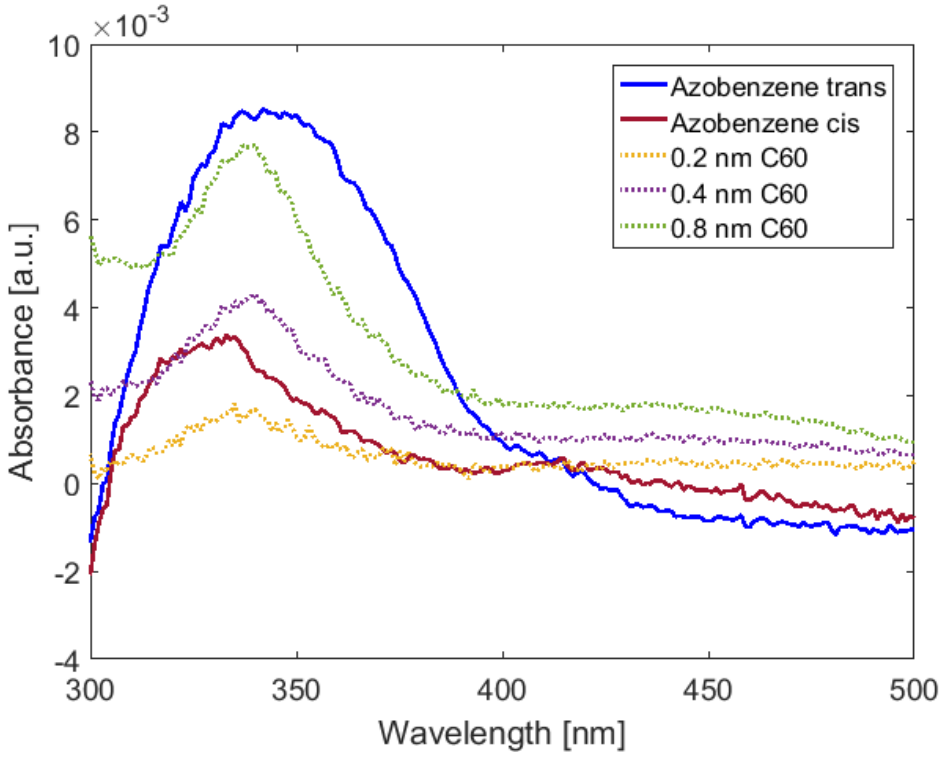

Figure 3-17: Comparison of absorption of azobenzene states and C60 layers on glass (Azobenzene measurement by Dr. Christine Kallweit).

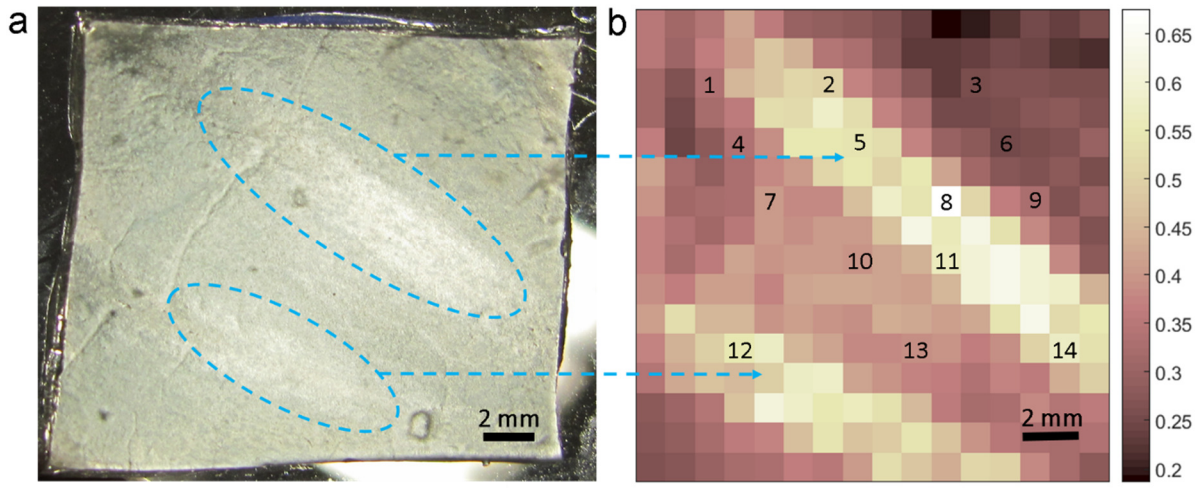

Figure 3-18: (a) Photo of functionalized lotus PDMS and (b) transmission scan of the surface; numbers indicating the measurement points for time resolved switching, results can be found in Figure 3-21.

Figure 3-18a shows a photograph of the functionalized lotus PDMS with the areas of the leaf veins showing a higher transmission, although the PDMS actually is thicker there. Lower scattering causes this effect. In the right part of the same figure (b) a scan with the UV laser setup is depicted. Also in this graph the position of the leaf veins can be clearly observed and the transmission in the vein area proved to be 70 % ± 30 % higher. For that measurement, all azobenzene molecules on the surface were in the *trans* state. Now, a cross was cut in the center of a piece of paperboard and this simple mask was put on the sample. Afterwards an exposure to UV light was carried out for 15 s. The exposure time was reduced in this case because it turned out to give better results. This might be due to guided UV light in the PDMS or glass substrate that excites the molecules crabwise. Then the surface was scanned again and delivered the map shown in Figure 3-19a. This map was normalized to a point apart from the leaf veins and the excited area. The same was performed with the scan before the UV exposure (Figure 3-18). Afterwards, the difference of both maps was computed in MATLAB and the result is given in Figure 3-19b. As can be seen the cross symbol is clearly visible in this plot and it states that it is possible to detect switched molecule areas of a SAM on a surface.

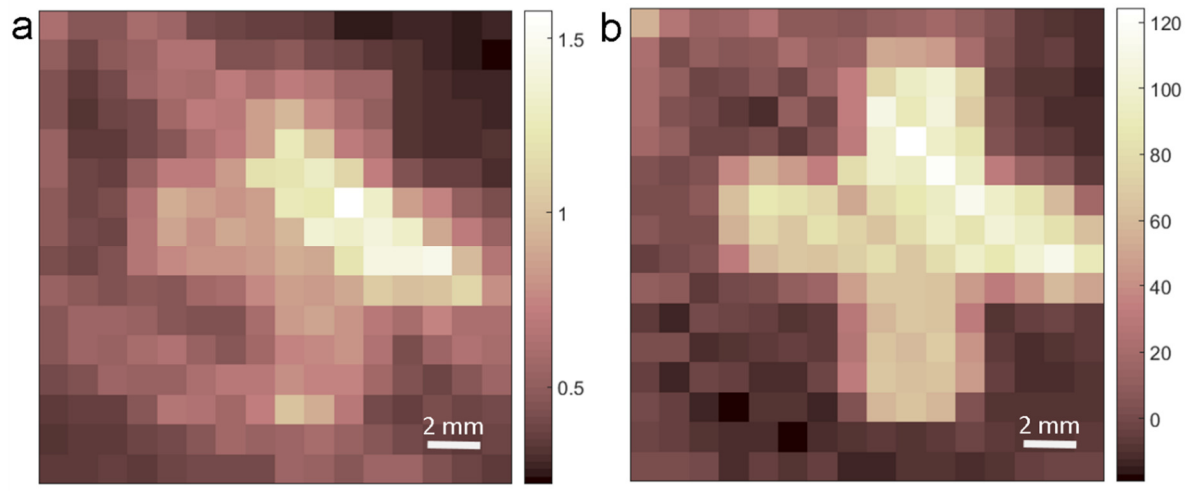

Figure 3-19: (a) Transmission scan of functionalized lotus PDMS after partial exposure to UV light and (b) difference plot of the scan before and after UV partial UV exposure (legend in percent).

If the sample position is not changed by the stage, also time-resolved measurements of the switching process are possible. Examples are depicted in Figure 3-20. There measurements on functionalized quartz glass substrate and the lotus PDMS are shown. In the beginning of the measurement, the molecules are kept in the *trans* state with blue LED. Once the LED is turned off the azobenzene layer starts to change into the *cis* state due to the laser light. When the blue layer is switched completely, the LED is turned on for 3 s between each measurement step and thereby a fast back switching is obtained.

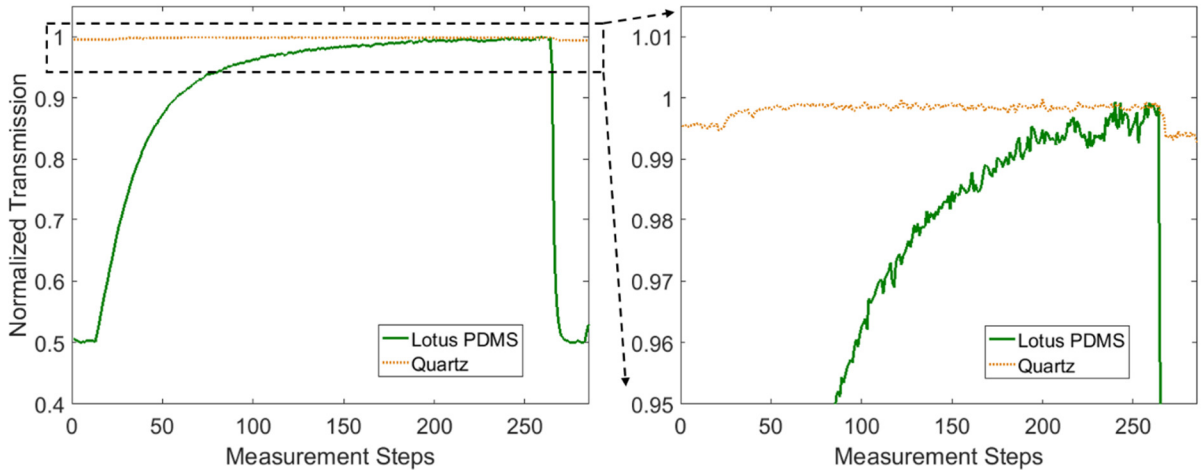

Figure 3-20: Switching of azobenzene layer on lotus PDMS and quartz glass from *trans* to *cis* and back to *trans*, magnified on the right.

The Figure 3-20 clearly demonstrates the performance differences between both substrates. On quartz, the transmission difference is with 0.5 % low and the azobenzene layer is switched quite fast by the UV laser. On the lotus PDMS instead the transmission can be doubled by switching from *trans* to *cis* and around 200 measurement points can be performed until the layer is fully switched. Even areas with different transmission were observable on the lotus PDMS (Figure 3-18) and it was already seen in Figure 3-19b that the switching difference between *trans* and *cis* state was higher in the vein area. For these reasons, time resolved measurements in the area of the leaf veins were compared with the areas apart from it. The measured curves are depicted in Figure 3-21. In this case the reference factor R was only obtained for the first measured point apart from the vein area. One can see that the initial transparency is higher in the vein area (dashed lines) compared to other areas (solid lines), but also the percentile increase of the transmission from *trans* to *cis* is with 119 % ± 4.5 % higher in the vein area than apart from the veins with 97 % ± 9.8 %. This effect can be attributed to a convolution with lower absorption and lower scattering in the vein area. Comparing the time constants of each switching curve, no significant difference between the areas can be found.

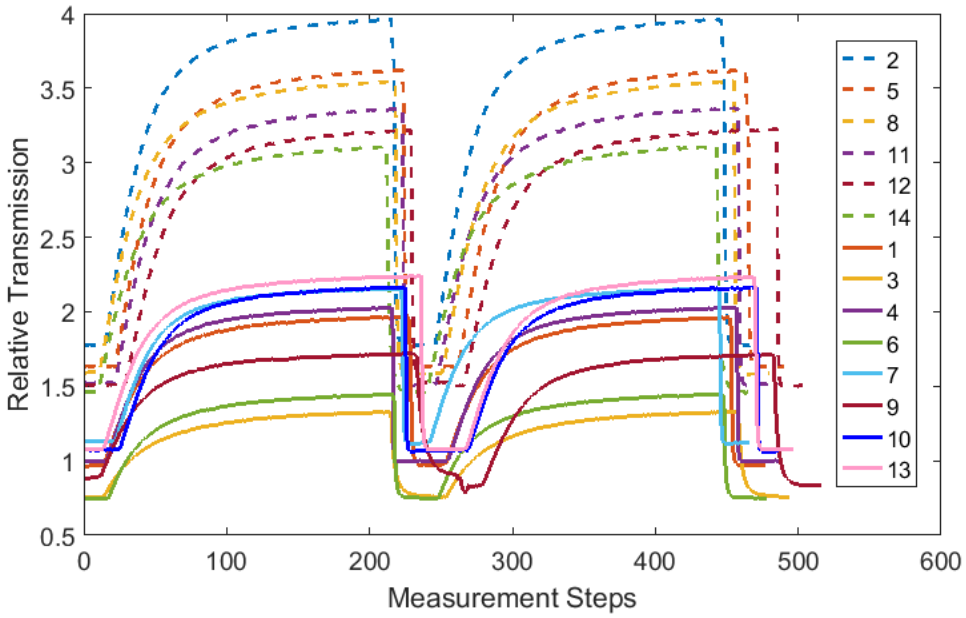

Figure 3-21: Switching of azobenzene layer on different positions of the lotus PDMS; Positions can be found in Figure 3-18. Dashed lines stand for measurements on leaf veins and solid lines for areas apart from the veins.

Discussion

Two different concepts for the covalent functionalization of surfaces with photochromic azobenzene molecules were shown in this chapter. One process involved "click chemistry" and the other one a coupling with glutaraldehyde. Both processes were optimized and proved to be applicable for fabrication of a switchable layer. They were combined with the biomimetic approach of copying a lotus leaf structure into the PDMS. Although shown in literature on similar systems [1], [141]–[146] this combination was not able to generate wettability switching. This problem is attributed to the surface binding strategies as they might force the molecule to switch in an unattractive way and such that there is no change of the surface tension obtainable.

In the second part of this chapter, a setup for a fast time and location-resolved characterization of photochromic layers was shown. The resolution limit for the lateral measurement was found to be set by the substrate inhomogeneity in terms of

absorption. Another problem is the guiding of UV light in the substrate that is successively switching other areas as well. This decreases the resolution of the setup. Time-resolved measurements of the switching could even be made on flat glass substrates. This laser based measurement revealed the advantages of combining the azobenzene functionalization with the lotus PDMS: It was the high relative absorption difference with an enhancement factor of 200 compared to the absorption change on a flat quartz glass substrate. The higher molecule density and the convolution of the surface structure and absorption made the creation of surface maps a lot easier.

The described findings show that it is possible to create a photoswitchable surface also on a fully flexible and biocompatible material. With the laser scanning setup, a comparably cheap characterization method has been demonstrated, which is useful for the realization of future devices—in particular for mapping the switching of photochromic molecule layers excited by an OLED matrix. This topic will be further investigated in Chapter 5.

Chapter 4.

Non-covalent spiropyran coatings

A simple functionalization process is described that allows the reversible photo-inducted wettability switching on carbon soot coated surfaces. The process involves a drop casting method supported by 0.001 mol/L *spiropyran in toluene with added 25 % acetone. Compared to the functionalization without acetone, where the maximum contact angle difference achieved values over 80°, acetone reduced this value to about 40°, but it added the reversibility of the contact angle switching. Due to the high absorption of the surface, it has been also tested to use the same spiropyran functionalization on other structured surfaces that showed far less absorption, but these experiments were not showing a switching of the contact angle.*

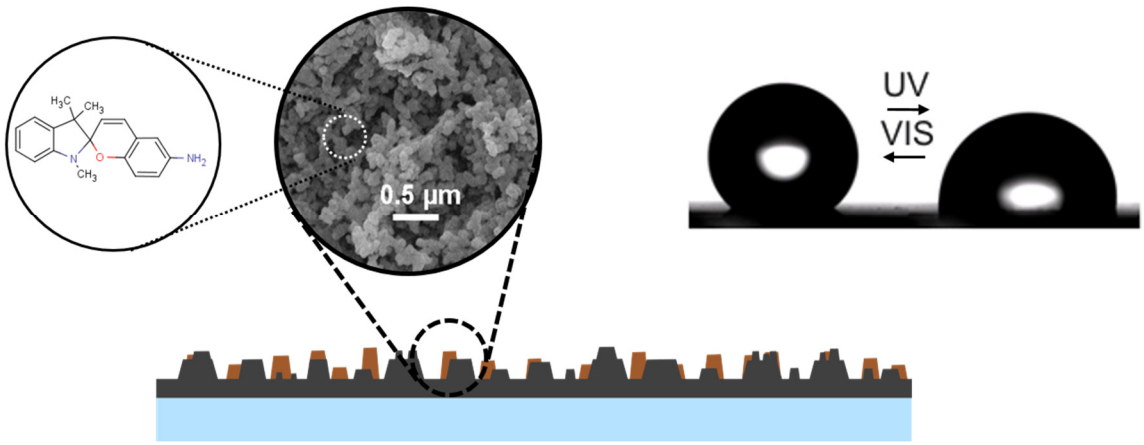

Figure 4-1: Schematic of spiropyran-coated candle soot surface with inset showing the reversible contact angle switching of a droplet.

The idea behind the experiment with spiropyran came from experiments that were performed with pupils by the Leibniz Institute for Science and Mathematics Education in Kiel, aiming to increase the interest for science in the participating groups [147]. In these experiments glass slides were coated with a carbon soot by simple candles. Afterwards, this coating was covered with spiropyran molecules from a toluene solution and this involved a very simple dropcasting method by evaporating the toluene, leaving only the spiropyrane on the surface. This process was initially developed within the bachelor thesis of Daniela Ingwersen [148] and produced a surface which could be switched from hydrophobic to hydrophilic, but not back to hydrophobic again. In the described experiments of Daniela Ingwersen contact angle differences up to 80° were achieved. The simplicity of this process seemed to be very attractive and so, it was decided to try applying it on different surfaces in order to make them transparent.

Surface structuring

As already described in Chapter 2 surface structuring is crucial for achieving high contact angles. Covering the surface with a photo-switchable molecule then and thereby allowing a change of the surface tension upon light exposure, realizes photo-switchable contact angle changing. The higher the initial contact angle, the larger the potential contact angles become. Here, the used structuring techniques for the experiments with spiropyran are described.

Simple candle soot

Simple microscope slides were cut into 25 mm x 25 mm pieces and then cleaned with acetone and isopropanol in an ultrasonic bath. After drying, the samples were held into the middle flame zone of a normal candle (Fenomen, IKEA) for 50 s to 90 s until the surface was fully opaque as can be seen in Figure 4-2a. Higher or lower flame zones are producing less stable surfaces [148]. Putting these surfaces under an SEM reveals that the carbon soot consists of 20 nm to 40 nm big carbon particles, clustering

to more complex structures as depicted in Figure 4-3b. These surfaces are highly hydrophobic and are showing water contact angles above 160° [21].

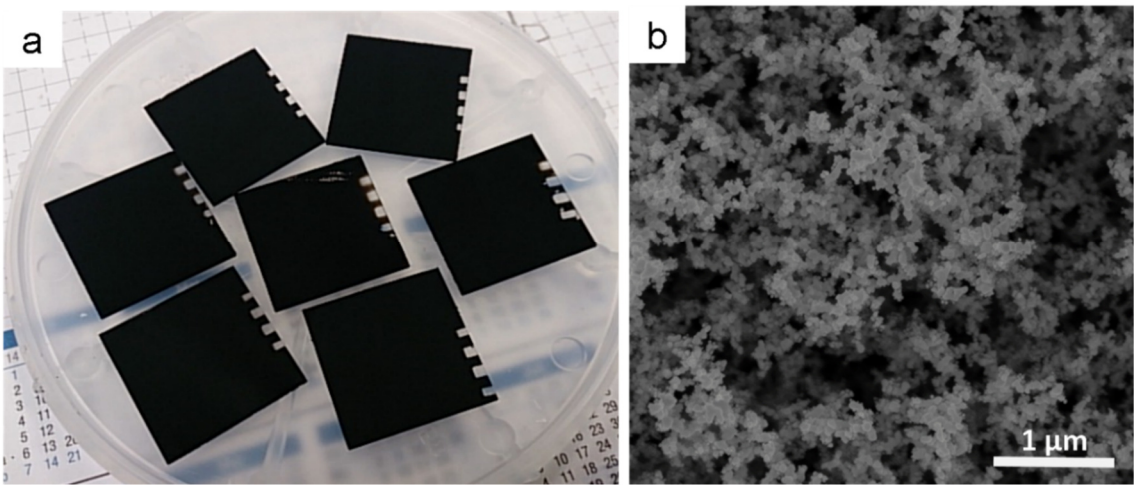

Figure 4-2: (a) Glass slide covered with candle soot; (b) candle soot under SEM (SEM image made by Torben Karrock).

Transparent candle soot

The transparent candle soot structures are an advance of the simple candle soot and were inspired by DENG [21] Therefore, the sooted glass slides were placed into a mid-sized desiccator together with 2 mL tetraethyl orthosilicate (TEOS) and 2 mL of an aqueous ammonia solution (28 %), each in small glass vessels. After the lid was closed, the samples were left in the desiccator for 24 hours. During this time a silicate film was deposited on the samples. The process behind this is also known as Stöber reaction.

Subsequently, the samples were taken out of the desiccator and put into a muffle furnace (Nabertherm) at 600 °C. This caused that the carbon degraded and diffused through the porous silicate film. After two hours there was no more carbon and all that was left was the nano-porous silicate structure (Figure 4-3a). This structure is highly hydrophilic and transparent, but has got a high haze. Under the SEM, the structure looks still quite similar to normal candle soot as can be seen in Figure 4-3b.

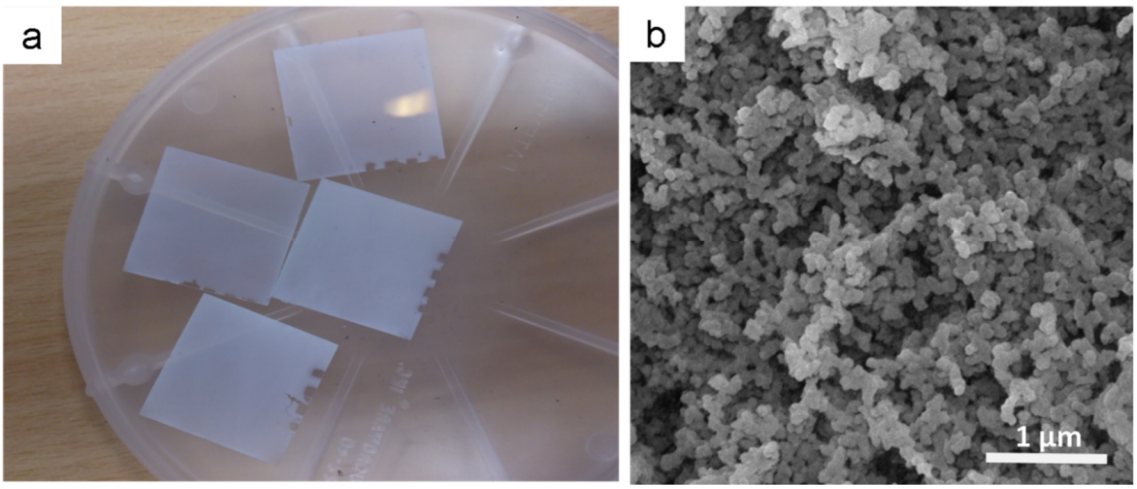

Figure 4-3: (a) Glass slides covered with transparent candle soot; (b) transparent candle soot under SEM (SEM image made by Torben Karrock).

Artificial sharkskin foil

The artificial sharkskin foil used for spiropyran experiments was obtained from Joanneum Research Materials from Austria. A shark possesses small triangle structures on top of its scales in order to reduce the water resistance. This is imitated on an artificial sharkskin foil by a 1D microstructure with triangles as schematically depicted in Figure 4-4a. The foil was fabricated by a roll-to-roll process, where the structure was pressed into a photoresist and afterwards cured by light. Additionally, the surface was fluorinated to increase the surface tension and to make it hydrophobic. Due to the 1D structure, the contact angle of water droplets is only enlarged in one dimension and this leads to drawn-out droplets as is shown in Figure 4-4b. A strong advantage of this structure is the low scattering.

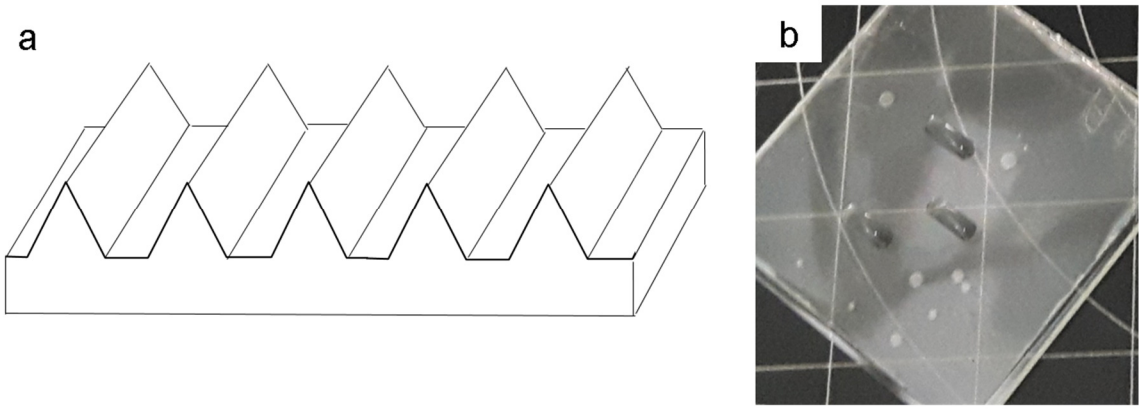

Figure 4-4: (a) Schematic of 1D micro structure of sharkskin foil; (b) long droplets formed on sharkskin foil (glued on glass).

Spiropyran coating

After the surfaces of the samples were structured, they had to be covered with spiropyran. Therefore, the synthesis of the spiropyran molecule will be described here and additionally, the drop casting method that was used for the deposition of the spiropyran on the samples.

Molecule synthesis

The spiropyran used for the coating process was freshly synthesized with the support of Dr. Britta Hesseler. The full name of the molecule is 1′,3′-dihydro-1′,3′,3′-trimethyl-6-nitrospiro-[2H-1-benzopyran-2,2′-[2H]indol] and will from now on be called spiropyran. Its chemical structure is shown in Figure 2-4. It is a simple spiropyran and can also be commercially obtained. As a conclusion, this molecule can be synthesized according to known instructions [149]–[151].

For the synthesis 3.47 g (20.0 mmol) 2-methylene-1,3,3-trimethylindoline and 3.34 g (20.0 mmol) 2-hydroxy-5-methylbenzaldehyde (both from Sigma Aldrich) were refluxed with 70 mL ethanol (Carl Roth) for five hours. After the solution was cooled down to room temperature, the deposit was filtered and washed with cold ethanol. The product was then dissolved in ethanol, heated, cooled to room temperature and

again filtered and washed. A yield of the final product of 2.83 g (42 %) was achieved and it had a light green to brown color. It was controlled by ^{1}H-NMR, which was performed by the Institute for Organic Chemistry at Kiel University: (200 MHz, $CDCl_3$, TMS): δ = 8.05 – 7.98 (m, 2H), 7.20 (td, ^{3}J = 7.5 Hz, ^{4}J = 1.4 Hz, 1H), 7.13 – 7.04 (m, 1H), 6.92 (m_c, 1H), 6.88 (td, ^{3}J = 7.5 Hz, ^{4}J = 1.0 Hz, 1H), 6.77 (m_c, 1H), 6.56 (d, ^{3}J = 7.5 Hz, 1H), 5.86 (d, ^{2}J = 10.4 Hz, 1H), 2.74 (s, 3H), 1.30 (s, 3H), 1.19 (s, 3H) ppm.

Drop casting

Now the spiropyran coating process for the structures will be described. The base for the coating was a simple drop casting process, with optimized parameters regarding solvent, spiropyran concentration and evaporation duration that were found out by Daniela Ingwersen [148]. A glass petri dish with a diameter of 100 mm was placed onto a hotplate inside a fume hood and heated up to 40 °C. Then the samples were placed inside the dish and it was very carefully filled with 25 mL of toluene with a 0.001 mol/L concentration of spiropyrane. Not being careful with the filling can already destroy the carbon soot structure! Now, the dish was closed with a lid employing Parafilm as a spacer between the bottom and lid dish. This is important, because the air circulation of the fume hood disturbs the process, but the solvent still has to be evaporated. Best results were achieved, when the solvent was completely evaporated after about 80 min. The process is also schematically depicted in Figure 4-5. After all the solvent was evaporated, the spiropyran covered the samples and the ground of the petri dish.

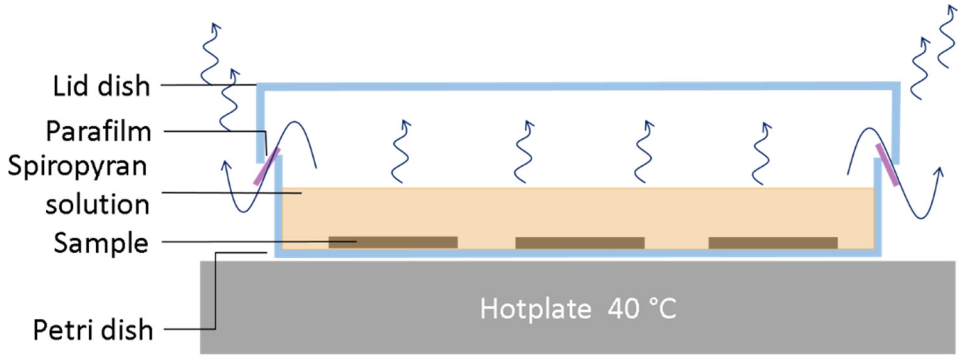

Figure 4-5: Schematic of solvent evaporation during the drop casting process.

In a next step, the same process was used with the difference that 5 mL acetone were added to the spiropyran-toluene mixture in the glass petri dish. The acetone was added carefully with the help of a pipette, while all other parameters stayed the same.

Both process circles were performed with all the three structures described above. Only the shark skin foil was glued on a glass substrate, because it would float on the solvent without additional weight.

Surface characterization

In the following paragraph, the characterization of the fabricated samples is described. A main emphasis lies on the photo-initiated contact angle switching. Whenever light is used for photoexcitation of a sample, this was conducted with LEDs. The ultraviolet (UV) light was produced by a Nichia NSCU033B LED with a center wavelength of 365 nm and the blue light by a Luxeon LXML PR01 0500 LED with 448 nm. The UV LED provided a radiant flux of 96 mW/cm² and the blue LED 25 mW/cm². These values are the reason for the different exposure times of 100 s for UV and 300 s for blue light.

First, we have a look on the sample by our naked eye. A photograph of the coated simple candle soot samples is given in Figure 4-6.

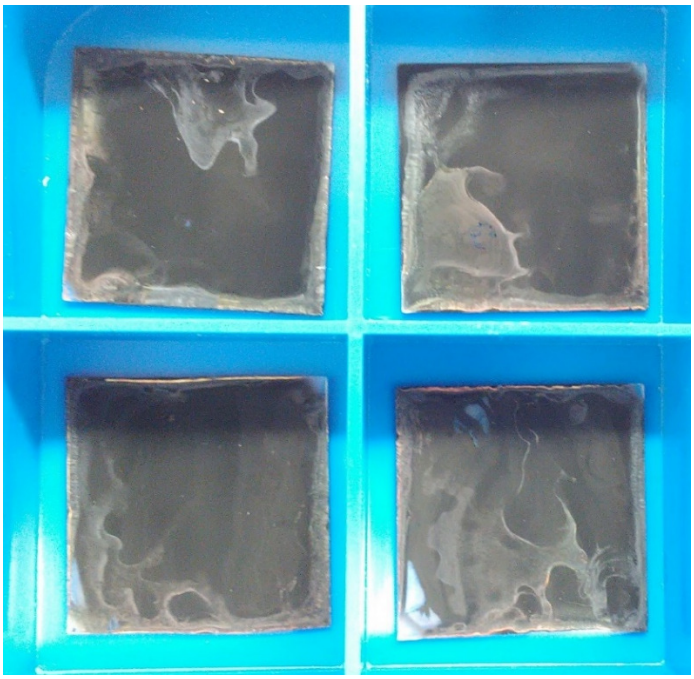

Figure 4-6: Candle soot samples after spiropyran coating (Photos by Ruprecht Reinke).

If comparing these samples to their appearance before the coating (Figure 4-2a), it can be seen that most of the sample surfaces have changed from a deep black to a more grayish color with some white deposits that can be found mostly at the edges and a bit randomly spread in the center. Neither the addition of acetone during the preparation process nor its photoexcitation does have an effect on the visual appearance of the coated surfaces.

Figure 4-7a+b are showing photographs of the spiropyran coated transparent candle soot samples. A yellowish deposit can be found on these samples, which forms a continuous band at the edges and a more random structure in the center. By exciting these surfaces with UV light, the yellowish deposit changes its color to violet as also depicted in the same figures. Having utilized acetone in the preparation process, the color can be switched back to a light yellow with the help of blue light. Without the adding of acetone during the coating, the color of the surface stays violet / orange upon excitation with blue light and even after leaving the samples at room temperature in the lab for weeks (Figure 4-7b).

The deposit on the sharkskin foil has got the same color as on the transparent candle soot (Figure 4-7c). The clear difference can be seen in the distribution of the deposit, because there are just a few agglomerations on the samples. Instead, the coating works much better on the back of the foil. As demonstrated in Figure 4-7d, the surface is very uniformly covered with the spiropyran allowing a clear photo patterning. For the shown picture, a thin polycarbonate plate labeled by a waterproof pen was used for shadowing the UV light from the LED.

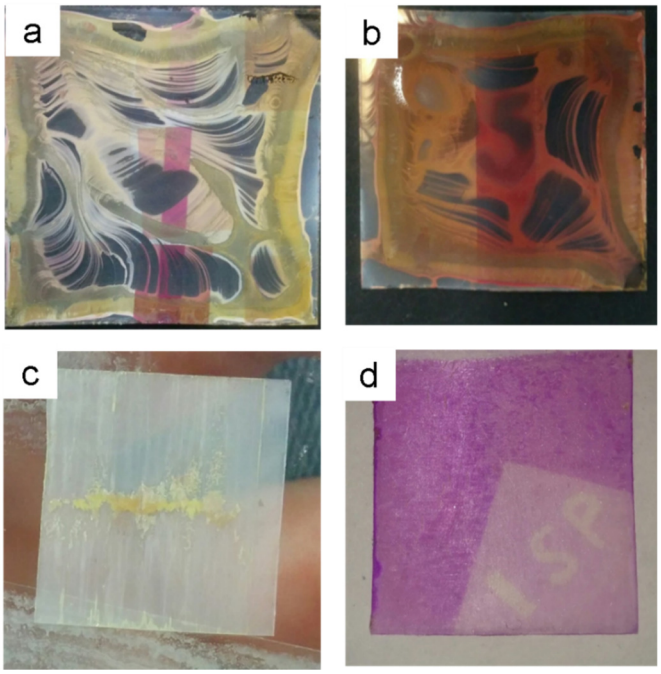

Figure 4-7: (a) Transparent candle soot sample after spiropyran coating partially excited with UV light; (b) transparent candle soot sample with spiropyran prepared without acetone one week after UV excitation; (c) sharkskin foil after spiropyran coating; (d) back of sharkskin foil after spiropyran coating and partial UV excitation (Photos by Ruprecht Reinke).

Contact angle switching experiments

The contact angles of water droplets on the prepared samples were measured with a dataphysics OCA 50AF in the sessile drop mode. In a first round, the most promising experiment of Daniela Ingwersen [148] was more or less simply copied. Putting water droplets onto these surfaces before and after 100 s of UV excitation gave comparable

results for the contact angle switching. The water droplet was removed before the light excitation. Switching from a higher to lower contact angle is in principle also possible with the droplet remaining on the surface, but it is adding more variance to the results as the droplet itself acts as a lens and evaporation of the water might also influence the final results. After each droplet deposition, it had 60 s to rest to its final position. The best measurement is depicted in Figure 4-8. Unfortunately, the variance of the achieved results was enormously high so it did not even make sense to determine it. The initial contact angle and especially the contact angle difference are not only depending on the details of coating method, but also highly on the position on the sample. The best results were mostly achieved close to the edges. After the measurement of the reduced contact angle that resulted from the UV excitation, the droplet was removed again and the sample was excited with blue light for 300 s, but the contact angle never changed again.

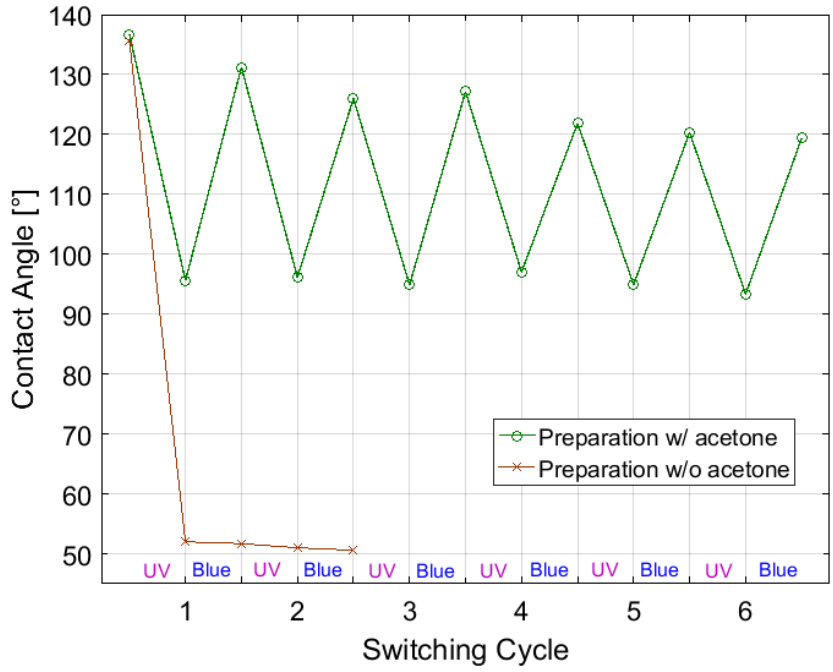

Figure 4-8: Results of contact angle switching experiments on spiropyran coated candle soot surface; the droplet position did not change, but it was removed prior to light exposure of the sample.

The samples that were fabricated according to the modified process with the added acetone instead showed different contact angles after the blue light excitation. An example of a contact angle measurement on these surfaces is also shown in Figure 4-8. The drawback here was that the contact angle difference was reduced compared to the surfaces that were prepared without acetone, but the switching was reversible for many times—just with a small degradation of the more hydrophobic contact angle.

The transparent candle soot surfaces were more hydrophobic in the yellowish areas and still hydrophilic in other areas. With the coating process without acetone a maximum contact angle difference of 43.4° (initial contact angle 126.5°) was achieved. Again, the variance of the results was very high. A back switching could not be seen on these surfaces. In contrast to the simple candle soot surfaces, on the transparent ones it was not possible to realize a reversible switching by adding acetone during the coating.

The coated sharkskin foil performed even lower. Neither on the front nor on the back side of the foil there was a contact angle switching after either fabrication of the processes observable.

SEM characterization

The samples with the simple candle soot structure were now put inside a scanning electron microscope to check what happens to the candle soot structure after the deposition of spiropyran. The samples with other structures were neglected for this experiment, because they did not show any contact angle switching. The images were made with an SEM by Zeiss, Modell Supra 55VP. For preparation, a 30 nm layer of silver was thermally evaporated on all samples. To be able to make suitable comparisons, three different samples were selected: one with pure candle soot, one spiropyran coated without and one with acetone. The image of the pure candle soot can be found in Figure 4-2b. The ones of the other samples can be seen in Figure 4-9.

To sum up the results of the SEM characterization, it can be said that the spiropyran is deposited in form of flakes on top of the candle soot structure. The form of these

flakes varies a lot over the whole sample surface and actually, each form can be found on either of the samples. Most of the flakes can be found close to the sample corners, but this was already predictable when having a look on the samples by your naked eye (compare to Figure 4-6). Unfortunately, it is clear, that the different flake formations will affect the resulting water contact angle of the surface, because they are a part of the surface structure. Due to the high amount of different forms and the problem that they do not cover a larger area uniformly, it is extremely difficult to measure the influence of the flake form on the resulting contact angle.

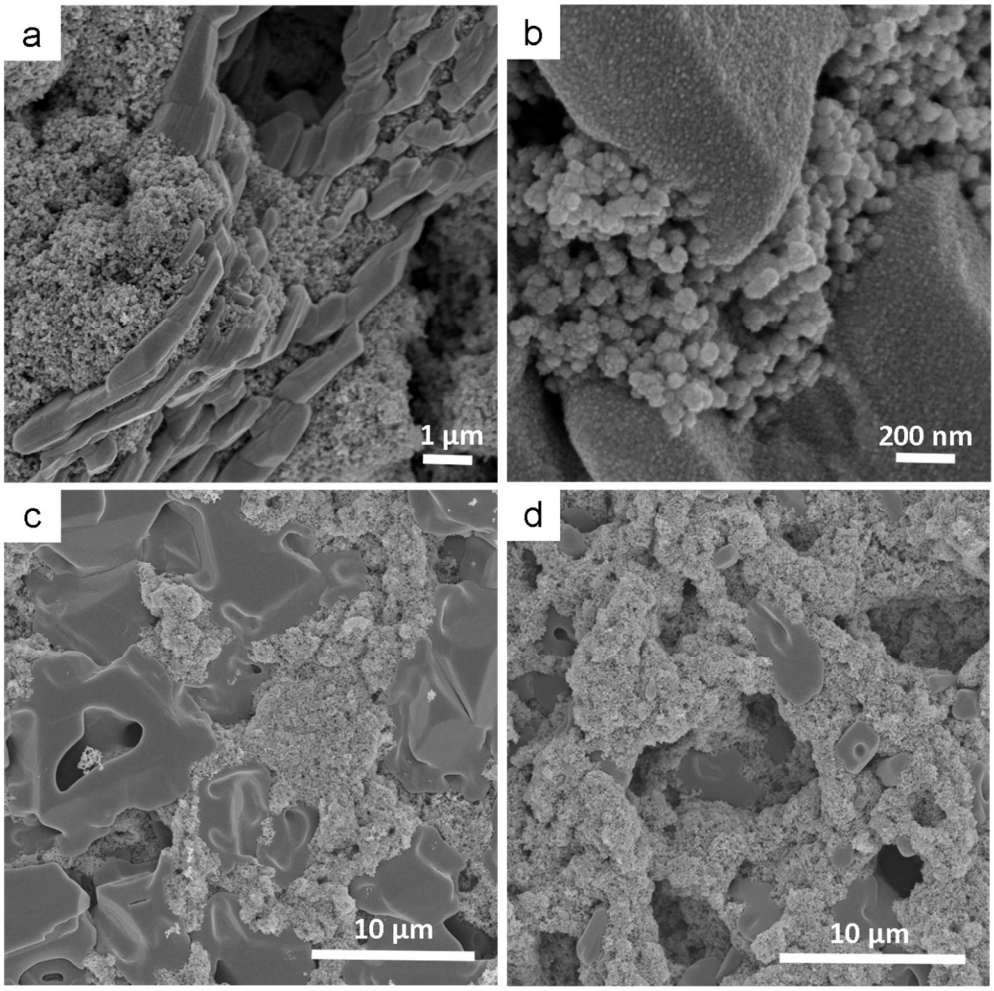

Figure 4-9: SEM images of spiropyran coated candle soot surfaces; (a) + (b) without acetone; (c) + (d) with acetone (Images made with help of Mohammadreza Taale).

Interesting was the occurrence of cracks inside the structure of samples (Figure 4-10), where the acetone was added during the coating process. These cracks might be the reason for decreased stability of these samples.

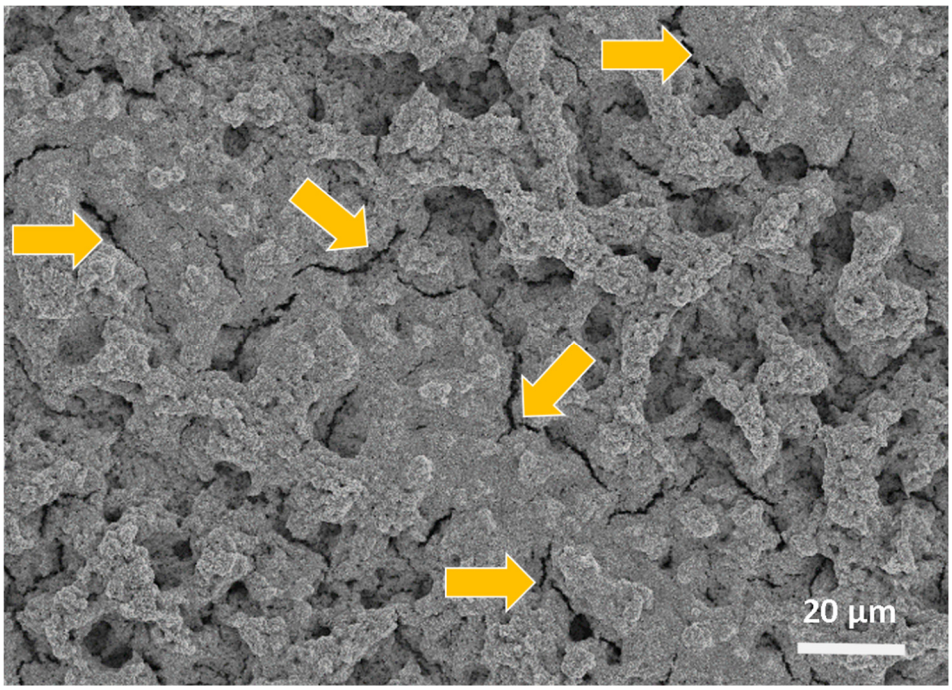

Figure 4-10: SEM image of spiropyran coated candle soot surface with arrows marking cracks (Image made with help of Mohammadreza Taale).

Discussion

Concluding this chapter, the development of a very simple fabrication process of surfaces that show photo-induced and reversible contact angle switching was achieved. The samples with simple candle soot structures show contact angle switching, when the spiropyran is deposited just with the help of toluene, and even reversible contact angle switching could be achieved with preparation of a 5:1 mixture of toluene and acetone. This was a surprising result since here was just a non-covalent surface functionalization used and these effects have never been shown so far. Drawbacks of the described method are the very poor uniformity of the resulting surfaces, which is due to the hardly controllable processes of the soot deposition and the evaporation of the solvents, and the enhanced sensitivity of the surface after adding acetone during the preparation. This is most probably caused by the cracks

seen under the SEM (Figure 4-10). Additionally, there is no color switching observable due to the high absorption of the carbon. The samples with transparent candle soot are showing a clear color change instead and it can even be made reversible with the toluene and acetone mixture. A contact angle switching can be seen on these surfaces after their first UV illumination as well, but strangely there is no reversible contact angle switching after the fabrication with the help of the solvent mixture.

The upper side of the sharkskin foil showed a very poor homogeneity with the spiropyran coating, but with its back it was possible to create nice uniform color changing surfaces (Figure 4-7d). A contact angle switching could not be achieved on these surfaces. A problem might be the fluorine coating of the foil that might affect the deposition of the spiropyran. Definitely it would be more practical to have a foil with 2D structuring instead.

Still unclear is the effect of the flake formation, its impact on the contact angle and its switching behavior, but as the areas with the same flake formation are smaller than needed droplets would be, it is not possible to perform contact angle measurements on them. In addition, the influence of solution mixture is poorly understood. A reason could be lying in the different polarities of the two solvents. The possible crystallization and maybe the already described merocyanine aggregation [5] might be affecting the final performance of the surfaces. In summary, there are many unclear points in the understanding of the described functionalization method, and still a plenty of research has to be conducted to fully understand and optimize the described process that might be performed better by a chemist. Applications might be found where one would like to minimize the interaction with the electrical properties of the substrate, e. g., when functionalizing graphene [152] or nanotubes [153]. For the usage in microfluidics, it is better to use covalently coupled molecule layers as they cannot be washed away [5]. The switching of the spiropyran-coated candle soot surface by OLEDs will be shown in the next chapter, but due to their non-existing transparency, it will not be possible to fabricate the OLED on the back of the same substrate. This makes the surface less practical for an integrated device.

Chapter 5.

Switching surface properties with OLEDs

This part describes the merging of the photo-switchable surfaces described in Chapter 3 and Chapter 4 with OLEDs, in order to realize a complete and compact "programmable" system that changes surface properties according to a signal input (Figure 5-1). First, two different stacks for blue OLEDs based on the emitters BCzVBi and DCzTrz were fabricated and characterized. The BCzVBi-OLEDs achieved a radiant flux with up to more than 10 mW/cm². *It was shown that this OLED had enough power to switch different azobenzene layers, which was verified by the measurement of the layer's absorption at the same time. The photochromic surfaces were always brought in state B with the help of an UV LED first and then switched back with an OLED. At the end of this chapter a complete system with a blue OLED switching the wettability of a spiropyran coated candle soot surface is presented.*

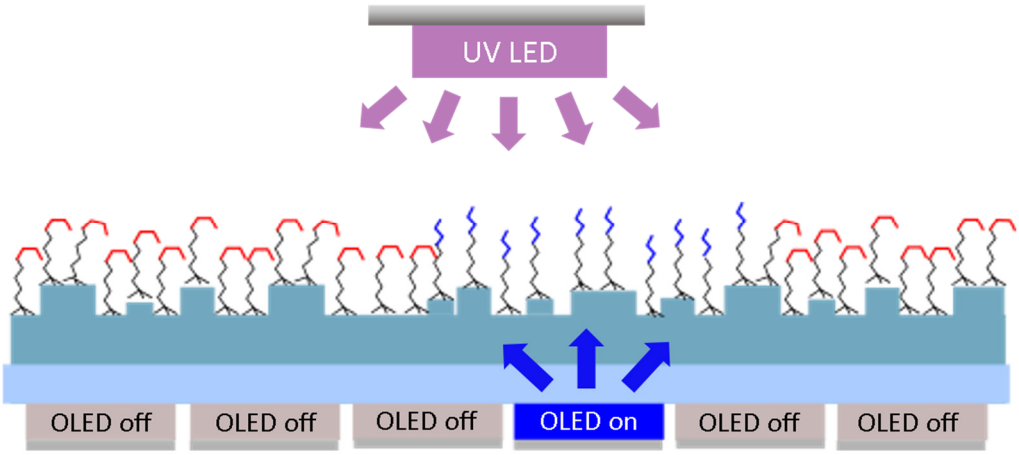

Figure 5-1: Schematic of blue OLEDs put on the back of a substrate covered with photochromic molecules.

The two different photochromic molecules (azobenzene and spiropyran) used for the switchable surfaces developed in this work possess the advantage of needing light in the same wavelength range to be switched from one state to the other and back. Switching of *trans* azobenzene or spiropyran to the metastable state (*cis* azobenzene or merocyanin) is achieved by UV light between 350 nm and 370 nm and the back switching can be most efficiently fastened with blue light in the range of 430 nm and 460 nm as was already explained in Chapter 2. Unfortunately, the performance of UV OLEDs is very poor so far. They hardly deliver light in the wavelength range needed and last for an extremely short time [24], [25], [154]–[156]. There is not only the problem of the high band gap needed to achieve UV emission, but also the effect of the UV light destroying the emitting molecules, which has been a similar problem in blue OLEDs for a long time. Developing blue OLEDs is instead much more feasible these days.

Blue OLEDs for switching photochromic molecules

First, it was looked for phosphorescent emitter material as it is supposed to deliver a higher efficiency, but it turned out that the lowest spectral emission profile came from Bis(2,4-difluorophenylpyridinato)tetrakis(1-pyrazolyl)borate iridium(III) (short: FIr6), which was not as deep blue as needed. So, it was decided to use the fluorescent emitter 4,4'-Bis(9-ethyl-3-carbazovinylene)-1,1'-biphenyl (BCzVBi). It was used with the suggested host material 4,4'-Bis(2,2-diphenylethenyl)-1,1'-biphenyl (DPVBi) [157], [158]. Compared to the stack developed by KIM [157] only the thickness of the LiF was reduced from 2 nm to 0.6 nm and a molybdenum(VI) oxide MoO_3 was introduced. LiF reduces the work function of aluminum and thereby increases the electron injection [99]. The MoO_3 is supposed to generate additional holes and thereby enhance the performance of the final device [159]–[163]. As a consequence, the layer of n,n'-

bis(naphthalen-1-yl)-N,N′-bis(phenyl)benzidine (NPB) could be reduced from 50 nm to 20 nm.

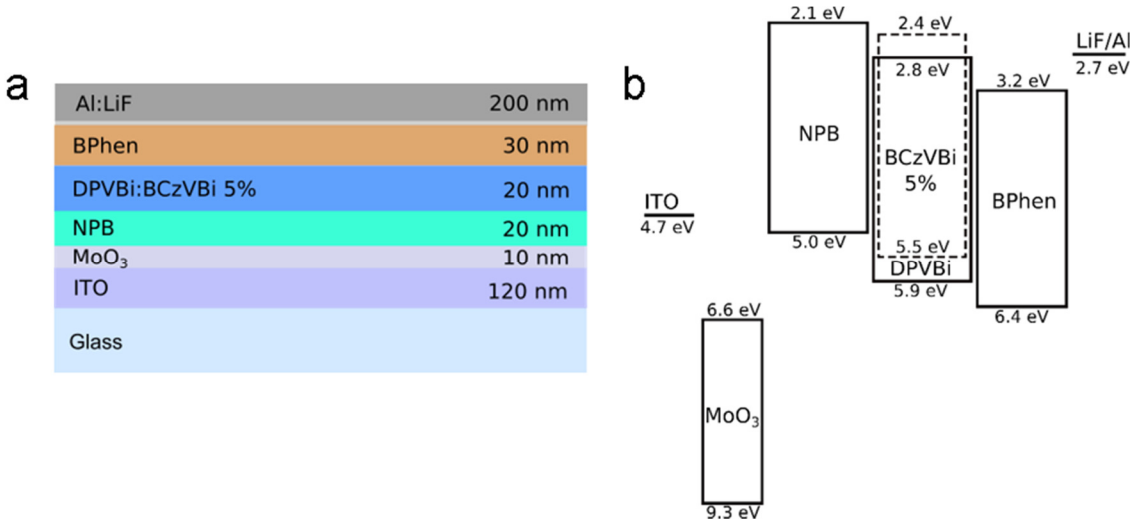

Figure 5-2: Stack (a) and energy diagram (b) for blue OLED with BCzVBi.

Due to the amount of research papers on TADF emitter [93], [97], [164], [165] and the chance to use even more efficient devices, it was at a later point also tried to use an appropriate material of this emitter type. Especially, 9,9',9''-(5-(4,6-diphenyl-1,3,5-triazin-2-yl)benzene-1,2,3-triyl) tris(9H-carbazole) (DCzTrz) promised quite a suitable emission spectrum [166]. The best device fabricated with this emitter in the time span of this thesis work was actually realized by a group of students, who participated in an optoelectronic lab at the group of integrated systems and photonics (Mike Schloh, Karoline Wilma, Pascal Gliesche). The stack of the TADF OLED is given in Figure 5-3.

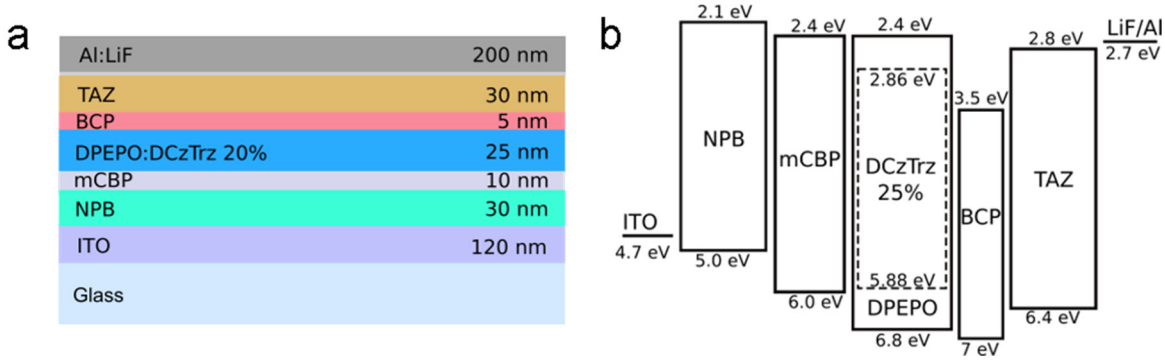

Figure 5-3: Stack (a) and energy diagram (b) for blue OLED with DCzTrz.

The emission spectra of both fabricated OLED types are comparable and shown in Figure 5-4a. The DCzTrz OLED has got a little broader spectrum and a part of the

BCzVBi OLED's spectrum has got a little extra shoulder on the more favorable side. These two facts make the BCzVBi OLED a little more attractive in respect of the application requirements.

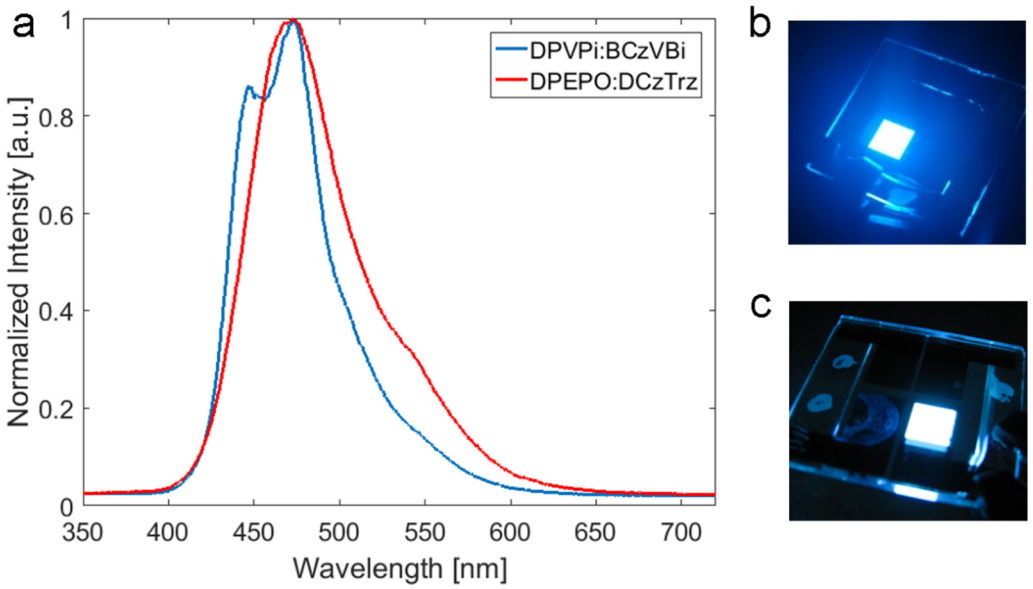

Figure 5-4: Emission spectra of the blue OLEDs (a) and photos of a BCzVBi (b) and a DCzTrz (c) OLED.

The biggest advantage of the BCzVBi OLED becomes visible when having a look at its provided radiant flux compared to the TADF OLED. From Figure 5-5, one can clearly see the enormous difference of their produced light power. The DCzTrz might consume much less current and is in the end more efficient, but in this case this is of minor interest. Due to the higher light power, the BCzVBi OLED was used for all switching experiments with the photochromic molecules.

Many other OLED stacks with the two different emitter materials were fabricated, but only the best concepts for each emitter are shown here.

Both OLEDs lasted at least over one year outside an inert atmosphere, which states their stability. For the experiments, the degradation in operation is more important. For the BCzVBi OLED this is shown in Figure 5-6 at the operation point for the switching experiment performed later. First, the current and the radiant flux are increasing, but after two minutes a continuous degradation sets in.

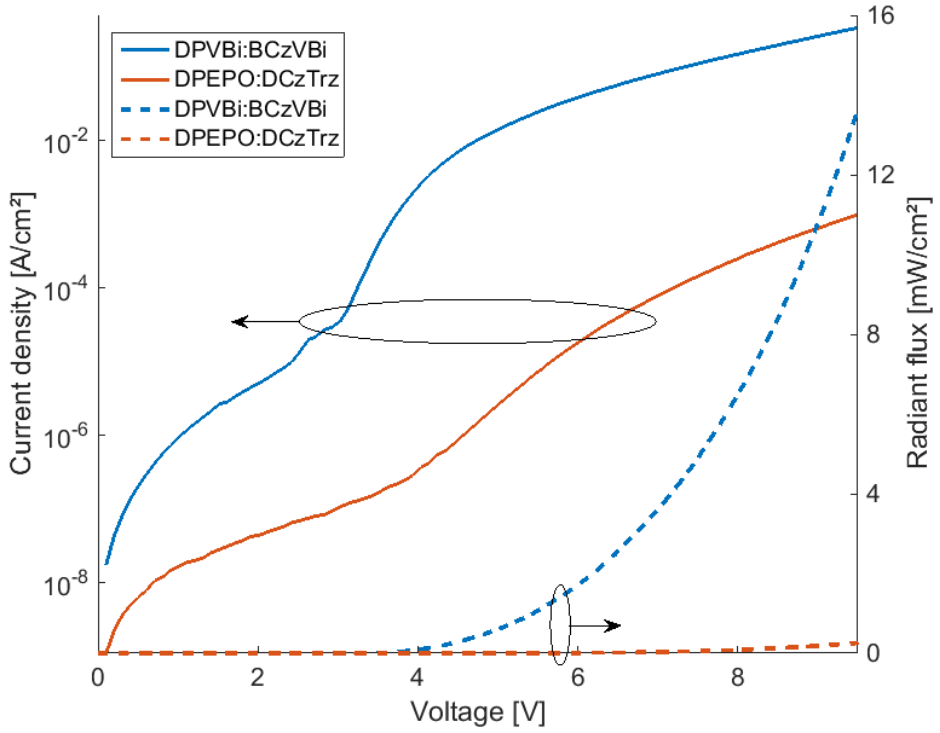

Figure 5-5: Voltage-current-curves and radiant flux of the blue OLEDs.

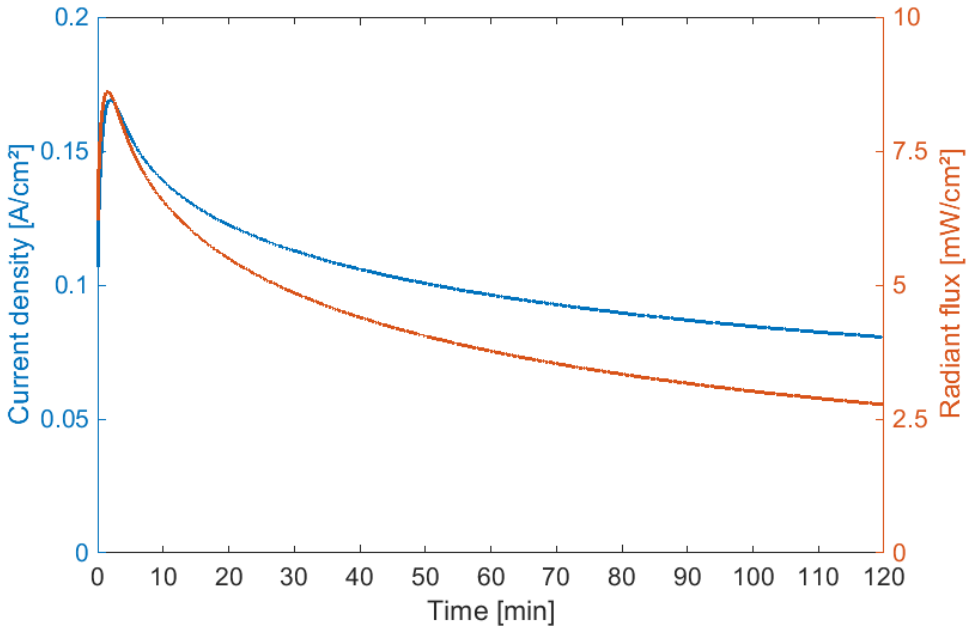

Figure 5-6: Degradation in operation of BCzVBi-OLED at a voltage of 7 V.

Temporal reaction of azobenzene layers on OLED irradiation

In the following part the reaction of different azobenzene layers is characterized to get an impression of how long these surfaces have to be irradiated with an OLED to achieve a full switching in combined systems. Unfortunately, it is not possible to predict the energy needed to switch a layer of photochromic molecules, because the changes in quenching due to density differences of the molecules are difficult to predict [42], [43]. Therefore, each surface has to be characterized individually. The different surfaces were always exposed to UV light until they were fully in the *cis* state and afterwards successively irradiated with blue light of the BCzVBi OLED described in the first part of this chapter. The OLED was always driven at 7 V, which resulted in an average radiant flux around 4 mW/cm².

The first trial of these experiments was performed on azobenzene hosted in a PMMA matrix. Therefore, we used a process developed by PAKULA [45]. The chemical structure of the azobenzene is shown in Figure 5-7. 28 mg of (4'-Hexyl-phenyl)-[4(propyl-butoxy)-phenyl]-diazene (ether-2), 42 mg PMMA and 7 ml toluene were mixed under a nitrogen atmosphere and then spincoated on top of a glass substrate. After drying for one hour, the samples were taken out of the glove box and characterized in an UV/VIS spectrophotometer (Perkin Elmer Lambda 650).

The first measurement gave the data for the *trans* state. Before the second measurement the sample was exposed to UV light by a Nichia NCSU033B LED (96 mW/cm²) for 30 s to the *cis* state. The absolute difference in absorption was quite high on this sample, because the number of photochromic molecules is much higher, when mixing it into a hosting matrix material. Then the sample was irradiated with the blue light of the OLED for different time spans until the *trans* state was reached again.

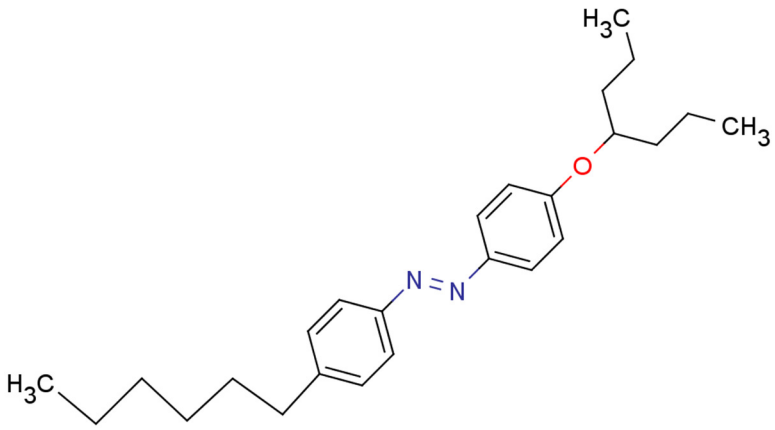

Figure 5-7: Chemical structure of (4'-Hexyl-phenyl)-[4(propyl-butoxy)-phenyl]-diazene (ether-2).

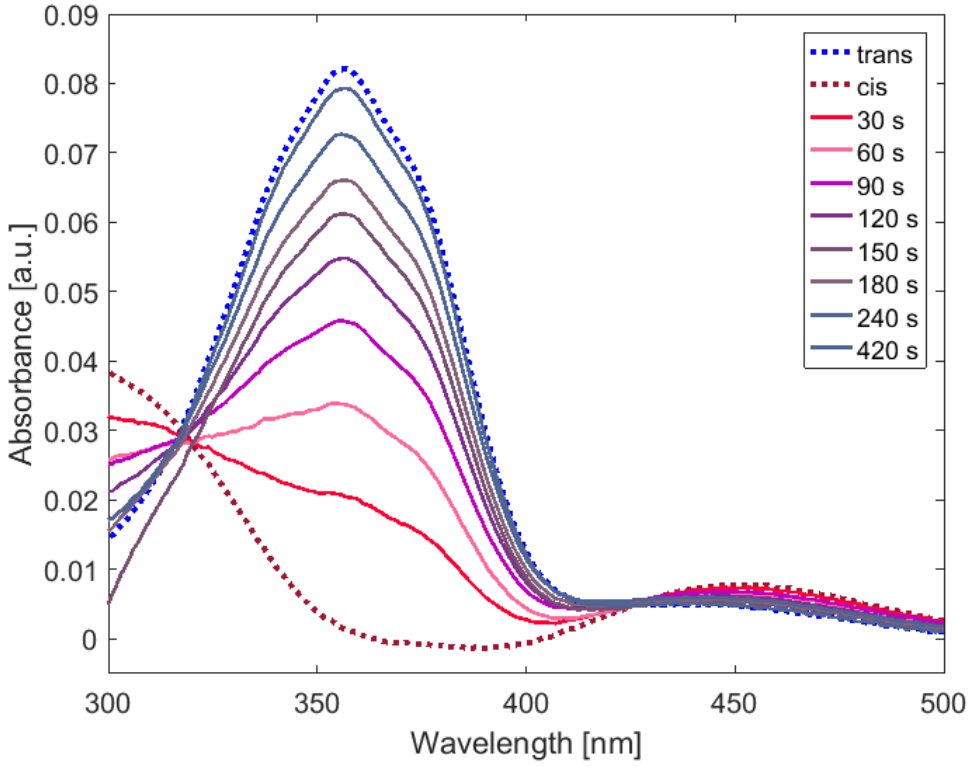

Figure 5-8: Absorption data of successively switched azobenzene in PMMA matrix by blue OLED (*cis* to *trans*).

Over 420 s were needed for a back switching, which is a much longer time compared to the time needed with an inorganic high power LED (30 s) that has got around 50 mW/cm². The OLED instead provides just one tenth of this radiant flux.

Next, the surfaces described in Chapter 3 shall be switched by an OLED. A flat glass substrate and a lotus PDMS structure functionalized with a 1:1 mixture of OCF3-AZO and an alkyne were investigated. The characterization procedure was the same as for the samples with the azobenzene in a PMMA matrix. The results can be seen in Figure 5-9 and Figure 5-10. Clearly visible is the low number of molecules on the flat glass substrates resulting in a very low absorption and it seems that a further switching is not possible after 240 s of OLED irradiation to the sample. Only a high power LED was able to convert the azobenzene layer back into the full *trans* state.

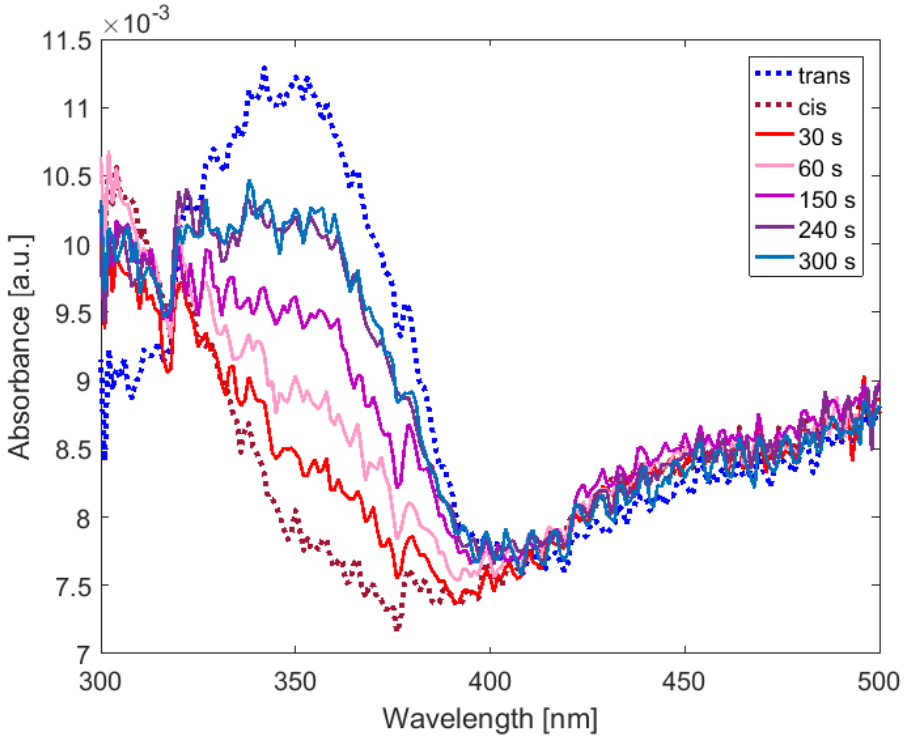

Figure 5-9: Absorption data of successively switched azobenzene covalently fixed on a glass substrate by blue OLED (*cis* to *trans*).

On the lotus PDMS structure instead the number of azobenzene molecules is much higher. This effect was already discussed in Chapter 3. Interestingly, it was possible to achieve an alomst complete back switching by an OLED in this case. After only 4 min of excitation by a simple blue OLED 80 % of the azobenzene molecules functionalized on the PDMS surfaces could be switched. This states that an OLED is able to strongly fasten the *cis-trans* isomerization and is therefore suitable as an on-chip light source

for photo-switchable surfaces and sensors. Figure 5-11 shows an OLED irradiating a lotus PDMS structure.

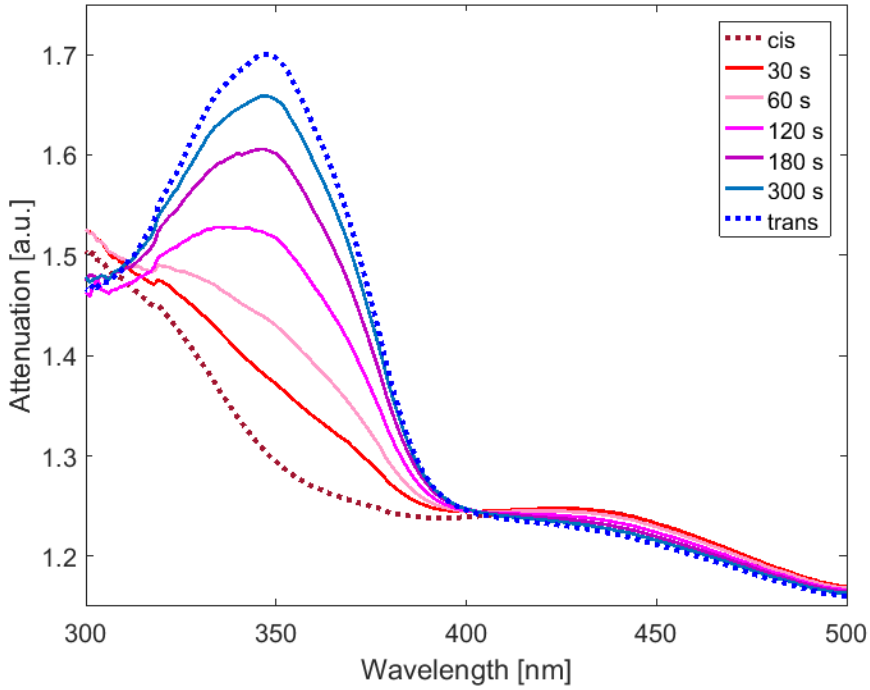

Figure 5-10: Absorption data of successively switched azobenzene covalently fixed onto lotus PDMS structure by blue OLED (*cis* to *trans*).

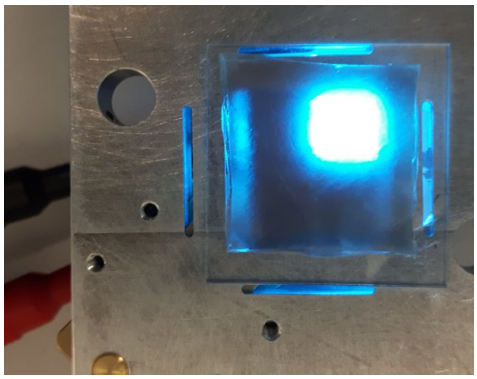

Figure 5-11: Operating OLED beneath a lotus PDMS sample.

Wettability switching with spiropyran and OLEDs

This part is supposed to show another application for the usage of photochromic molecules together with OLEDs. As described in previous chapters it took already quite a lot of effort to achieve photo-switching of the contact angle on a surface. One problem is the interplay between molecule density, molecule orientation and the surface structure. Very many combinations and especially all functionalizations by the "click chemistry" approach are not realizing any differences in the surface energy and thereby no wettability changes. Another point is the need for transparency, which leads to enormous restrictions in terms of substrate and structure usage. Transparency would be needed to put the OLED directly on the back of the substrate that is covered with photochromic molecules, but up to this very moment there has no work about a transparent, photo-switching wettable surface been published.

Though not perfectly stable and not transparent, the spiropyran surfaces presented in Chapter 4 are able to provide a clearly detectable wettability switching. Unfortunately, the lifetime of the merocyanin is quite short and this means that the contact angle is already switched back within a short time in darkness. Figure 5-12 illustrates the results of an experiment, where the difference of darkness and blue light irradiation with a BCzVBi OLED on the isomerization process from merocyanin to spiropyran was compared. The switching to merocyanin was again realized by a high power UV LED and this resulted in a decrease of the contact angle from 132° to 78°. Afterwards, the surface was irradiated by the blue light from the OLED for 200 sec or was just left in darkness for the same time. The radiant flux of the OLED was around 4 mW/cm² in this case. Every time the OLED was used the contact angle difference was higher. In average the increase was 42 % higher than after the sample had been left in darkness. When operating the OLED with a lower current and consequently a lower radiant flux, there was no difference obtainable once it got lower than 1 mW/cm².

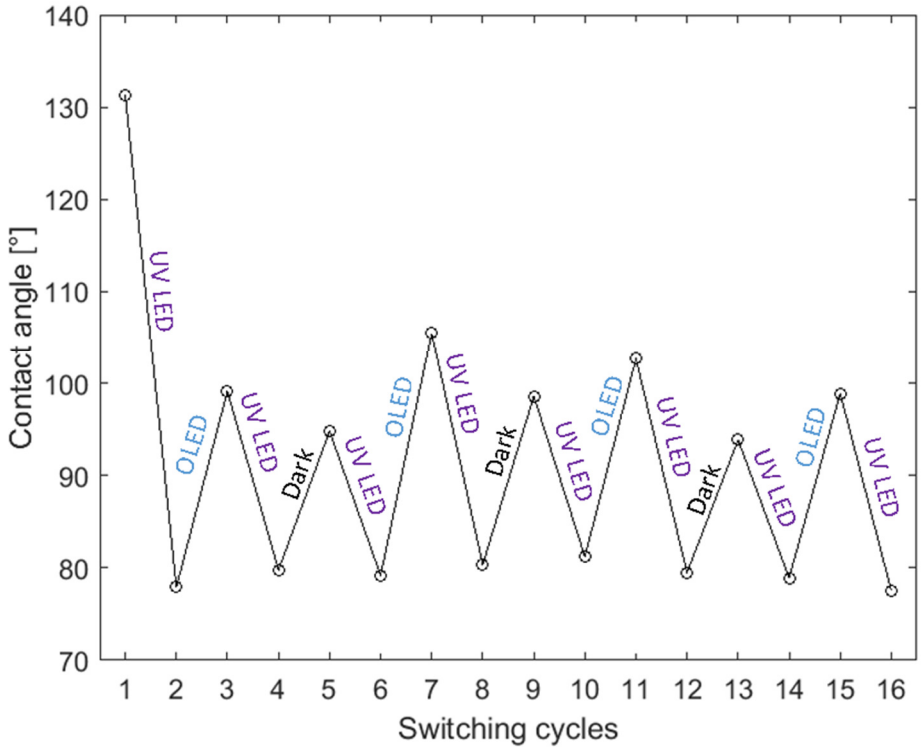

Figure 5-12: The difference of wettability switching on a spiropyran coated candle soot surface between darkness and OLED irradiation.

Discussion

Two different blue OLED types were developed: One with a fluorescent- and one with a TADF emitter. The radiant flux provided by the developed BCzVBi stack was quite high for an OLED with up to more than 10 mW/cm². Afterwards, it was shown successfully that OLEDs are suitable devices for the excitation of photochromic molecule layers. Still, due to their lower radiant flux the time of excitation is higher compared to the use of inorganic LEDs. Absorption and wettability were switched with the help of an OLED. By the absorption switching with the BCzVBi OLED through the substrate a device with a "programmable" surface was realized, which could be used for a spatial control in sensors or microfluidics.

The use of OLEDs in combination with a photochromic molecules requires an avoidance of additionally absorbing layers. As, e. g., in case of the wettability

switching, where the candle soot layer is completely untransparent and thereby complicating the system integration. This states again that for the combination of photochromic molecules and OLEDs in one device / system, both the photo-switchable layers and the OLEDs have to be optimized.

Chapter 6.

T-ZnO particles for substrate mode scattering

As already described in Chapter 2, quite a high amount of the light generated in the emitting layer of the OLED is trapped inside the substrate. The light may be scattered out of it by incorporated nanoparticles [26], [27]. *This may then result in an increase of efficiency. Tetrapodal zinc oxide (t-ZnO) particles were inserted into a polymer, which was then formed to foils by the company Phi-Stone AG (former FUMT R&D Functional Materials GmbH). Here, these foils were optically characterized. A sample showed a haze of around* 50 %. *The actual t-ZnO content was varying quite intensively, which made it difficult to perform comparisons. For the OLED stack that was fabricated on top of these foils, a gold anode was employed as semitransparent anode. The high surface roughness of the foils led to the need of PEDOT:PSS as a smoothing layer, which made the final devices more efficient, but darker in the end. The OLED devices on the t-ZnO containing substrate were brighter, but in the end not more efficient and not brighter than devices without t-ZnO and the PEDOT:PSS.*

This work was conducted in cooperation with the Interreg project "RollFlex".

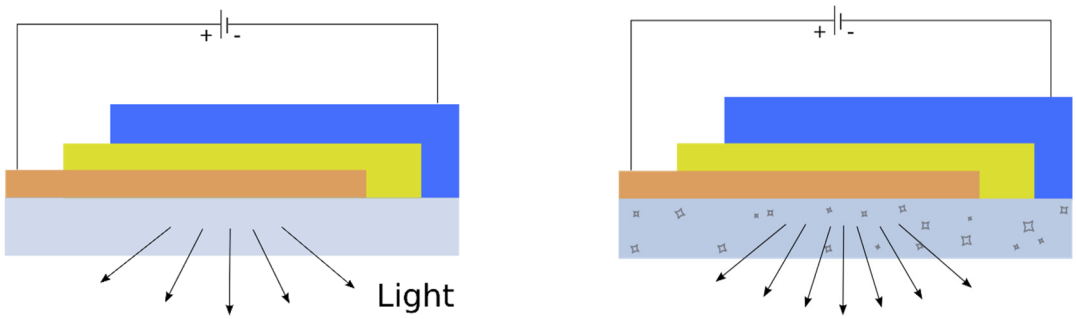

Figure 6-1: Schematics of simple OLED stacks on different substrates without and with scattering particles.

The extraction of light from the substrate is less difficult than the outcoupling of guided modes. The most efficient way to do this is to put a big half sphere beneath the substrate [10]. On the other hand, this is very unpractical for many applications and subverts the advantage of the OLED being a very thin device. An often-used alternative are microlens arrays [10], [167], [168]. Already a simple roughening, e. g., by sandblasting helps to improve the efficiency of an OLED by scattering out the substrate modes [169], [170]. Especially for substrates made of flexible polymers it is attractive to mix scattering particles into the substrate material [27]. All three described methods are schematically depicted in Figure 6-2. Here, the configuration from Figure 6-2c is realized by mixing t-ZnO particles into the OLED substrate and gold was used as transparent flexible anode material.

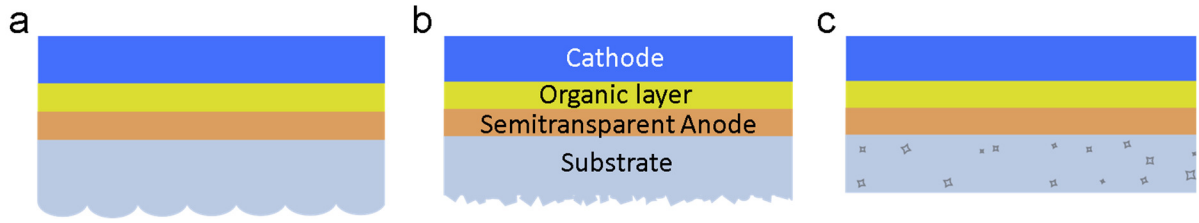

Figure 6-2: Schematics of OLEDs on different modified substrates: (a) with lenses; (b) with rough surface; (c) with integrated particles.

Gold as an anode for OLEDs

Gold (Au) is a precious material and known for its good electrical conductivity, which is the reason for the frequent use of Au in electrical devices and conductor plates. In fact, it possesses a quite high conductivity even if just applied as very thin layer. As shown in the graph in Figure 6-3, the sheet resistance of a 8 nm Au layer is already low enough to be suitable for an OLED electrode. A good indium thin oxide (ITO) layer that is usually used for an anode in an OLED has got a sheet resistance of 15 Ω to 50 Ω. A drawback that often follows with a high conductivity is a high absorption and indeed even thin layers as 10 nm of Au are showing a transmission of under 50 % (Figure 6-4). In this respect, ITO is much better, but with the trend to flexible devices [12], [171], [172] another problem of ITO comes into account: it is a

metal oxide and all of those are rather brittle as solid layers on flexible substrates. ITO does not survive bending radii smaller than 2 mm [173]. The price of ITO is also quite high and therefore the cost differences are negligible.

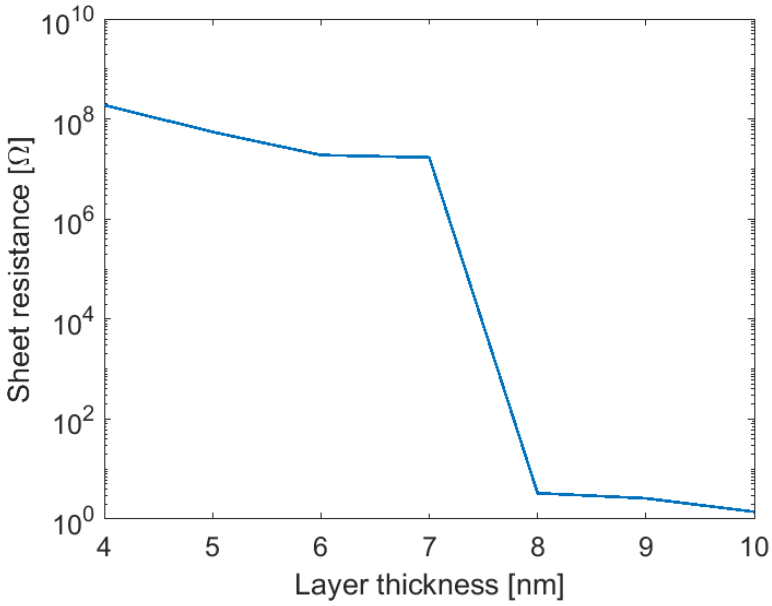

Figure 6-3: Sheet resistance of thin gold layers measured by four-point probe method.

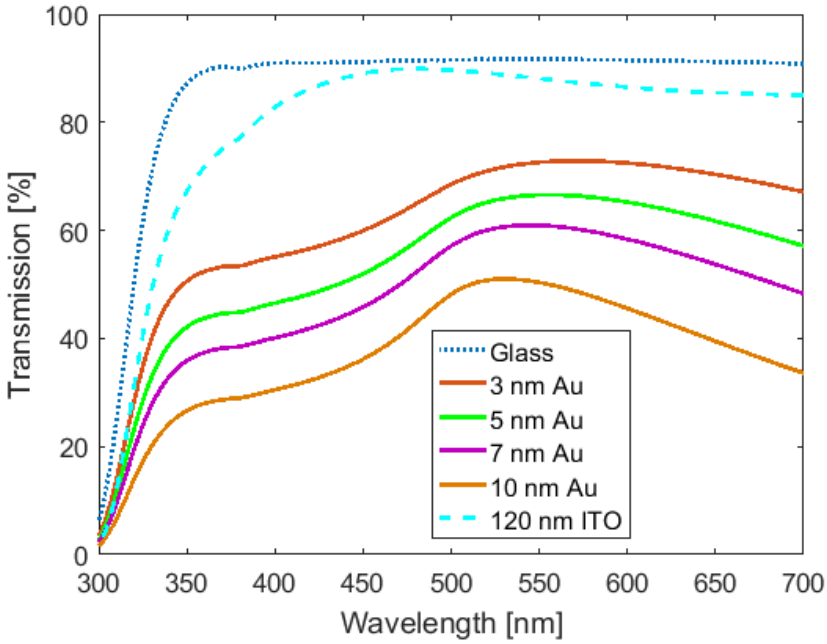

Figure 6-4: Transmission of thin gold layer on glass compared to bare glass and a typical ITO layer.

Fabrication of OLEDs with t-ZnO containing substrates

There are very many different forms of ZnO particles: spherical, needle, core-spike particles, hexagonal nanorods, tetrapods etc. [174]–[176]. The particles used here were produced by a simple flame transport synthesis resulting in ZnO particles with a tetrapodal shape as shown in the SEM image in Figure 6-5 [174], [175].

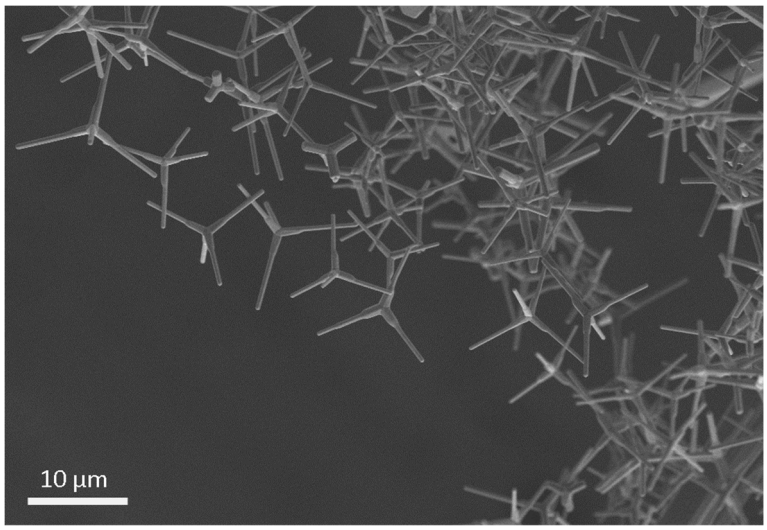

Figure 6-5: SEM image of t-ZnO; Printed with permission of: Phi-Stone AG, Kiel.

Different amounts (0 wt%, 0.1 wt%, 0.5 wt%, 1 wt%, 3 wt%) of tetrapodal ZnO (t-ZnO) particles were mixed into a polymer, polythiurethane (PTU). This mixture was then cured to foils with 1 mm thickness. PTU is highly transparent in the visible and near infrared spectrum, solvent free and can be fabricated as thin foil or used for coatings. The Phi-Stone AG performed the fabrication of the foils. Details for their fabrication can be found in [177], [178].

The substrates were cleaned in an ultrasonic bath with acetone and isopropanol for 10 min and then at 70 °C dried for 2 hours. Afterwards, an 8 nm layer of Au was thermally evaporated on the t-ZnO-PTU. Unfortunately, the substrates were not as smooth as usual float glass. This lead to quick breakdowns of the devices. The problem was solved with an additional layer of poly(3,4-ethylenedioxythiophene) doped with poly(styrene sulfonate) (PEDOT:PSS). This layer flattened the substrate and helped to

ease the hole injection. PEDOT:PSS comes as a liquid and was deposited using a spincoating step with 3500 rpm, but this required a short treatment with an oxygen plasma (100 W RF, 40 s) to enhance the adhesion of the PEDOT:PSS on the PTU. Then a 10 nm layer of MoO_3 was evaporated to enhance the hole generation at the anode side. A layer with 30 nm n,n′-bis(naphthalen-1-yl)-N,N′-bis(phenyl)benzidine (NPB) acted as a hole transportation layer and 50 nm of tris-(8-hydroxyquinoline)aluminum (Alq_3) as emitting layer. Due to the fact that the cathode follows immediately on top of the emitting layer, this layer was made quite thick. Both layers were thermally evaporated as well as the cathode materials: 1 nm lithium fluoride (LiF) and 200 nm aluminum. The complete OLED stack is shown schematically in Figure 6-6. In order to prevent the devices from fast degradation, they were encapsulated with epoxy adhesive and another small PTU foil.

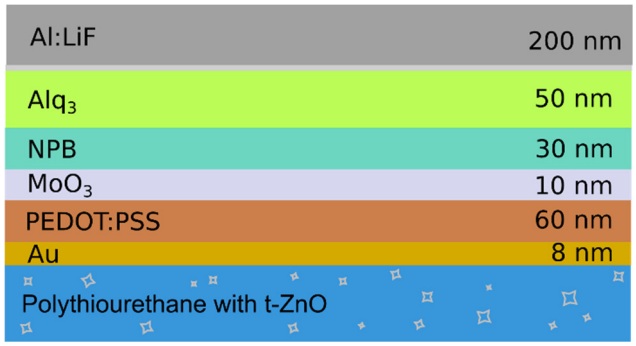

Figure 6-6: Schematic of OLED stack on t-ZnO-PTU substrate.

Optical characterization of the substrate

Before the device characteristics of the OLEDs were measured, the optical performances of the substrates were characterized with the scattering as main interest. The photographs of the foils in Figure 6-7 are already stating that the scattering increased with a higher t-ZnO particle content, but this photo has to be treated with reserve as the actual particle content and distribution varied quite intensively in the foils.

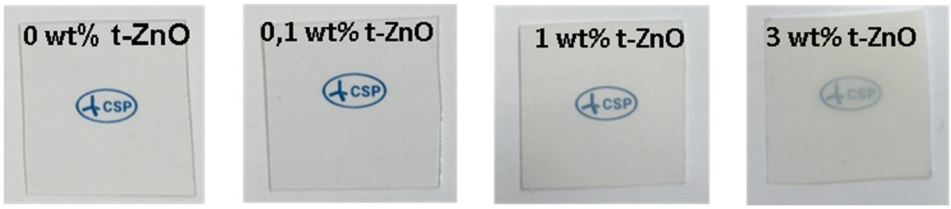

Figure 6-7: Photographs of PTU foils with different t-ZnO content.

The following detailed measurements of the scattering were only performed exemplarily for PTU with 1 wt% due to the time-consuming nature of these measurements. They were conducted thanks to the help of Dr. Klaus Jäger at the Helmholtz-Zentrum Berlin for Materials and Energy.

The standard measurement for the characterization of scattering layers is the haze measurement. For this measurement the sample is placed in a beam in front of the opening of an integrating sphere, which is equipped with a photodiode 90° away from the sample opening. Then two different transmission values are determined. The first is the total transmission of the sample and for the second value, a hole on the opposite of the sample opening is used. It can be left open or filled with a strong damping material. Thereby, the light of the beam that directly passes the sample (±2.5° to beam normal) will not be included in this measurement. Dividing the total transmission by the second value gives the haze. Here, it was measured with PerkinElmer Lambda 950 UV/VIS spectrometer together with a classical expansion device for the haze characterization. The result is depicted in Figure 6-8. The haze stays at 50 % for the whole visible range. The reasons for this are the low absorption of ZnO which increases just beneath 400 nm and the fact that the particles most probably are strongly accumulating, which means that geometrical optics have to be applied.

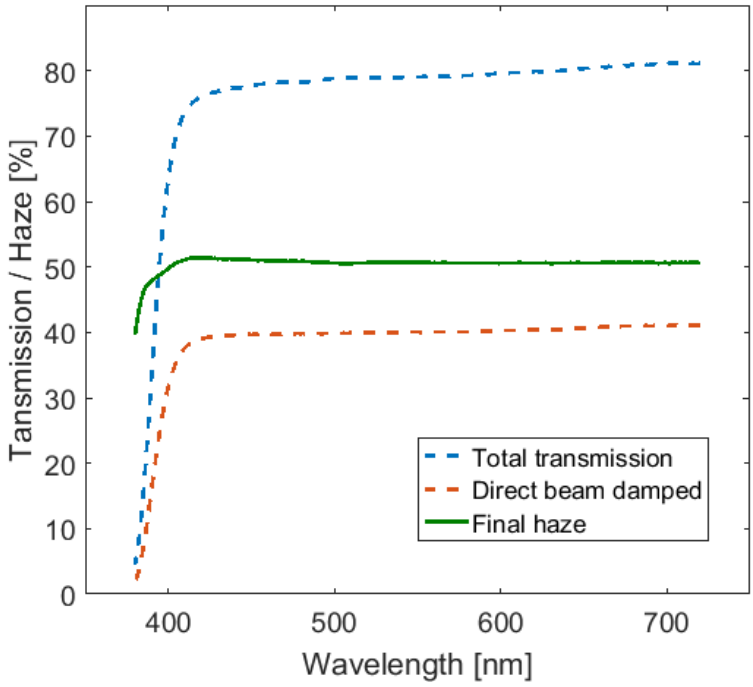

Figure 6-8: Results for haze measurement; no wavelength dependency in the visible range because absorption is low and the particles are large.

The haze measurement has one strong drawback: You do not get to know in which direction the light is scattered [179]. It could be all scattered into ±5° to the beam normal or within ±50°—the haze values would be the same. Therefore, also angle-dependent scattering measurements were conducted with the same UV-VIS spectrometer, but with a special automated reflectance / transmittance analyzer (ARTA) [180]. The result of the angle-dependend measurement is shown in Figure 6-9. It shows that though 50 % of the light were scattered over the ±2.5° border of the haze definition, all the rest of the light is still scattered quite close to the beam normal.

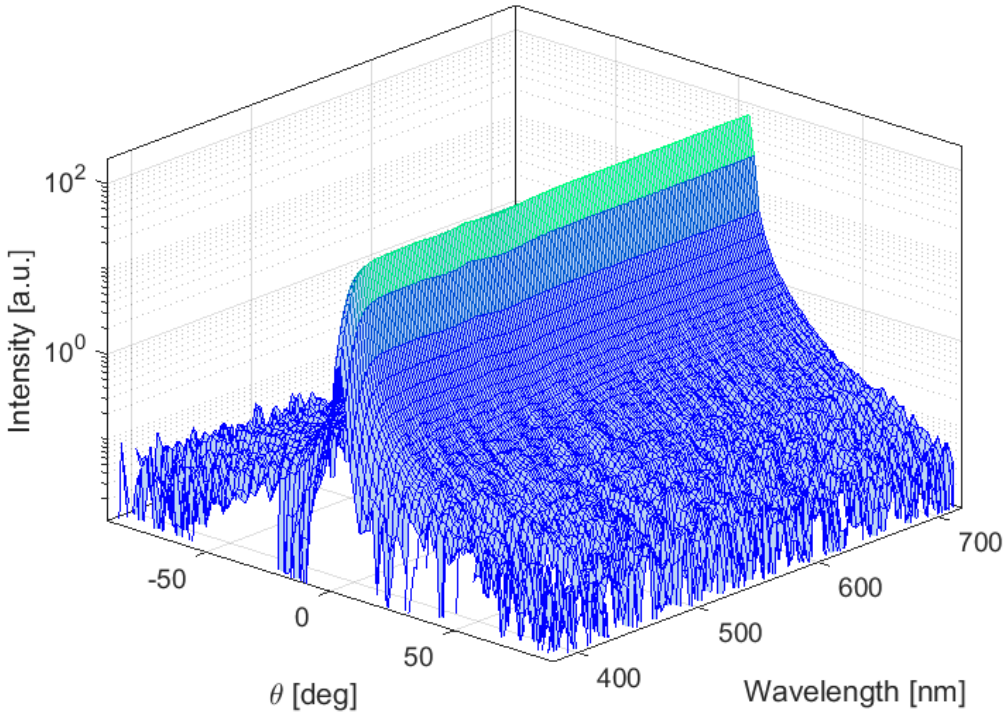

Figure 6-9: Angle and wavelength resolved measurement of scattering PTU with t-ZnO.

Electroluminescene characterization of OLEDs on t-ZnO substrates

Now the device characteristics of the OLEDs will be described. The samples were run with a source-measurement unit by Keithley (Modell 2400). An example of an OLED in operation is shown in Figure 6-10. It was fabricated on a little thinner substrate to allow a better bending. Figure 6-11a depicts the current-voltage curves of devices with and without t-ZnO in the PTU substrate. The sample with t-ZnO is showing some leakage current from 0 V to 2 V which is caused by an inhomogeneity of the stack due to a higher surface roughness of the substrate. Spectral measurements revealed that the emission spectrum of the device becomes a little narrower with an increasing t-ZnO particle content in the substrate. The light in the range of 600 nm to 700 nm is proportionally reduced (Figure 6-11b).

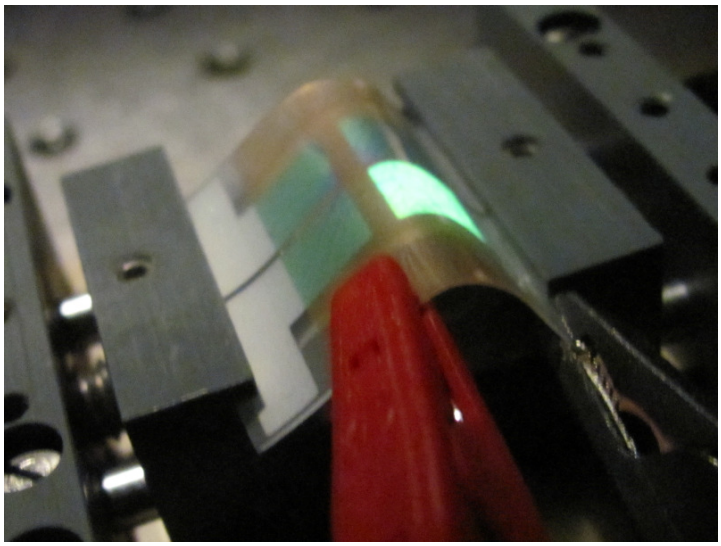

Figure 6-10: Photograph of bended OLED on PTU substrate.

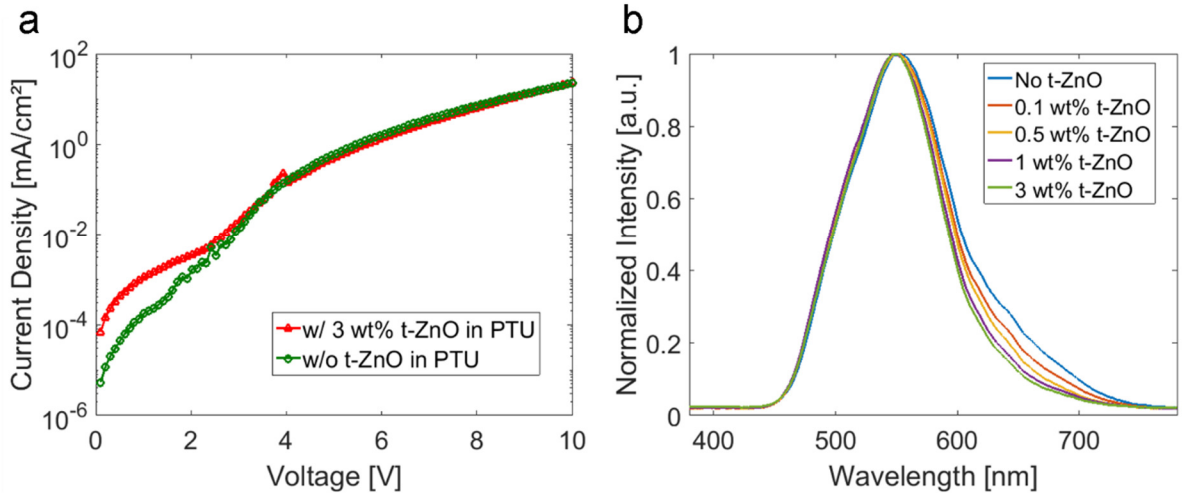

Figure 6-11: (a) current-voltage curve and (b) normalized emission spectra of OLEDs on PTU substrate with and without t-ZnO.

The emitted light of the OLED was measured with a calibrated photodiode on which the samples were lying directly during the measurement. After a weighting of the measured photocurrent with the responsivity curve of the photodiode and the emitting spectrum, the radiant flux can be obtained. The radiant flux is plotted against the applied voltage in Figure 6-12. In this figure two examples for each substrate are given. The radiant flux of OLEDs on substrates containing low amounts of t-ZnO particles is a little bit higher (about 30 %). In Figure 6-13 the wall plug efficiencies of the same samples are given. The OLEDs on pure PTU are showing a typical efficiency

roll-off, which is not present on substrates that are containing t-ZnO particles. Unfortunately, the efficiency variations are too high to state which is the best t-ZnO content.

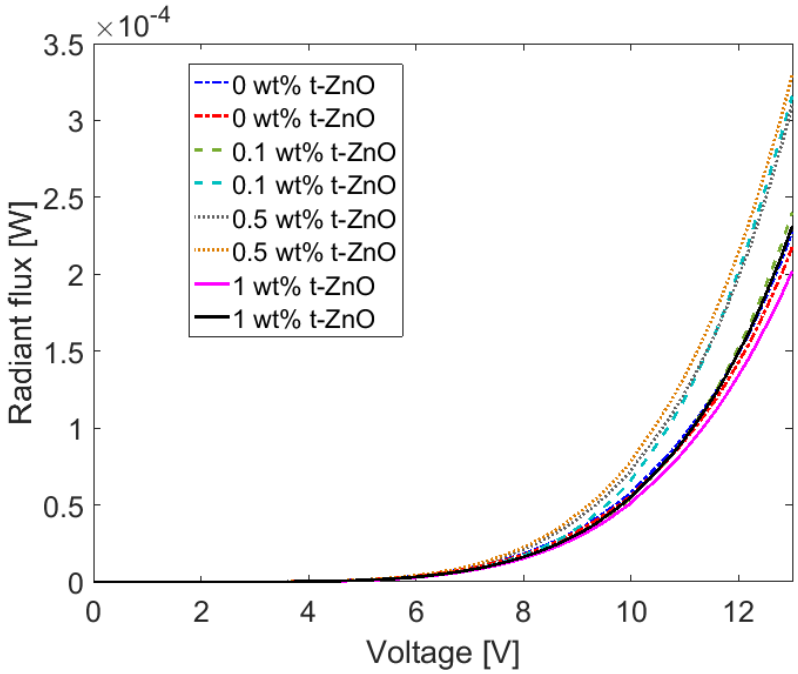

Figure 6-12: Radiant flux of OLEDs on different t-ZnO-PTU substrates.

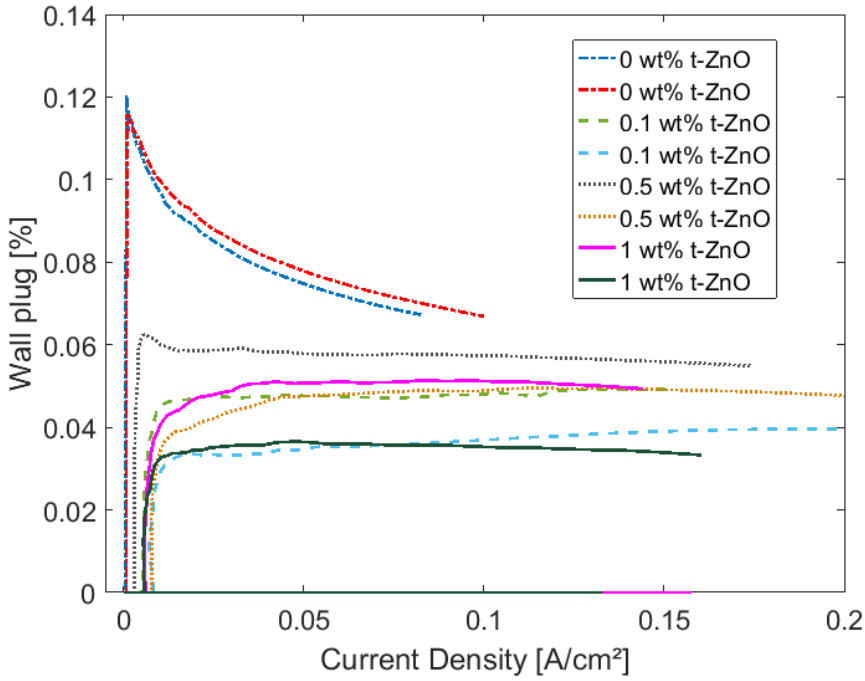

Figure 6-13: Wall plug efficiencies of OLEDs on PTU substrates with t-ZnO particles; roll-off disappears, when particles are included in the substrate.

Discussion

The fabrication of OLEDs on t-ZnO containing substrates was successful and it was possible to get about 30 % more light out of devices with low t-ZnO content (Figure 6-12). The ideal particle content could not be determined as the final particle contents in the foils were varying intensively without showing a connection to the particle content given into the polymer during the substrate fabrication. Unfortunately, the OLEDs did not become more efficient, but instead the efficiency roll-off disappeared completely. Although it is unwanted, the roll-off is actually a typical effect in light emitting devices. Even in inorganic LEDs there has been a lot of afford to understand and efface this effect, which is called "droop" there [181]. At the moment this effect is mostly explained due to Auger losses [182]. In OLEDs, the reasons for this effect as, e. g., different annihilation processes are more diverse and only some of them have been partly explained [183]. So, the understanding of the disappearing roll-off effect needs some more profound investigations here. Fact is that obviously some t-ZnO particles are reaching out of the PTU. ZnO is a semiconducting material and can be also used as hole injection material [184] or, in combination with an aluminum doping even as electrode [185]. These electronic properties of the ZnO might be the reason for changes of the emission spectrum (Figure 6-11b). The emission zone in the OLED must have been moved because a reduction in the red cannot be explained with a higher absorption due to a higher particle content. The particle parts that are reaching out of the substrate and other surface inhomogeneity have been the reason for the use of PEDOT:PSS to smoothe the surface. This smoothening made the OLEDs more efficient but led to a reduction of the radiant flux due to the absorption of PEDOT:PSS. As follows, for the excitation of photochromic molecules these developed substrates are currently not useful. A simple thin coating of a polycarbonate substrate with a t-ZnO containing polymer did not show any positive effects. For future work, it would be important to focus on the prevention of particle accumulation during the incorporation

in the PTU and on smooth surfaces to avoid further effects on the electrical performance of the OLED device.

Chapter 7.

Light manipulation with 1D gratings in OLEDs

This Chapter deals with light directed by non-metal gratings in OLEDs on a mainly experimental basis. It is systematically shown in which way the intensity of the resonances caused by the integrated gratings can be influenced, highlighting the effect of emitter positioning and refractive index contrast. A close position of the emitting layer to a thin metal electrode turned out to be most critical for high resonance intensities. Also the integration of gratings into a fully flexible OLED on PDMS is presented, where a shift of the resonance was induced by stretching the substrate. At the end, the direction of light in multiple directions is shown by the first electroluminescence measurement of an OLED with a multi-periodic grating.

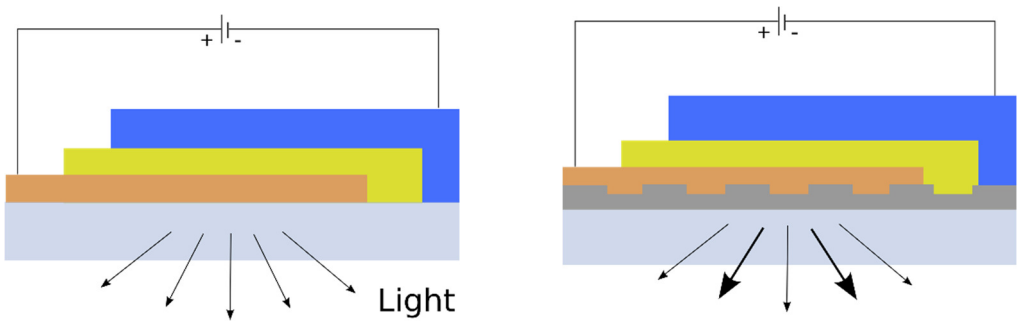

Figure 7-1: Schematics of simple OLED stacks on different substrates without and with an integrated grating.

First, we will have a quick overview of methods for guided mode outcoupling. Similar to the extraction of substrate mode, particles can also be integrated into the organic stack (Figure 7-2a) [186]. This can lead to a higher efficiency by outcoupling of light, which was trapped in guided modes. Often this also leads to a much higher current injection. Both facts are valid for the integration of periodic gratings made of metals [187] (Figure 7-2b) or dielectric materials and polymers [188], [189] (Figure 7-2c). They strongly change the spectral emission characteristic.

An upgrade of the substrate by integration of high-index layers [171] or sub-anode grids [190] can help to couple out guided modes as well.

In this thesis, it is made use of integrated photonic crystals for coupling light into specific directions. For this reason, the theory behind the influence of the photonic crystal on the spectral emission properties is described in more detail.

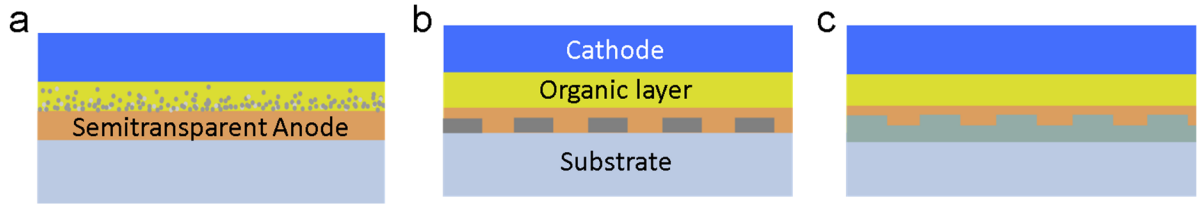

Figure 7-2: Schematics of concepts for guided mode outcoupling: a) particle integration into organic layers; b) integrated metal grid; c) photonic crystals.

Theory and methods for non-metal gratings

In a few words, a photonic crystal (PC) is a structure with a periodically modulated refractive index, where the periodicity is in the dimension of the wavelength of light. The refractive index can be modulated in one, two or even all three dimensions. In OLEDs, these photonic crystals generate resonance peaks at certain wavelengths and angles in the emission spectrum. Here, we have a look at a 1D Bragg grating with the periodicity Λ in x direction [191]. This changes the wavevector k_x to:

$$k'_{xm} = k_x + m\frac{2\pi}{\Lambda}, m \in \mathbb{Z} \qquad \text{(Eq. 7-1)}$$

Now the outcoupling angle for the mode can be calculated with $|\overrightarrow{k'}| = k_0 n^{(i)}$ and (Eq. 2-12):

$$\sin\theta_m^{(i)} = \frac{k'_{xm}}{|\overrightarrow{k'}|} = \left(n_{\text{eff}} + m\frac{\lambda_0}{\Lambda}\right)/n^{(i)} \qquad \text{(Eq. 7-2)}$$

where i is the indication for the layer, e. g., $n^{(\text{air})} = 1$. Figure 7-3 illustrates the principle of this Bragg scattering for the first order (m = -1).

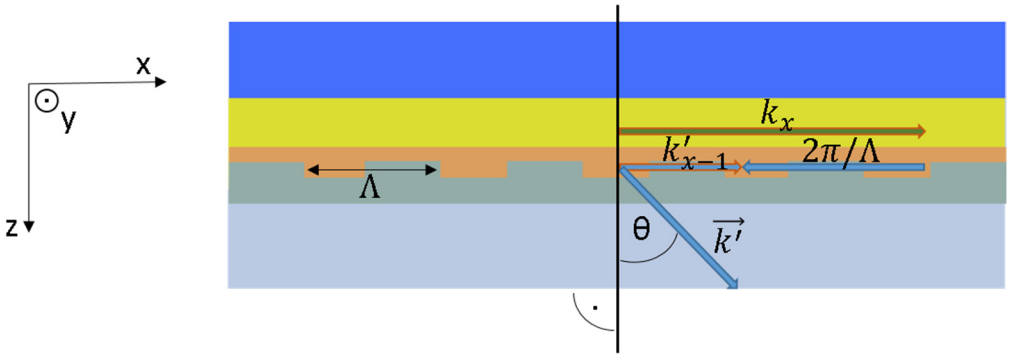

Figure 7-3: Schematic of Bragg scattering at 1D structure. The grating reduces k_x and thereby scatters the mode of the wave-guiding layer.

Gratings are additionally effecting the SPP, but this is of minor interest here. In case the reader is interested in SPP outcoupling or a deeper inside into outcoupling enhancement of OLEDs it is recommended to have a look into SAXENA or BRÜTTING [26], [192].

Fabrication of optical gratings by nanoimprint lithography

Due to the extremely small dimensions of the gratings, they have to be fabricated by costly processes as electron-beam lithography or slightly less expensive alternatives as, e. g., laser interference lithography. For this reason, only master structures were fabricated for this work. The structure of a master can then be transferred into a photoresist by a nanoimprint lithography (NIL) process. This allows for a substantial

cost and time reduction and could be even more efficient in a roll-to-roll process [193]–[195]. Here, a soft NIL was used, where the master structure is first transferred into a PDMS mold. For this, eight parts of Sylgard 184 (DowCorning) were mixed with one part of its curing agent, poured onto the master structure, degassed and finally cured in an oven at 130 °C. This PDMS stamp was used for the actual imprint process, schematically depicted in Figure 7-4. First, the photoresist had to be spincoated on a substrate, e. g., a glass slide. The substrate was thoroughly cleaned in an ultrasonic bath with acetone and isopropanol. Then it was dehydrated at 160 °C on a hotplate for 10 min. After a short cooling of two minutes, the adhesion promoter Amoprime (Amo GmbH) was spincoated at 3000 rpm for 30 s. The sample had then to be baked at 115 °C on a hotplate for 2 min and again cooled for 2 min. Now, the photoresist Amonil MMS4 (AMO GmbH) was spincoated with the same parameters as the adhesion promoter. The PDMS stamp was then positioned on the coated sample and pressed down just using the hand (Figure 7-4a). As shown in Figure 7-4b, the combination of PDMS stamp and the substrate with photoresist was afterwards exposed to UV light for the curing of the resist (1 min with a 350 W mercury vapor lamp). The PDMS stamp could now be removed and a positive copy of the master structure was transferred into the resist structure (Figure 7-4c). Amonil is highly transparent and has the same refractive index as a substrate made of float glass and a thickness of 200 nm after spincoating.

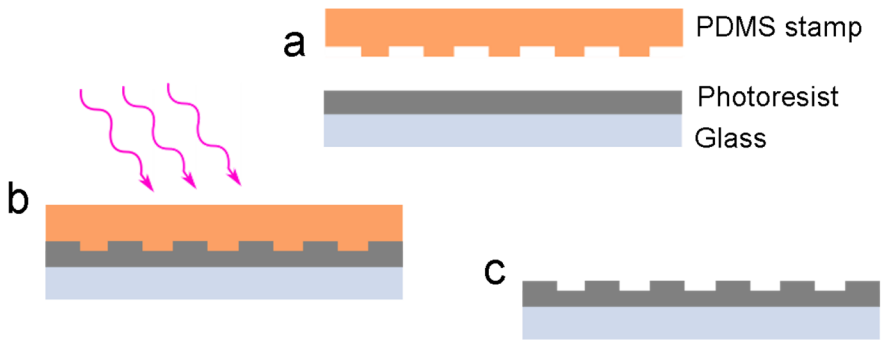

Figure 7-4: Schematic of soft nanoimprint lithography (NIL) process: (a) Pressing PDMS stamp into photoresist; (b) UV curing; (c) final product.

General characterization methods for grating effects

As explained, optical gratings produce an angular-dependent change of the emission spectrum in an OLED. To characterize this effect, it is necessary to tilt the OLED parallel to the grating lines while performing spectral measurements. This can be done with a goniometer that is connected with a spectrometer. Such a setup was constructed by Christian Kluge [196]. It possesses two rotation stages that can be controlled via LABVIEW by National Instruments and the light is tracked by a bare fibre, coupling light into a spectrometer (Andor Shamrock SR-500i) with a cooled CCD detector (Andor DU920P-OE). A schematic of this setup is depicted in Figure 7-5.

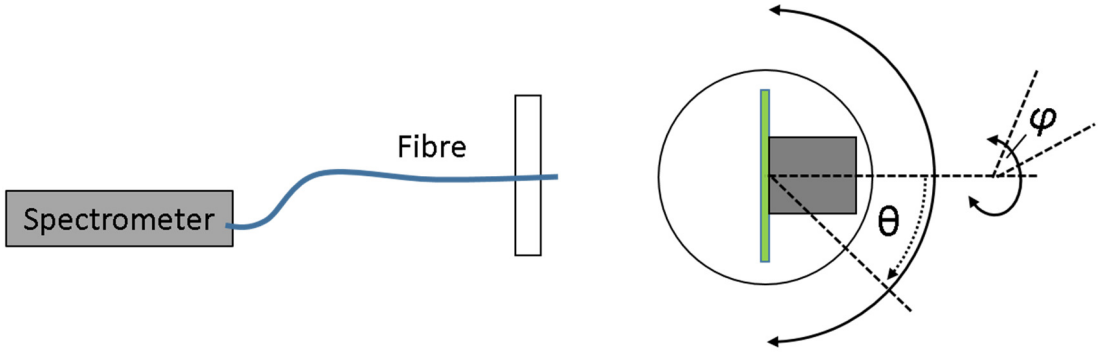

Figure 7-5: Schematic of the goniometer setup from above; sample position colored in light green.

The goniometer setup allows to apply an electric current to an OLED, but the electroluminescence (EL) requires defect-free layers and suitable electrodes, which sometimes is difficult to realize. For this reason, a small laser pointer emitting at 405 nm is mounted with the sample holder on the θ-stage. It can excite the sample in 30° angle to its surface normal. This allows measurements in photoluminescence (PL) and it is practical for the sample positioning. A PL measurement can also help to distinguish between overlaid resonances in EL. This effect becomes important for larger OLEDs because, due to their size, not the complete emitting area is tilted in the rotation center of the stage. Thereby, the resonances seem to broaden and smear in extreme cases. The described problem is illustrated in Figure 7-6.

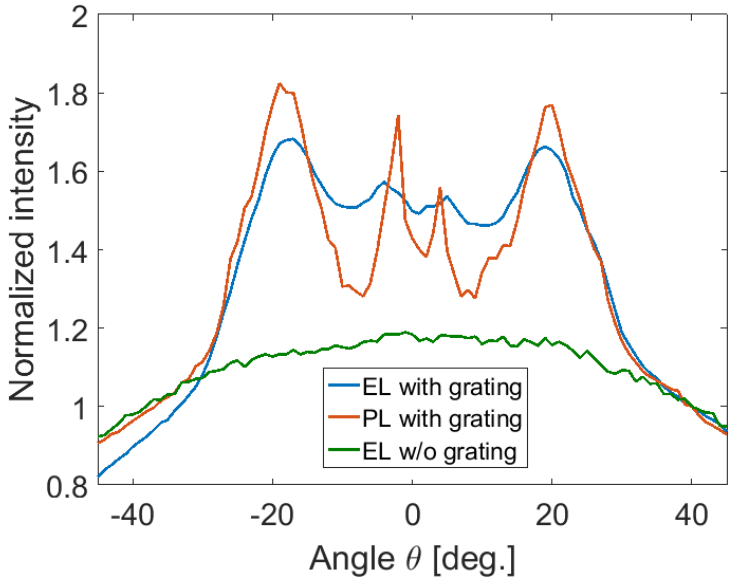

Figure 7-6: Angular emission profile at 540 nm of a 5x5 mm² large Alq_3-OLED with and without a linear grating (period 370 nm) compared to photoluminescence.

In case the samples contained a grating, the PL measurements were sometimes performed for φ = 0° and φ = 90°, as the rotation allowed to get rid of disturbing measurement artifacts as, e. g., excited fluorescence of epoxy adhesive used for the encapsulation. Example measurements are shown in Figure 7-7 and Figure 7-8. After a φ rotation of 90° the resonances should form a perfect arc [197], while there are two deformed arcs crossing each other in Figure 7-8. In fact, the appearance of the resonance is quite sensitive at this angle. To fit Bragg lines to the measurements (Eq. 7-1) has to be extended to the following equation describing the scattering process [198]:

$$k_{xm}'^2 = \left(\mathrm{m}\frac{2\pi}{\Lambda} - k_0 \sin\theta\cos\varphi\right)^2 + (k_0 \sin\theta\cos\varphi)^2 \quad , m \in \mathbb{Z} \qquad \text{(Eq. 7-3)}$$

Changing φ after the Bragg lines were fitted with this equation to Figure 7-7, it reveals that the grating must have been rotated to φ = 85° in the measurement for Figure 7-8. The deviation of 5° is attributed to the manual positioning of the stamp on the substrate during the NIL step.

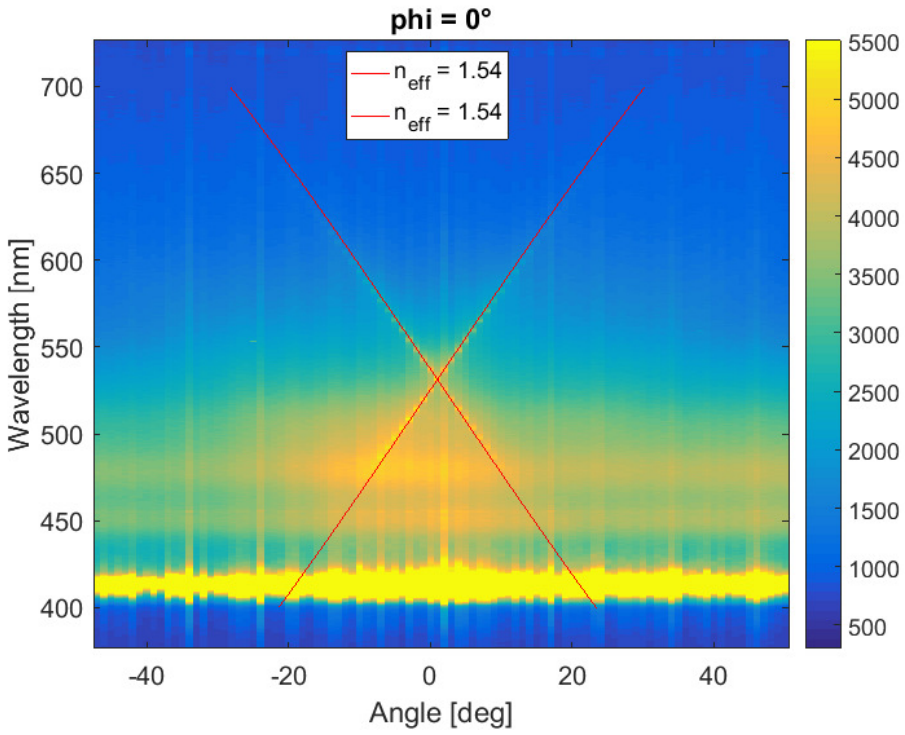

Figure 7-7: PL measurement of a SiO/Alq_3/SiO/Ag stack on grating with Λ = 370 nm with fitted Bragg lines.

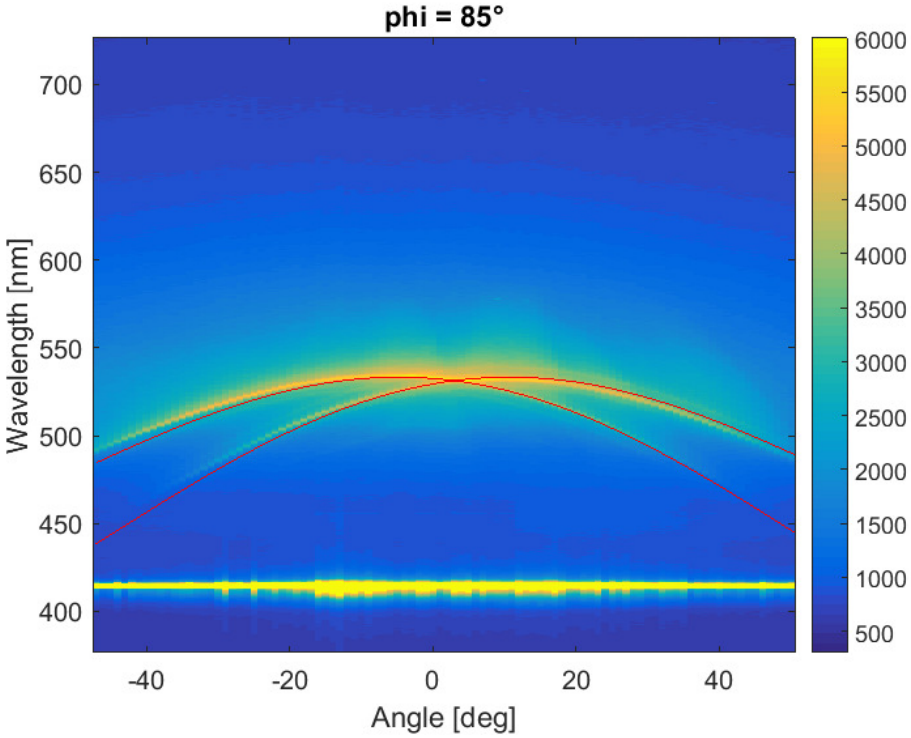

Figure 7-8: PL measurement of a SiO/Alq_3/SiO/Ag stack on grating with Λ = 370 nm with fitted Bragg lines after φ rotation.

An experimental approach on influencing grating resonance intensities in OLEDs

This part provides an overview of the most important parameters that are influencing the intensity of resonances caused by integrated gratings in OLEDs. Here, mainly layer position, thickness, absorption and refractive index are included.

Also dipole orientations [105] and grating depths have an influence on the resonance intensity, where the last one induces an intensity shift to longer wavelengths with an increasing depth as was shown experimentally [199]. These parameters are difficult to control and for this reasons not examined experimentally in the described studies.

Effect of emitter positioning

The following experiments show the influence of the emitter and metal electrodes positions systematically. In order to simplify the fabrication and characterization processes only photoluminescence (PL) measurements were performed. This had also the advantage that the organic semiconductors for the charge transportation could be exchanged with silicon monoxide (SiO). Thereby, the negative effect on the resonance intensity caused by their absorption could be avoided. The samples for this experiment were fabricated by NIL if they contained a grating and thermal evaporation was used for the remaining layers. For the characterization, goniometric measurements were made and due to their amount, all of them can be found in Appendix B .

A problem was the encapsulation of the samples, which was still needed to perform the measurements in the photogoniometer. The usually employed epoxy adhesive turned out to luminesce when exposed to UV light with peaks at 450 nm and 480 nm, which can be seen in Figure 7-7. In Figure 7-8 it is not visible because the excitation of the epoxy is enhanced when $\varphi = 0°$. For this reason, the encapsulation was changed to spincoated PMMA later. This encapsulation is much thinner and weaker but still better than exposing the samples directly to air.

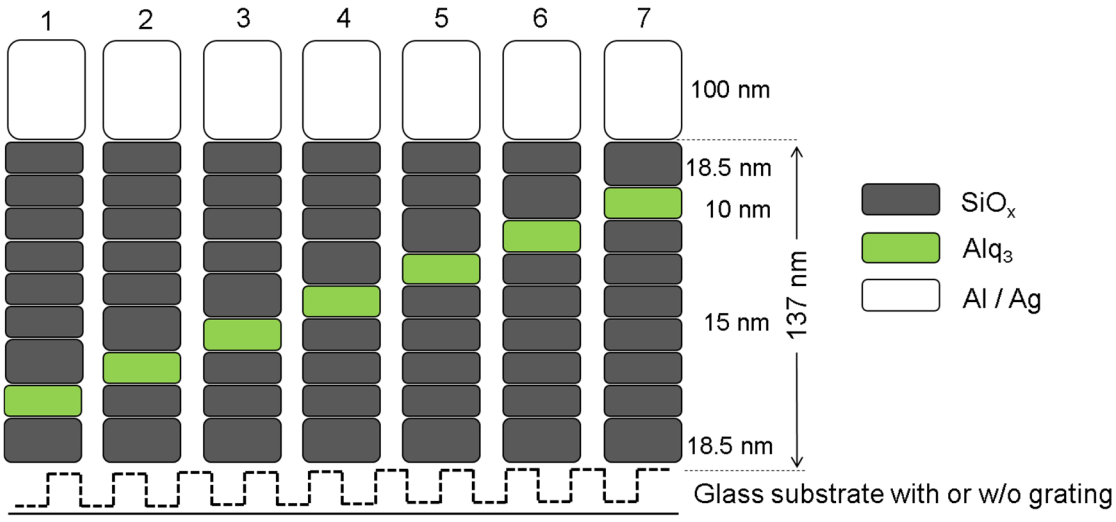

Figure 7-9: Schematic of stacks on samples with varying emitter position (drawn by Markus Köpke).

In a first step, the position of the emissive layer was varied according to the schematic in Figure 7-9 without changing the height of the complete stack, using silver or aluminum as top electrode. All variations were produced in form of stripes on one 25 mm x 25 mm glass substrate. As well known, the position of the emitter influences the light output of an OLED in general, which could be due to a higher amount of SPPs close to a metal electrode or to self-amplification caused by interferences (see Chapter 2). The sample without a grating produced a minimum for stack 2/3 and a maximum for stack 6 (Appendix B 1, 5). The resonance intensity was reduced compared to the Alq_3 background spectrum when the emitter was moved away from the grating. This is clearly visible for both electrode types (Appendix B 2, 6) and even after rotation of the samples (Appendix B 4, 7). For the sample with the silver electrode it became more clear after the luminescence of the epoxy had been reduced (Appendix B 3). The quality factor was also decreasing, which is defined as:

$$\boldsymbol{Q = \frac{\lambda}{FWHM}} \qquad \text{(Eq. 7-4)}$$

where FWHM stands for full width at half maximum starting from Alq_3 background. The reducing quality factor can already be seen from the example spectra in Figure

7-10. The next diagram in Figure 7-11 states that the reduction of the quality factor is linear, dependent on the displacement of the emitter position.

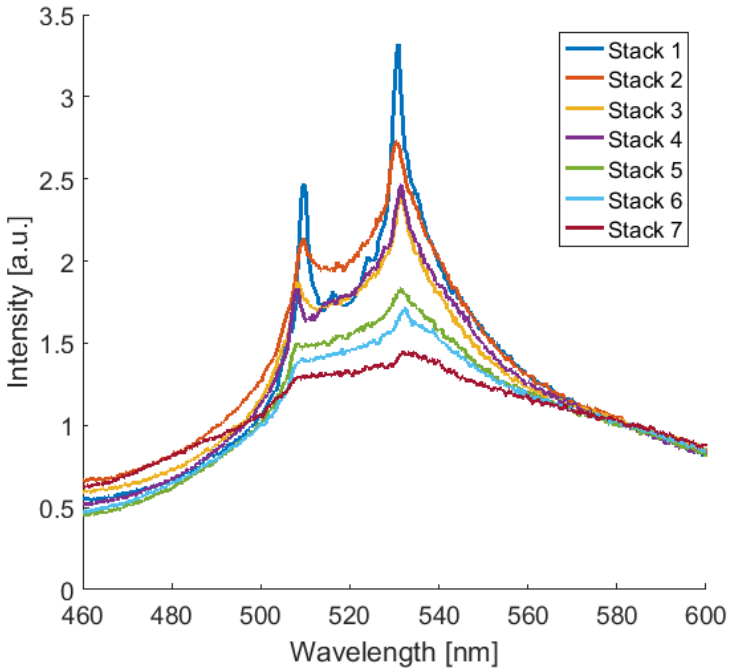

Figure 7-10: Photoluminescence spectra of stacks 1 to 7 of the sample with varying emitter position, grating (350 nm) and silver electrode at θ = -20°, φ = 90°, normalized to λ = 580 nm; Emitter distance to grating increasing and to electrode decreasing.

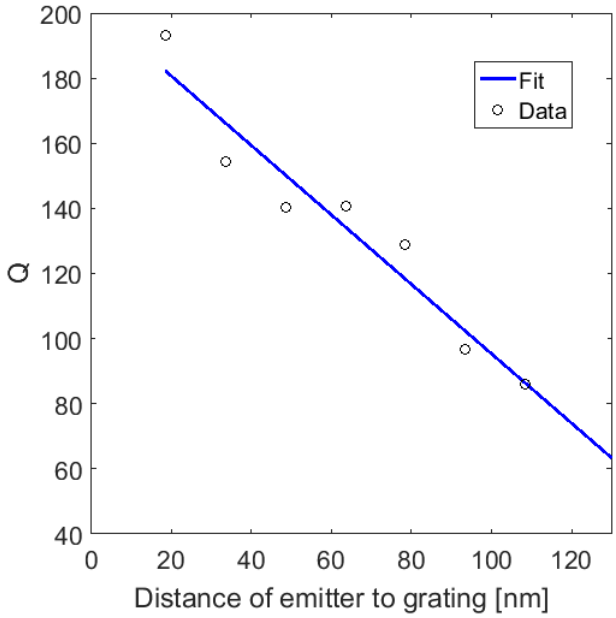

Figure 7-11: Quality factors depending on emitter distance to grating / electrode (at 137 nm away from grating) for spectra shown in Figure 7-10 with regression line.

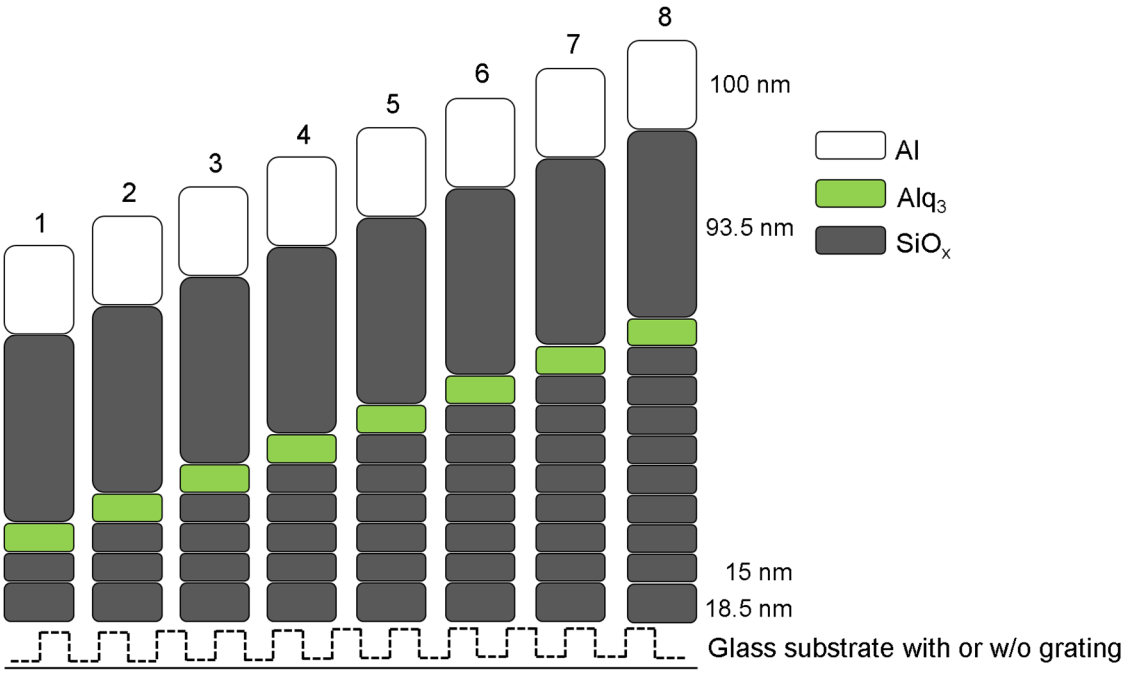

Figure 7-12: Schematic of stacks on samples with different distances to the substrate or grating (drawn by Markus Köpke).

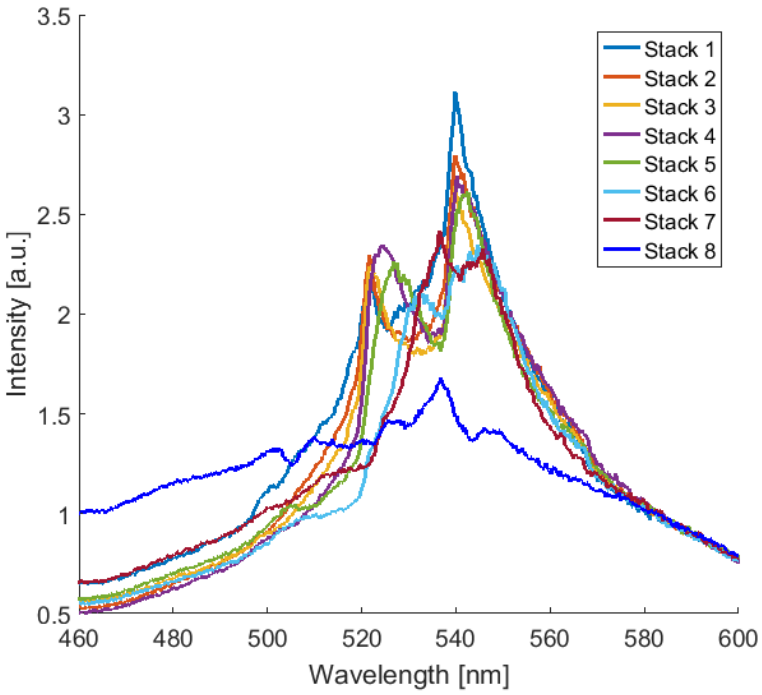

Figure 7-13: Photoluminescence spectra of stack 1 to 8 of sample with varying emitter distance to grating (350 nm) and aluminum electrode at θ = -10°, φ = 90°, normalized to λ = 580 nm.

To check whether the distance to the grating or the distance to the electrode was the critical factor for the described resonance intensity reduction in the experiment, in a next run only the distance to the grating was changed (Figure 7-12). The stacks without a grating (Appendix B 8) revealed—despite the strong emitting epoxy—that emission spectrum and intensity were not changed intensively by this modulation. The resonance position of the grating was slightly red-shifted due to the enlarging layer thickness (Appendix B 9). It turned out that the distance to the grating is less critical as the variation of the resonances is comparably low (Appendix B 9, 10). This can be seen again in Figure 7-13. A stronger reduction could first be obtained from stack 6 but in stack 8, the reduction of the quality factor was intensive. These results were expected because as long as the fill factor of the outcoupled mode with the grating is not changing substantially, the resonance intensity should not change dramatically either.

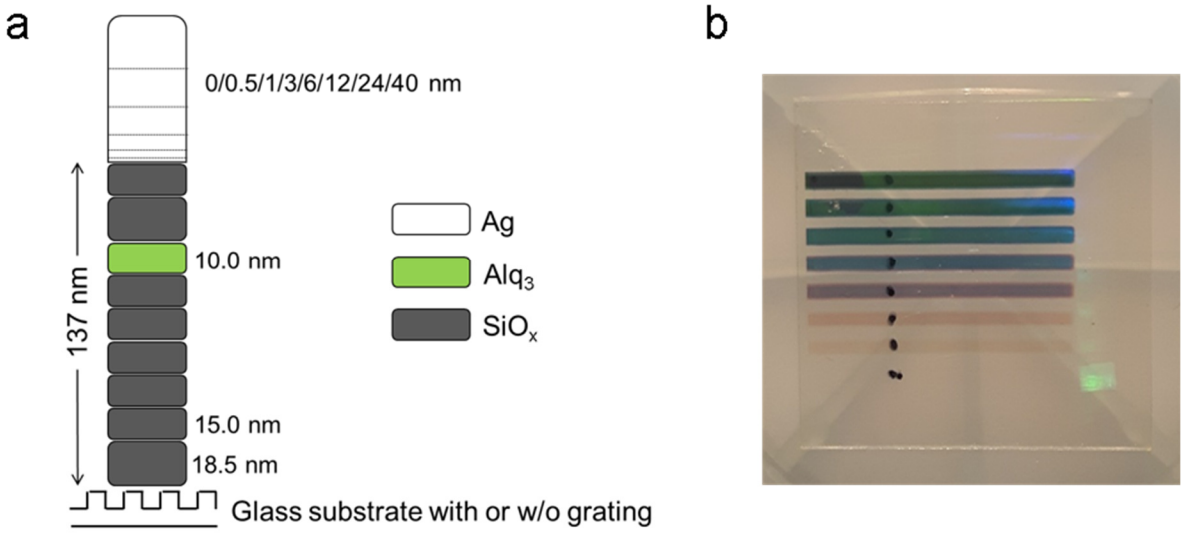

Figure 7-14: (a) Schematic (drawn by Markus Köpke) and (b) photo of a sample with different silver layer thicknesses on simplified OLED stack.

Next, the influence of the metal electrode was investigated more closely by changing its thickness. The emitter was placed quite close to the metal for this experiment (Figure 7-14a). Thin metal electrodes become transparent and can also change their color as can be seen in Figure 7-14b. In case of two transparent electrodes, light is emitted in two directions (top and bottom) from an OLED. The sample without

grating (Appendix B 11) shows that once the metal layer gets more and more reflecting, the measured light output at the detection side (bottom) increases. The growing reflection already prohibits a "disappearing" of light to the wrong side. Once there is a grating in this stack (Appendix B 12), the influence on the resonances is different at the beginning: While on the first stack the resonances are visible, they are disappearing and then becoming more intensive for thicker metal layers (Figure 7-15). At the beginning, only the absorption increases and the metal starts first to reflect with thicker layers which then help to enhance the resonance effect. This was also shown in a simulation by Hannes Lüder, which revealed that a metal layer made of silver has to be at least 80 nm thick to achieve the optimal results. The reason for this is that the TE modes are able to run partly in a thin metal layer while this is not possible in thicker metal layers and the mode is pushed a bit away from the metal layer when it is getting thicker [199].

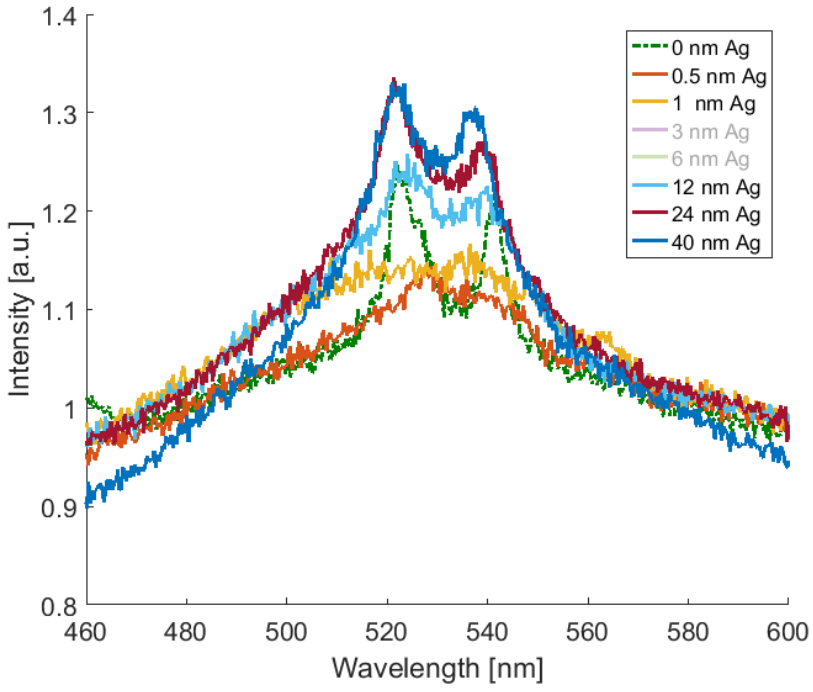

Figure 7-15: Photoluminescence spectra of stack 1 to 8 of the sample with varying silver electrode thickness (grating period 350 nm) θ = -10°, φ = 90°, normalized to λ = 580 nm; the stacks with 3 nm and 6 nm Ag were removed for overview reasons and as they were quite similar to the stack with 1 nm Ag.

To summarize the results of the PL experiments shortly: In case the resonances produced by a grating in an OLED shall be maximized, the emissive layer has to be put away from a metal electrode and if this is not possible, it has to be at least a completely non-transparent metal layer. The distance to the grating becomes only critical for larger values. Absorption has always to be kept as low as possible in the stack.

Adjusting resonance intensities with nanoparticle blends

Like the emitter position and the absorption, the refractive index has a big influence on the resonances in the emission spectrum of an OLED with integrated gratings. A high fill factor of the guided mode with the grating as well as a large refractive index contrast are both important for high resonance peaks. Using a standard material as ITO for the anode on top of a grating fabricated in Amonil would be already sufficient as the refractive index of ITO is quite high ($n_{\mathrm{ITO}} \approx 1.9$ at 530 nm) compared to glass. Even most of the organic semiconductors possess a higher refractive index. PRADANA [200], [201] wanted to use a highly conductive PEDOT:PSS for an anode to obtain a bendable OLED on polycarbonate. The refractive index of PEDOT:PSS is the same as for glass and the photo resist. This would have made the grating invisible for the light if the PEDOT:PSS would have been spincoated on top. PRADANA decided to mix titanium dioxide nanoparticles (TiO_2 NP) with an average diameter of 35 nm into the resist. He showed that up to 30 vol% of the TiO_2 NP can be mixed into it and thereby refractive index changes from ≈1.5 to ≈1.85 (at 530 nm) were possible. At the same time, it was proven that no scattering is caused by the particles [201].

The TiO_2 NP were dispersed in xylene. The quality of the dispersion is a crucial point for this application. If the nanoparticles were partly accumulating to larger particles, large scattering effects would appear.

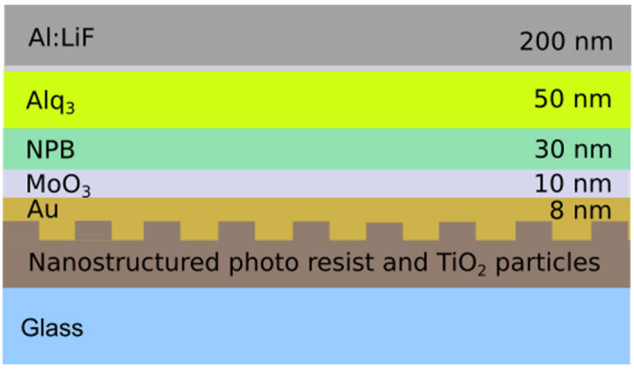

Figure 7-16: Schematic of OLED stack on nanostructured photo resist.

The same method was applied here to tailor the intensity of the resonance peaks without touching the OLED stack. Therefore, different amounts of TiO_2 NP were mixed into Amonil which resulted in hybrid resist layers with different thicknesses (10 vol% TiO_2 NP → d = 305 nm, 20 vol% TiO_2 NP → d = 405 nm, 30 vol% TiO_2 NP → d = 505 nm) [201]. After the grating was imprinted into the resist, the OLED stack shown in Figure 7-16 was built on top.

In Figure 7-17 the angular-resolved EL and PL spectra of the OLEDs are given. It can be seen clearly that the resonances are disappearing with an increasing NP content. This is due to the fact that the refractive index of the resist increases and becomes equal to the refractive index of the organic stack.

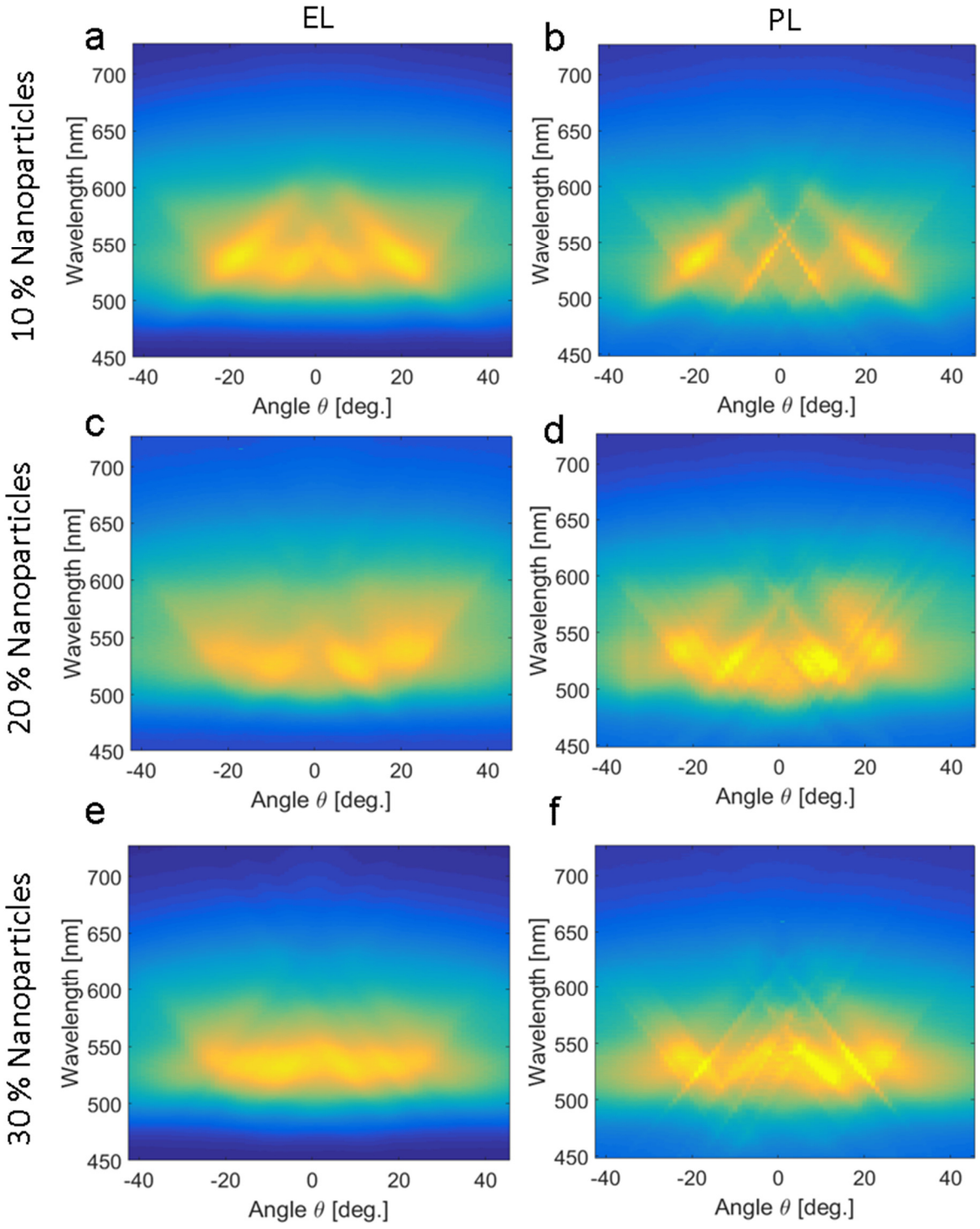

Figure 7-17: EL and PL spectra of OLEDs with linear grating (period 370 nm) and variation of TiO_2 nanoparticle content in photo resist.

Photonic crystals for fully flexible OLEDs

The last part already mentioned the work of Arfat Pradana who used nanoparticles in a photoresist in order to realize a refractive index contrast at the boundary to a PEDOT:PSS anode [200], [201]. The anode was made of PEDOT:PSS because it had to be flexible. As substrate, Arfat Pradana used a polycarbonate sheet, which was still quite stiff and could only be bended a bit. In Chapter 2, a photochromic layer on a fully flexible (bendable and stretchable) PDMS substrate was shown and this encouraged to also develop an OLED on PDMS with an integrated grating. The use of a rigid photoresist or a metal oxide layer is inapplicable for this purpose, and for this reason the grating structure was molded into the PDMS that afterwards is used as substrate (Figure 7-18a).

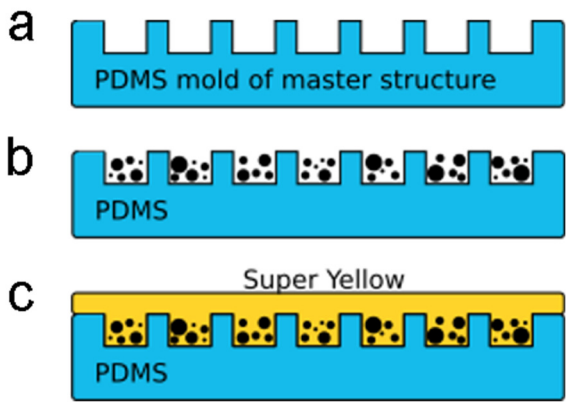

Figure 7-18: Fabrication procedure of simplified OLED stack on flexible PC for PL measurements: a) molding of master structure, b) spincoating of nanoparticles, c) OLED stack on top (drawn by Julius Schmalz).

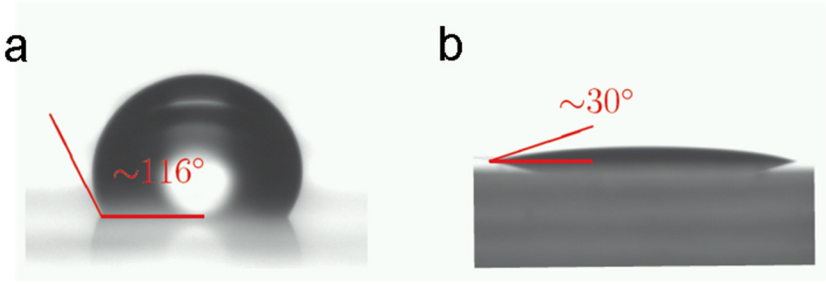

Figure 7-19: Contact angles of a) hydrophobic PDMS and b) hydrophilic PEO-PDMS (made by Julius Schmalz).

A problem is the high hydrophobicity of the PDMS, which results in a low adhesion of materials on it, especially for the hydrophilic conductive PEDOT:PSS that could be a potential anode material. A treatment of the PDMS surface with an oxygen plasma would help to overcome this problem but also destroys the grating structure completely, even with a very low power. In addition, it produces a thin glass layer on top of the PDMS that could cause surface cracks during stretching. Another method to get a more hydrophilic PDMS is to mix it with poly(dimethylsiloxane)-b-poly(ethylenoxide) (PDMS-PEO) [202]. There one methyl group of the PDMS is substituted with a strong polar poly(ethylenoxide). Thereby the PDMS gets much more hydrophilic as the contact angle measurements in Figure 7-19 are showing, but it also gets softer and a bit hazy. Mixing 2 % of the PDMS-PEO under the normal PDMS already gives a contact angle of 30° for the final PEO-PDMS. The rest of the structure molding and PEO-PDMS curing is comparable to the process that was described in the part about NIL—except from a lower curing temperature of 70 °C. This prolonged the curing time to four hours.

Now a sufficiently large refractive index contrast ($n_{\mathrm{PDMS}} = 1.42$) was needed to produce a photonic crystal and make the grating resonances visible in the OLED emission spectrum. Here, spherical ZnO nanoparticles dispersed in H_2O (Sigma Aldrich) were employed for this. First, the dispersion was diluted from 30 % down to 4% to 16 % and then mixed with 0.5 % of a fluorosurfactant (FC-4430 by 3M Germany GmbH) to enhance the surface adhesion. This mixture was then spincoated with 2000 rpm onto the PEO-PDMS (Figure 7-18). In principle it would also be possible to mix metal oxide nanoparticles directly into PEDOT:PSS and use it as an anode, but if the dispersed ZnO particles are mixed into PEDOT:PSS they are forming agglomerations again—probably caused by the PSS. Mixing particles directly from a powder into the PEDOT:PSS requires a suitable dispersion method, which was proven to be difficult by the usage of TiO_2 NP powder. The SEM images in Figure 7-20 illustrate the result of using a bad dispersion with TiO_2 NP powder in PEDOT:PSS (a) and a good nanoparticle dispersion with ZnO partiles in H_2O (b).

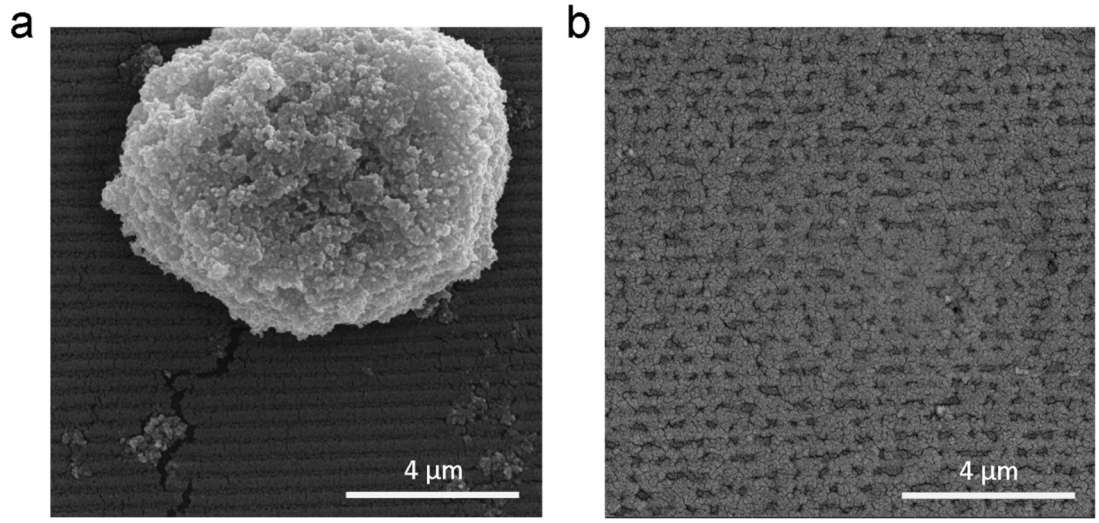

Figure 7-20: SEM images of structured PEO-PDMS after spincoating (a) PEDOT:PSS containing non-perfectly dispersed TiO_2 nanoparticles (NP) from a powder and (b) ZnO NP spincoated direcly (made by Julius Schmalz / Torben Karrock).

To further check the quality of the produced photonic crystals, their resonances were checked by putting them between crossed polarizers as shown in Figure 7-21. Photos taken of the samples under the microscope are already an evidence for their different resonances according to the ZnO content of the spincoated mixture (Figure 7-22). Figure 7-23 depicts the spectra of their resonance in transmission. As can be seen from this figure the highest quality factor is achieved with a ZnO content of 12 % in H_2O. 16 % ZnO is already producing a spectrum outside the interesting range. The shown examples have been fabricated on a thin PDMS layer ($d \approx 150$ µm). Thicker layers produce an additional polarization rotation, which would increase the background light in the spectrum and distort the measurement.

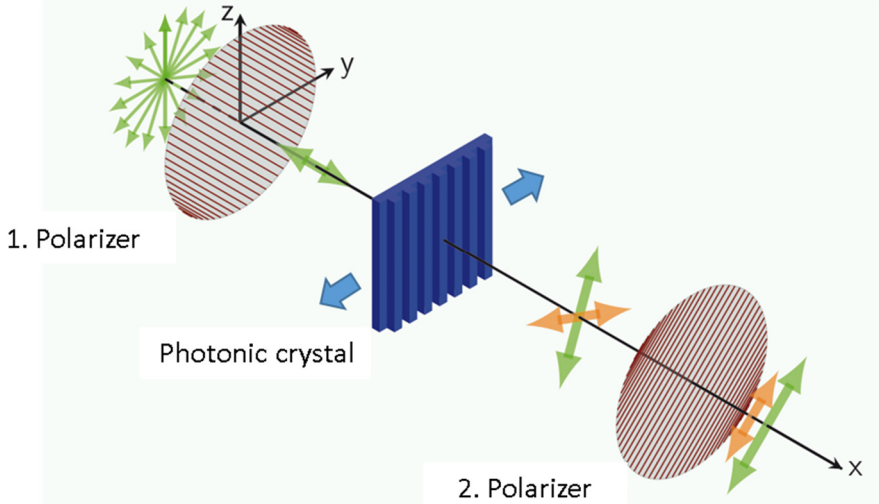

Figure 7-21: Schematic of the measurement setup for the determination of the resonance spectrum of a (flexible) photonic crystal (drawn by Julius Schmalz).

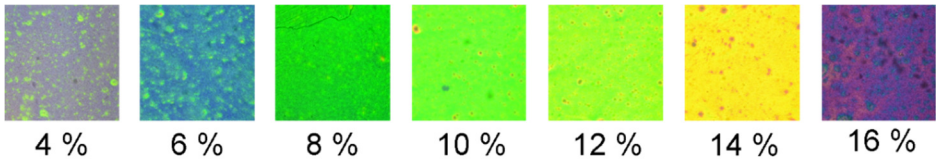

Figure 7-22: Photos of a photonic crystal (Λ = 400 nm) fabricated with different ZnO particle concentrations in spincoating solution (under a microscope between crossed polarizers).

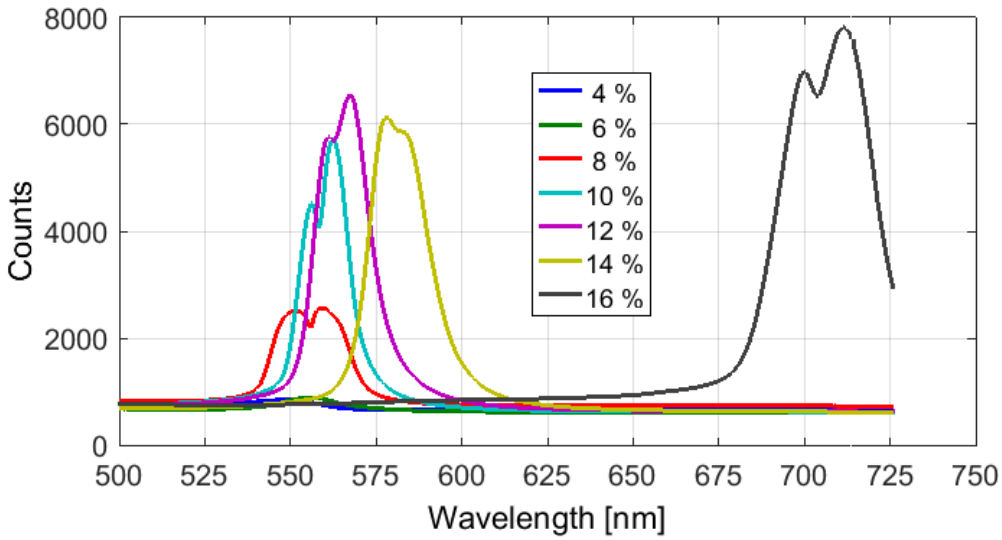

Figure 7-23: Resonance spectra of PCs (Λ = 400 nm) fabricated with different ZnO particle concentrations in spincoating solution (made by Julius Schmalz).

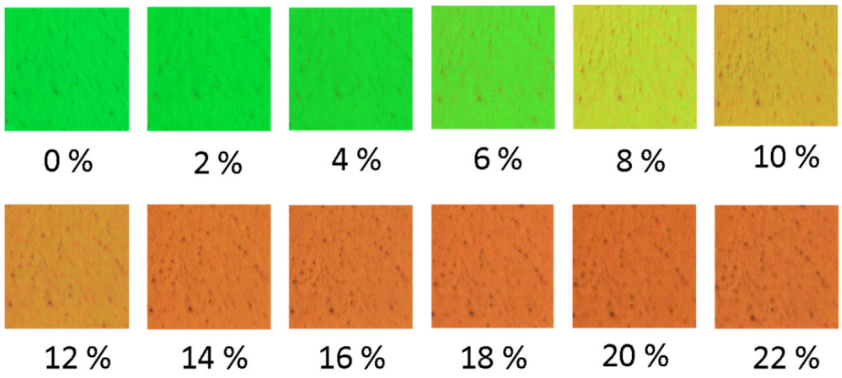

Figure 7-24: Photos of photonic crystal (Λ = 400 nm) with different prolongations (under a microscope between crossed polarizers).

Now, a sample with 12 % ZnO was stretched between the crossed polarizers and thereby a redshift of its the resonance spectrum was obtained as can be seen in the photos in Figure 7-24. The quality factor of the resonance improves with the first prolongation and decreases continuously afterwards (Figure 7-25). The redshift due to the prolongation is about 3.4 nm/% .

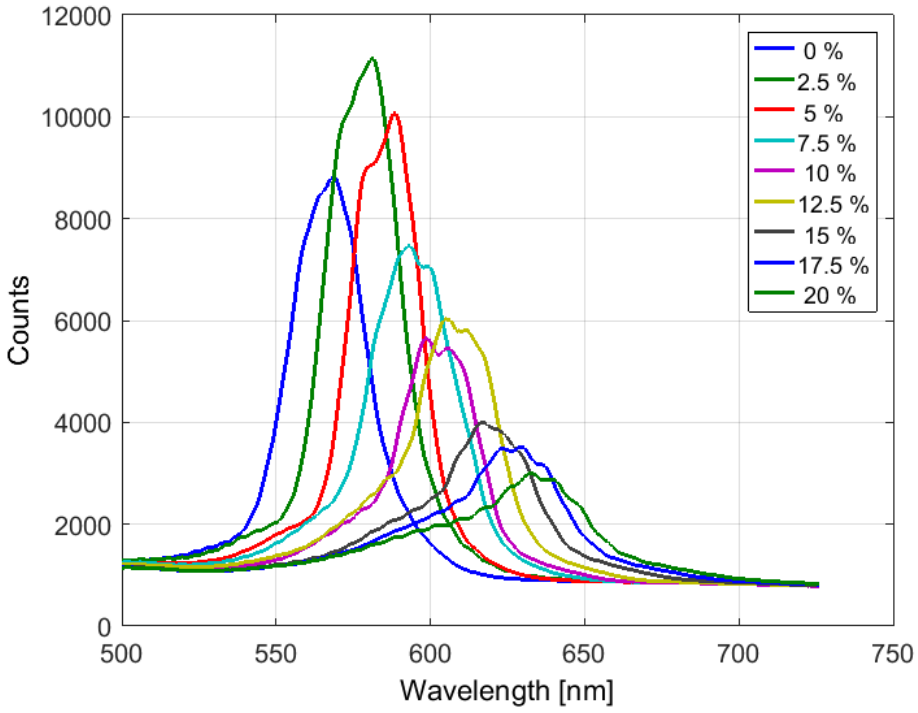

Figure 7-25: Resonance spectra (Λ = 400 nm) of PC with different prolongations (made by Julius Schmalz).

To understand the reducing quality factor of the photonic crystal resonance better, finite-difference time-domain (FDTD) simulations in 3D were performed. The used program was FDTD Solutions by Lumerical. The simulated grating had a periodicity Λ = 400 nm with a structure height h = 120 nm, and the ZnO particles ($n_{\mathrm{ZnO}} = 2.1$) had a diameter of 40 nm. The results plotted on the next page are not showing resonances of the simulated photonic crystals (with crossed polarizers) but their transmission spectra. The position of the highest absorption corresponds almost to their resonance position. Also, all their other properties are linked and therefore the FDTD results can be directly compared to the measured resonances.

In case the particle density would stay constant during the prolongation of the photonic crystal, its central resonance wavelength would simply shift with an increasing quality factor (Figure 7-26). At higher wavelength, the mode is less guided in the waveguide of the photonics crystal. As follows, the mode overlap with the grating is lower and it is less scattered by the grating, which causes the higher quality factor. If the number of nanoparticles stays constant (Figure 7-27), the quality factor increases as well. Consindering now that there are more nanoparticles in the grooves of the structure, the quality factor still increases (Figure 7-28).

Compared to the experiments, there is a strong broadening of the resonance that causes a decrease of the quality factor (Figure 7-25). The increasing quality factor with low stretching can be explained with the effect seen in the FDTD simulations. With a higher prolongation there might be unconformable periodicity changes over the sample caused by the sample mounting at the edges. The strain is a bit larger in the center of the sample and in addition to that, the distribution of the particles is probably not ideal over the whole sample under strain. Another very likely reason might be the emergence of cracks in the nanoparticle layer.

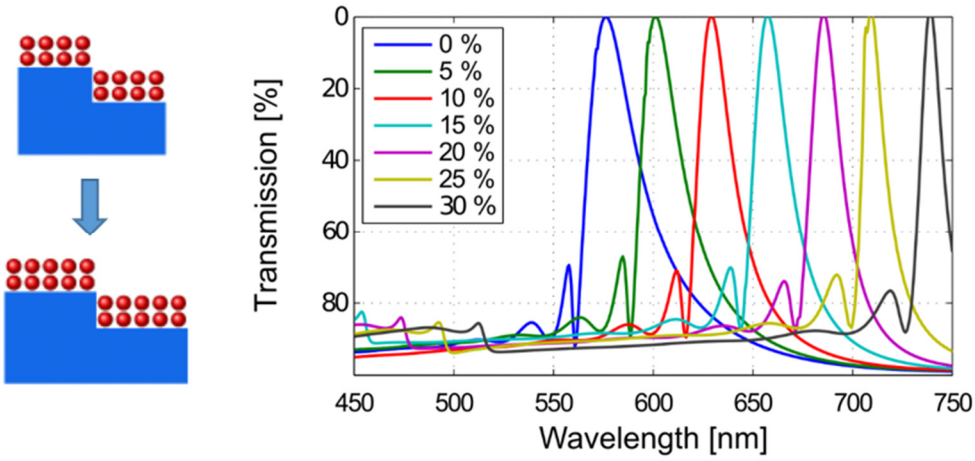

Figure 7-26: Simulated resonance spectra of a PC with constant NP density under prolongation (made by Julius Schmalz).

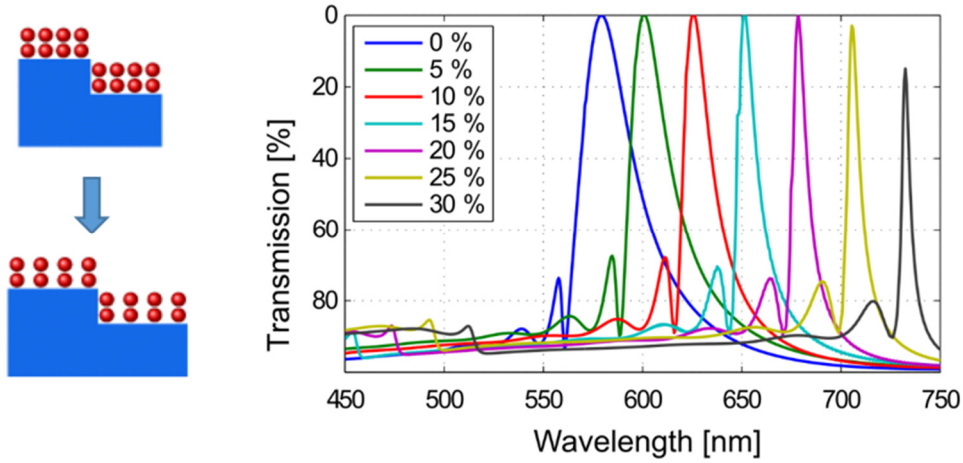

Figure 7-27: Simulated resonance spectra of a PC with constant number of NPs under prolongation (made by Julius Schmalz).

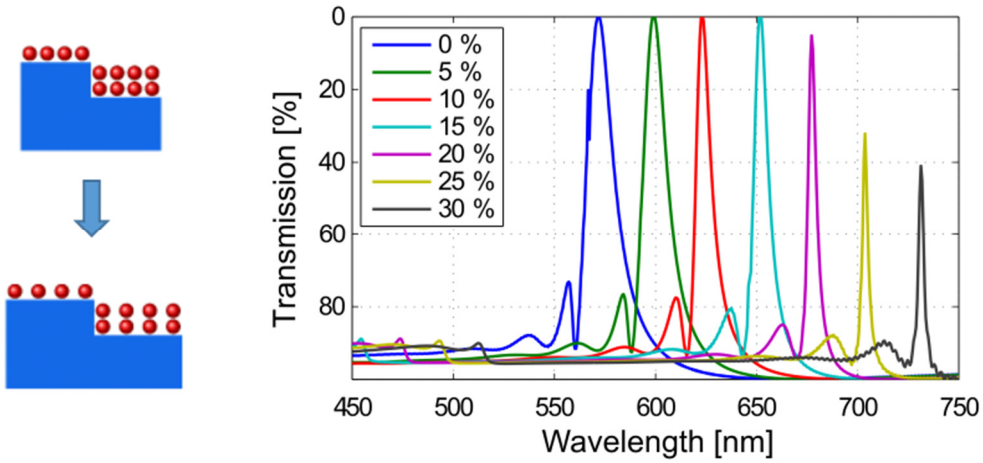

Figure 7-28: Simulated resonance spectra of a PC with constant number of NPs and more particles in the grooves under prolongation (made by Julius Schmalz).

Finally, an emissive polymer, Super Yellow (Merck), was spincoated on top of the flexible photonic crystal (Figure 7-18c). This allowed to perform PL measurements, which are shown in Figure 7-29. As can be seen, there are more resonances than one expects from a single grating, but this was caused by the relatively thick guiding layer, which supported multiple modes. It thereby comes to TE or TM modes of higher order, and the reason for the close superposition around the central resonance is an inhomogeneity of the high-index layer. Comparing the position of the central resonance at θ = 0° for no (λ_{CR0} = 625 nm) and 10 % stretching states a displacement of the resonance of about $\Delta\lambda$ = 30 nm. From theory, the displacement of the resonance by a prolongation p of the grating (Λ = 400 nm) is defined as:

$$\boldsymbol{\Delta\lambda = p \cdot \Lambda \cdot n_{eff}} \qquad \text{(Eq. 7-5)}$$

For a stretching of p = 10 % with $n_{\text{eff}} = \frac{\lambda_{CR0}}{\Lambda} = 1.56$, this equation predicts a resonance displacement of approximately $\Delta\lambda$ = 62.5 nm (under the assumption that n_{eff} = const.). It follows, that there is a deviation from theory to experiment with a factor of two. Already the characterization of the photonic crystals (Figure 7-25) gave comparable results, but the theory as well as the FDTD simulation require that the refractive indices and the layer thicknesses are not changing during stretching. Since it is difficult to predict if and how these two parameters are affected, it is not possible to include this into the theory.

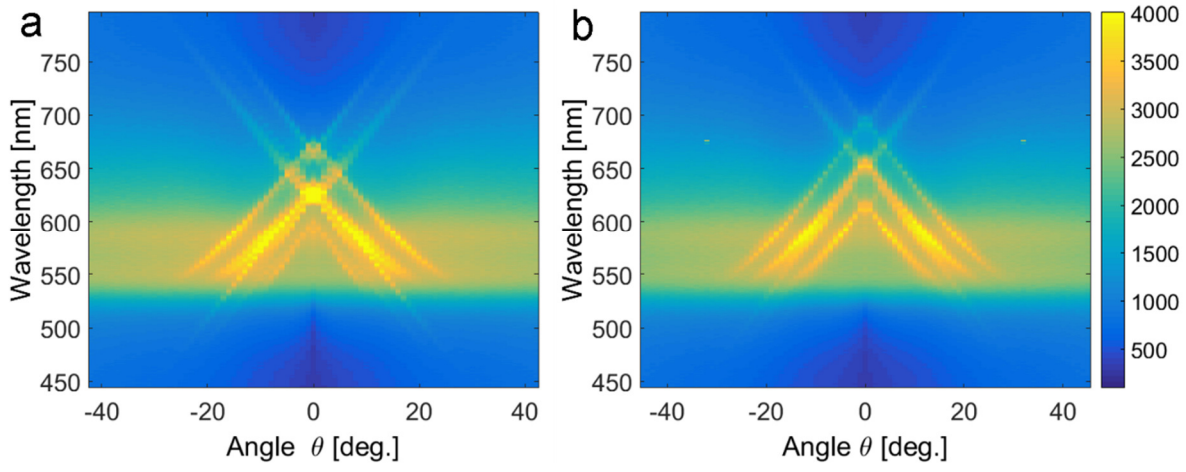

Figure 7-29: Angle-resolved photoemission spectra of simple OLED stack (a) unstretched and (b) with 10 % stretching (made by Julius Schmalz).

It was also tried to build a complete OLED on top of the presented flexible photonic crystal, but EL measurements have not been possible so far because of a low conductivity of the used electrodes. Aluminum became completely black when evaporated onto PEO-PDMS. Silver performed much better but had still a low conductivity and was difficult to contact on the soft substrate. Another problem was encapsulation of the samples. It was possible to pour PEO-PDMS partly on top, but the PDMS was still not an effective barrier towards air and humidity. Thus, there is still a lot of work to pursue before EL is possible.

Multi-periodic gratings for OLEDs

The equation (Eq. 7-2) is also valid for multi-periodic gratings. Those are just superpositions of multiple mono-periodic gratings as shown schematically in Figure 7-30. The period of the multi-periodic grating Λ_{MP} will be larger than of a mono-periodic grating as it is the least common multiple of the combined single gratings, e. g. $\Lambda_1(250\ \mathrm{nm}) + \Lambda_2\ (300\ \mathrm{nm}) + \Lambda_3\ (450\ \mathrm{nm}) = \Lambda_{\mathrm{MP}}(4500\ \mathrm{nm})$. These gratings are directing light into multiple directions as provided by its single gratings and this has already been shown by Christian Kluge in PL measurements [203].

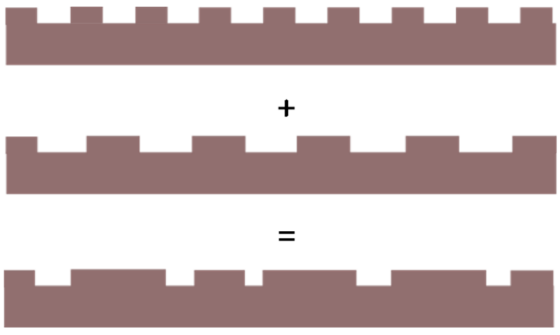

Figure 7-30: Multi-periodic gratings are superpositions of mono-periodic gratings.

Figure 7-31: Sample pattern of multi-periodic grating: 250 nm/300 nm/450 nm (duty cycles: 0.3/0.5/0.3); showing $2\Lambda_{MP}$.

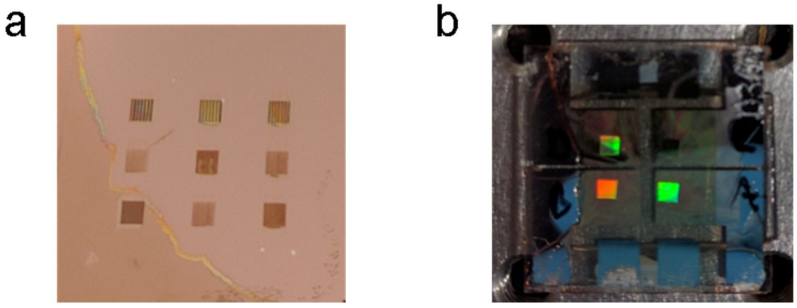

Figure 7-32: (a) Master with 9 gratings (each 2 mm x 2 mm) fabricated by KNMF, Karlsruhe; (b) Gratings integrated into OLEDs on glass substrate with visible grating effects by reflection (made by Mesut-Ömür Özden).

The difficult task that arises from the superposition of the gratings is to fabricate the small features of these structures, because they can be much smaller than in a typical optical grating with dimensions beneath 50 nm. For this, very sophisticated e-beam lithography is needed. With the Karlsruhe Nano and Micro Facility (KNMF) a partner could be found who was able to fabricate these structures, but due to the intensive time-consuming nature of the process, the dimensions of the written structures were kept at just 2 mm x 2 mm (Figure 7-32a). The gratings were transferred by NIL onto a glass substrate and then an OLED was fabricated on top of them (Figure 7-32b). Therefore, the emitting area of the OLED was isolated to the structured areas on the substrate by using another lithography step and the photoresist AZ1518 by Microchemicals. The applied OLED stack is depicted in the schematic in Figure 7-33. It is similar to the one used for the experiments with nanoparticle blends in the OLED stack in this chapter.

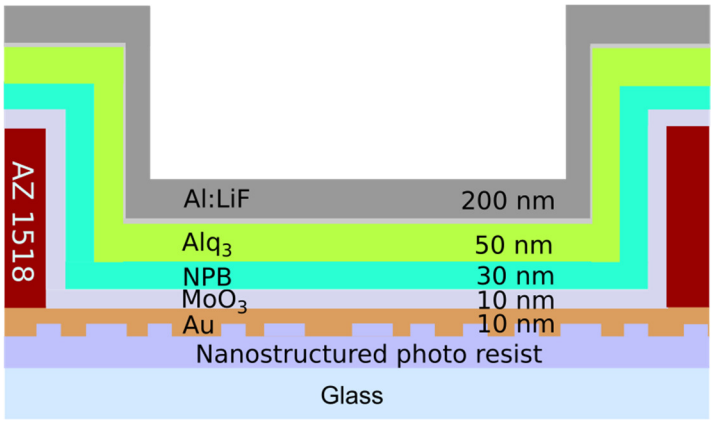

Figure 7-33: Schematic of OLED stack built on multi-periodic nanostructure with isolating photoresist layer (AZ1518, d = 2 µm).

The size of the OLED was very small, which also meant that the amount of light that could be analyzed in measurements was low. The integrating time for the goniometric measurements had to be set to the maximum of spectrometer capabilities (10 s) in EL, and in only few attempts it was possible to see resonances. An example is given in Figure 7-34 with PL in (a) and EL in (b) for the structure shown in Figure 7-31.

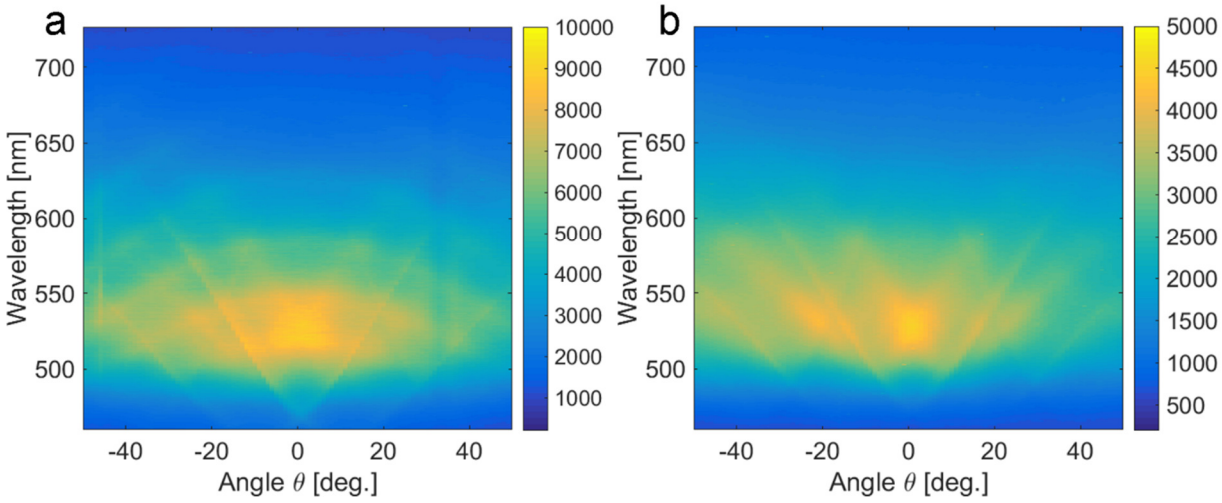

Figure 7-34: (a) PL and (b) EL of the structure shown in Figure 7-31 (made by Mesut-Ömür Özden).

The low number of useful results at the current state is attributed to a low quality of the master structure and the small quantity of available light due to the highly absorbing gold anode (Figure 6-4). Furthermore, the simple OLED structure must be mentioned, as well as the quality of the lithography step for the isolation of the

emitting area, because of the usage of foils as exposure masks that contained tiny bubbles. The usage of ITO and professional chromium masks for the isolation step should bring some enhancement, but it would still be better to use larger patterned master structures, which are hard to manufacture.

Discussion

Due to the distinct nature of the experiments described here, this is more a summary of this chapter. Further discussions can be found at the end of each part.

The results of the systematic experiments speak for themselves. They revealed the main issues with the adjustment of the resonance intensities. Critical were a low refractive index contrast, the closeness to a metal layer and especially the absorption of thin metal layers.

In the next part, it was shown how the resonance of an OLED emission spectrum shifts, when it is built on a fully flexible substrate, which possesses a grating and is stretched. Unfortunately, the shift of the resonance by the characterized photonic crystals was not in agreement with the performed FDTD simulations, which could be due to a change of the refractive index, a thinning of the NP or Super Yellow layer or a combination of both. Additionally, the decreasing quality factor could not be seen in the simulation, which strengthens the speculation that cracks might occur in the nanoparticle layer. Measuring the effect in electroluminescence and a fabrication of OLEDs directly on the back of the functionalized lotus PDMS from Chapter 3 will need some more sophisticated engineering on the electrodes and the encapsulation of the flexible devices. Still, the results are promising, not only for flexible sensors and integrated systems with OLEDs, but also as a utility in upcoming flexible OLED displays for warning purposes when the devices are bended or stretched too intensively. The warning would be obtained in form of a perceived color change in the display.

Finally, it was shown that OLED light could also be directed into multiple directions with superimposed gratings. This has already been already predicted in photoluminescence measurements a few years ago [203], but was now proven in electroluminescence as well. The stack fabricated on top of the OLED could still have some optimizations aiming to see the resonances more clearly and thereby to make the direction of light more efficient. For the use of these multi-periodic structures in a higher volume, it would need a faster and more reliable method to produce the master structures as well.

The findings of this chapter will help to enhance the directing of light in certain directions, which then could increase the switching of photochromic layers fabricated on the reverse side of the same substrate. As already mentioned in the introduction this would be of substantial importance for the device integration. For the excitation of photochromic molecule new (multi-periodic) gratings will have to be designed, which will allow to direct the OLED light straight to the switchable surface as it is depicted in Figure 1-1.

Chapter 8.

Summary and conclusion

In this thesis the development of photo-switchable surfaces and their combination with blue OLEDs was shown. Starting from the initial aim to switch the contact angle of water droplets on a surface by light, a biomimetic approach was investigated: A lotus leave structure was copied into PDMS, which was covalently functionalized with an azobenzene molecule by the help of "click chemistry". Unfortunately, no switching of the contact angle was observed on these surfaces, but as they were transparent the switching of the relative transmission (355 nm) was instead enhanced by a factor of 200 compared to flat glass substrate that was functionalized the same way. This surface property allowed for making surface maps, which were showing switched and not switched areas. They were produced by scanning a UV laser over the surface and measuring absorption differences. For the development of programmable surfaces it is important to be able to perform this type of measurement. In addition, it allows checking the influence of the surface structure onto the switching behavior of the photochromic molecule.

Next, candle soot surfaces were non-covalently functionalized with spiropyran and these surfaces allowed a reversible switching of the contact angle between 138° and 95°. Drawbacks were their poor homogeneity and their high absorption. Transferring this functionalization to both silica-based candle soot and an artificial sharkskin foil, which are more transparent, did not succeed. Still, it was surprising that the simple drop casting method with a toluene-acetone mixture produced surfaces with contact angle switching capability that was comparable or even better than on surfaces with covalently bound spiropyran [142], [204]–[207].

It was a blue OLED based on the emitter BCzVBi developed that delivered a radiant flux of up to over 10 mW/cm². This OLED was able to switch azobenzene molecules in a PMMA matrix from *cis* to *trans* state, as well as the azobenzene-functionalized lotus PDMS to 80 % (with 4 mW/cm²) within four minutes. In addition, a faster switching of droplet contact angles (compared to darkness) of the spiropyran-coated candle soot could be shown. On the other hand, the radiant flux provided by a high-power LED is still higher and able to switch photochromic layers faster. To further increase the output power of OLEDs, t-ZnO particles incorporated in PTU were investigated as OLED substrates. The t-ZnO particles scatter light, promising enhanced outcoupling of trapped substrate modes. Devices with a low t-ZnO content in their substrate showed a 30 % increase of their radiant flux, but at the same time, they did not get more efficient. This negative effect might have been caused by a higher current injection in the end due to the high surface roughness that additionally made the use of a PEDOT:PSS layer for planarization necessary. This layer made the devices more efficient, but resulted in a lower light output because it is absorbing light.

Another approach to optimize the switching by OLEDs is to concentrate their emitted light in a certain direction, which can be achieved by an integration of optical gratings into an OLED stack [29]. It was shown how the position of the emitting layer effects the intensity of resonances produced by a grating. There, a position close to a metallic electrode proved to be mostly reducing the resonance intensity, which was even worse in front of thin metal electrodes that were partly transparent.

As a photochromic layer was fabricated on PDMS, also the effect of a grating in an OLED put on top of this very flexible material was shown in photoluminescence measurement. A side product was a highly flexible photonic crystal, which showed a large resonance shift under stretching.

Finally, a multi-periodic grating was introduced into an OLED stack, which scattered light concentrated into multiple directions. This was the first time that this effect was shown in a goniometric electroluminescence measurement.

Showing the localized enhancement of switching a photochromic layer by OLEDs with gratings as schematically depicted in Figure 1-1 was not successful so far. A strong reduction of the scattering would be needed for this. Additionally, gratings will have to be designed in a next step such that they are able to direct as much light as possible to the surface normal of the emitting OLED area. A combination of this with a substrate outcoupling by nanoparticles would not make sense, as the scattering particles would destroy the light-concentration effect by the gratings.

To conclude, switching of photochromic layers by OLEDs is already possible. Overall, a combination with the functionalized lotus PDMS is already close to an application in an integrated device as due to the transparent PDMS, the OLED could be fabricated on its back. Other photochromic molecules could be used to control, e. g., protein adsorption, cell adhesion or DNA attachment [7], [48]. Then the adsorption of the biomaterial would just have to induce a signal to be read out. Due to the enlarged surface by the lotus leaf structure, the chance is high to create an increased signal. The result would be a spatially controllable biosensor.

The development of more photo-switchable surfaces with other properties while still leaving them transparent is still a challenging task. This is especially the case for the contact angle switching. Spiropyran might be more promising for this application as it provides a larger shift of its dipole moment, but so far the best results have been shown with azobenzene [123], [134]. On the other hand, these surfaces have been highly absorbing light.

Finally, it would of course be very practical to have a stable OLED that is able to emit UV light. It would be needed for a completely integrated device, which can switch a photochromic layer reversibly. An alternative would be to synthetically modify the photochromic molecules such that their bands are red-shifted [46], but as it was already shown for azobenzene the stability of the *cis* state is reduced intensively by this modification [48].

Nevertheless, this work provides a bundle of design criteria, processes and more results, which will help to develop spatially controllable integrated devices.

Bibliography

[1] Y. Liu, L. Mu, B. Liu, and J. Kong, "Controlled switchable surface," *Chem. - A Eur. J.*, vol. 11, no. 9, pp. 2622–2631, 2005.

[2] S. L. Gras, T. Mahmud, G. Rosengarten, A. Mitchell, and K. Kalantar-Zadeh, "Intelligent control of surface hydrophobicity," *ChemPhysChem*, vol. 8, no. 14, pp. 2036–2050, 2007.

[3] R. H. El Halabieh, O. Mermut, and C. J. Barrett, "Using light to control physical properties of polymers and surfaces with azobenzene chromophores," *Pure Appl. Chem.*, vol. 76, no. 7–8, pp. 1445–1465, 2004.

[4] N. Nishikawa, H. Kiyohara, S. Sakiyama, S. Yamazoe, H. Mayama, T. Tsujioka, Y. Kojima, S. Yokojima, S. Nakamura, and K. Uchida, "Photoinduced formation of superhydrophobic surface on which contact angle of a water droplet exceeds 170 by reversible topographical changes on a diarylethene microcrystalline surface," *Langmuir*, vol. 28, no. 51, pp. 17817–17824, 2012.

[5] R. Klajn, "Spiropyran-based dynamic materials.," *Chem. Soc. Rev.*, vol. 43, no. 1, pp. 148–84, 2014.

[6] R. Klajn, "Immobilized azobenzenes for the construction of photoresponsive materials," *Pure Appl. Chem.*, vol. 82, no. 12, pp. 2247–2279, 2010.

[7] G. Wang and J. Zhang, "Photoresponsive molecular switches for biotechnology," *J. Photochem. Photobiol. C Photochem. Rev.*, vol. 13, no. 4, pp. 299–309, 2012.

[8] D. Baigl, "Photo-actuation of liquids for light-driven microfluidics: state of the art and perspectives," *Lab Chip*, vol. 12, no. 19, p. 3637, 2012.

[9] M. Freebody, "OLEDs set to reshape market," *Photonics Spectra*, pp. 26–31, 2016.

[10] S. Reineke, F. Lindner, G. Schwartz, N. Seidler, K. Walzer, B. Lüssem, and K. Leo, "White organic light-emitting diodes with fluorescent tube efficiency.," *Nature*, vol. 459, no. 7244, pp. 234–8, 2009.

[11] J. Liang, L. Li, X. Niu, Z. Yu, and Q. Pei, "Elastomeric polymer light-emitting devices and displays," *Nat. Photonics*, vol. 7, no. 10, pp. 817–824, 2013.

[12] M. S. White, M. Kaltenbrunner, E. D. Głowacki, K. Gutnichenko, G. Kettlgruber, I. Graz, S. Aazou, C. Ulbricht, D. a. M. Egbe, M. C. Miron, Z. Major, M. C. Scharber, T. Sekitani, T. Someya, S. Bauer, and N. S. Sariciftci, "Ultrathin, highly flexible and stretchable PLEDs," *Nat. Photonics*, vol. 7, no. 10, pp. 811–816, 2013.

[13] V. Bulović, G. Gu, P. E. Burrows, S. R. Forrest, and M. E. Thompson, "Transparent light-emitting devices," *Nature*, vol. 380, p. 29, 1996.

[14] P. Görrn, M. Sander, J. Meyer, M. Kroger, E. Becker, H. H. Johannes, W. Kowalsky, and T. Riedl, "Towards see-through displays: Fully transparent thin-film transistors driving transparent organic light-emitting diodes," *Adv. Mater.*, vol. 18, no. 6, pp. 738–741, 2006.

[15] E. Orgiu and P. Samorì, "25th anniversary article: Organic electronics marries photochromism: Generation of multifunctional interfaces, materials, and devices," *Adv. Mater.*, vol. 26, no. 12, pp. 1827–1844, 2014.

[16] E. Orgiu, N. Crivillers, M. Herder, L. Grubert, M. Pätzel, J. Frisch, E. Pavlica, D. T. Duong, G. Bratina, A. Salleo, N. Koch, S. Hecht, and P. Samorì, "Optically switchable transistor via energy-level phototuning in a bicomponent organic semiconductor," *Nat. Chem.*, vol. 4, no. 8, pp. 675–679, 2012.

[17] N. Crivillers, E. Orgiu, F. Reinders, M. Mayor, and P. Samorì, "Optical modulation of the charge injection in an organic field-effect transistor based on photochromic self-assembled-monolayer-functionalized electrodes," *Adv. Mater.*, vol. 23, no. 12, pp. 1447–1452, 2011.

[18] B. Xin and J. Hao, "Reversibly switchable wettability," *Chem. Soc. Rev.*, vol. 39, no. 2, pp. 769–782, 2010.

[19] S. Wang, Y. Song, and L. Jiang, "Photoresponsive surfaces with controllable wettability," *J. Photochem. Photobiol. C Photochem. Rev.*, vol. 8, no. 1, pp. 18–29, 2007.

[20] N. Verplanck, Y. Coffinier, V. Thomy, and R. Boukherroub, "Wettability

switching techniques on superhydrophobic surfaces," *Nanoscale Res. Lett.*, vol. 2, no. 12, pp. 577–596, 2007.

[21] X. Deng, L. Mammen, H.-J. Butt, and D. Vollmer, "Candle Soot as a Template for a Transparent Robust Superamphiphobic Coating," *Science*, vol. 335, no. 6064, pp. 67–70, 2012.

[22] T. Sun, L. Feng, X. Gao, and L. Jiang, "Bioinspired surfaces with special wettability," *Acc. Chem. Res.*, vol. 38, no. 8, pp. 644–652, 2005.

[23] B. Bhushan and Y. C. Jung, "Natural and biomimetic artificial surfaces for superhydrophobicity, self-cleaning, low adhesion, and drag reduction," *Prog. Mater. Sci.*, vol. 56, no. 1, pp. 1–108, 2011.

[24] T. Yu, W. Su, W. Li, R. Hua, B. Chu, and B. Li, "Ultraviolet electroluminescence from organic light-emitting diode with cerium(III)-crown ether complex," *Solid. State. Electron.*, vol. 51, no. 6, pp. 894–899, 2007.

[25] H. Etori, X. L. Jin, T. Yasuda, S. Mataka, and T. Tsutsui, "Spirobifluorene derivatives for ultraviolet organic light-emitting diodes," *Synth. Met.*, vol. 156, no. 16–17, pp. 1090–1096, 2006.

[26] W. Brütting, J. Frischeisen, T. D. Schmidt, B. J. Scholz, and C. Mayr, "Device efficiency of organic light-emitting diodes: Progress by improved light outcoupling," *Phys. status solidi*, vol. 210, no. 1, pp. 44–65, Jan. 2013.

[27] H. W. Chang, J. Lee, S. Hofmann, Y. Hyun Kim, L. Müller-Meskamp, B. Lüssem, C. C. Wu, K. Leo, and M. C. Gather, "Nano-particle based scattering layers for optical efficiency enhancement of organic light-emitting diodes and organic solar cells," *J. Appl. Phys.*, vol. 113, no. 20, 2013.

[28] L. Li, J. Liang, S.-Y. Chou, X. Zhu, X. Niu, ZhibinYu, and Q. Pei, "A solution processed flexible nanocomposite electrode with efficient light extraction for organic light emitting diodes.," *Sci. Rep.*, vol. 4, p. 4307, 2014.

[29] U. Geyer, J. Hauss, B. Riedel, S. Gleiss, U. Lemmer, and M. Gerken, "Large-scale patterning of indium tin oxide electrodes for guided mode extraction from organic light-emitting diodes," *J. Appl. Phys.*, vol. 104, no. 9, 2008.

[30] E. V. Anslyn and D. A. Dougherty, *Modern Physical Organic Chemistry*. Sausalito, CA: University Science Books, 2006.

[31] B. H. Brand, "Theorie der Farbigkeit." [Online]. Available: www.bhbrand.de/downloads/1farbigkeit.pdf. [Accessed: 01-Aug-2017].

[32] M. Schwoerer and H. C. Wolf, *Organische Molekulare Festkörper*. Weinheim, Germany: Wiley-VCH, 2005.

[33] A. Köhler and H. Bässler, *Electronic processes in organic semiconductors*. Weinheim, Germany: Wiley-VCH, 2015.

[34] M. C. Petty, *Molecular Electronics*. Chichester: John Wiley & Sons Ltd., 2007.

[35] Y. Hirshberg, "Photochromy in the bianthrone series," *Comptes Rendu l'Académie des Sci.*, vol. 231, pp. 903–904, 1950.

[36] H. Dürr, "Organische Photochromie," *Angew. Chemie*, vol. 116, no. 25, pp. 3404–3418, 2004.

[37] M. M. Russew and S. Hecht, "Photoswitches: From molecules to materials," *Adv. Mater.*, vol. 22, no. 31, pp. 3348–3360, 2010.

[38] K. Nakatani, J. Piard, and R. Métivier, "Introduction: Organic Photochromic Molecules," in *Photochromic Materials: Preparation, Properties and Applications*, First Edit., H. Tian and J. Zhang, Eds. Wiley-VCH, 2016.

[39] E. Mitscherlich, "Über die Zusammensetzung des Nitrobenzids und Sulfobenzids," *Ann. Pharm.*, vol. 12, pp. 305–311, 1834.

[40] Demselben, "Über das Stickstoffbenzid," *Ann. Pharm.*, vol. 12, pp. 311–314, 1834.

[41] G. S. HARTLEY, "The Cis-form of Azobenzene," *Nature*, vol. 140, no. 3537. pp. 281–281, 1937.

[42] H. M. D. Bandara and S. C. Burdette, "Photoisomerization in different classes of azobenzene," *Chem. Soc. Rev.*, vol. 41, no. 5, p. 1809, 2012.

[43] C. R. Crecca and A. E. Roitberg, "Theoretical study of the isomerization mechanism of azobenzene and disubstituted azobenzene derivatives," *J. Phys. Chem. A*, vol. 110, no. 26, pp. 8188–8203, 2006.

[44] I. K. Lednev, T. Q. Ye, R. E. Hester, and J. N. Moore, "Femtosecond time-resolved

UV-visible absorption spectroscopy of trans-azobenzene in solution," *J. Phys. Chem.*, vol. 100, no. 96, pp. 13338–13341, 1996.

[45] C. Pakula, C. Hanisch, V. Zaporojtchenko, T. Strunskus, C. Bornholdt, D. Zargarani, R. Herges, and F. Faupel, "Optical switching behavior of azobenzene/PMMA blends with high chromophore concentration," *J. Mater. Sci.*, vol. 46, no. 8, pp. 2488–2494, 2011.

[46] A. a. Beharry, O. Sadovski, and G. A. Woolley, "Azobenzene photoswitching without ultraviolet light," *J. Am. Chem. Soc.*, vol. 133, no. 49, pp. 19684–19687, 2011.

[47] S. Samanta, A. a. Beharry, O. Sadovski, T. M. McCormick, A. Babalhavaeji, V. Tropepe, and G. A. Woolley, "Photoswitching Azo compounds in vivo with red light," *J. Am. Chem. Soc.*, vol. 135, no. 26, pp. 9777–9784, 2013.

[48] A. a Beharry and G. A. Woolley, "Azobenzene photoswitches for biomolecules.," *Chem. Soc. Rev.*, vol. 40, no. 8, pp. 4422–4437, 2011.

[49] J. Piard, "Influence of the solvent on the thermal back reaction of one spiropyran," *J. Chem. Educ.*, vol. 91, no. 12, pp. 2105–2111, 2014.

[50] W. Putzbach and N. J. Ronkainen, "Immobilization techniques in the fabrication of nanomaterial-based electrochemical biosensors: a review.," *Sensors (Basel).*, vol. 13, no. 4, pp. 4811–4840, 2013.

[51] R. Wang, T. Iyoda, L. Jiang, D. a. Tryk, K. Hashimoto, and A. Fujishima, "Structural investigation of azobenzene-containing self-assembled monolayer films," *J. Electroanal. Chem.*, vol. 438, no. 1–2, pp. 213–219, 1997.

[52] E. Benassi and S. Corni, "Quenching of the Photoisomerization of Azobenzene Self-Assembled Monolayers by the Metal Substrate," *J. Phys. Chem. C*, vol. 118, no. 45, pp. 25906–25917, 2014.

[53] N. R. Krekiehn, M. Müller, U. Jung, S. Ulrich, R. Herges, and O. M. Magnussen, "UV/Vis Spectroscopy Studies of the Photoisomerization Kinetics in Self-Assembled Azobenzene-Containing Adlayers," *Langmuir*, vol. 31, no. 30, pp. 8362–8370, 2015.

[54] C. Dorrer and J. Rühe, "Some thoughts on superhydrophobic wetting," *Soft Matter*, vol. 5, no. 1, p. 51, 2009.

[55] A. Nakajima, "Design of hydrophobic surfaces for liquid droplet control," *NPG Asia Mater.*, vol. 3, no. 5, pp. 49–56, 2011.

[56] T. Nishino, M. Meguro, K. Nakamae, M. Matsushita, and Y. Ueda, "The lowest surface free energy based on -CF3 alignment," *Langmuir*, vol. 15, no. 13, pp. 4321–4323, 1999.

[57] J. Zhang, X. Lu, W. Huang, and Y. Han, "Reversible superhydrophobicity to superhydrophilicity transition by extending and unloading an elastic polyamide film," *Macromol. Rapid Commun.*, vol. 26, no. 6, pp. 477–480, 2005.

[58] S. G. Lee, D. Y. Lee, H. S. Lim, D. H. Lee, S. Lee, and K. Cho, "Switchable transparency and wetting of elastomeric smart windows," *Adv. Mater.*, vol. 22, no. 44, pp. 5013–5017, 2010.

[59] R. N. Wenzel, "Resistance of solid surfaces to wetting by water.," *J. Ind. Eng. Chem. (Washington, D. C.)*, vol. 28, pp. 988–994, 1936.

[60] A. B. D. Cassie and S. Baxter, "Wettability of porous surfaces," *Trans. Faraday Soc.*, vol. 40, no. 5, pp. 546–551, 1944.

[61] A. Lafuma and D. Quéré, "Superhydrophobic states.," *Nat. Mater.*, vol. 2, no. 7, pp. 457–460, 2003.

[62] X. Feng and L. Jiang, "Design and creation of superwetting/antiwetting surfaces," *Adv. Mater.*, vol. 18, no. 23, pp. 3063–3078, 2006.

[63] N. J. Shirtcliffe, G. McHale, S. Atherton, and M. I. Newton, "An introduction to superhydrophobicity," *Adv. Colloid Interface Sci.*, vol. 161, no. 1–2, pp. 124–138, 2010.

[64] B. Wang, Y. Zhang, L. Shi, J. Li, and Z. Guo, "Advances in the theory of superhydrophobic surfaces," *J. Mater. Chem.*, vol. 22, no. 38, p. 20112, 2012.

[65] M. Nosonovsky and B. Bhushan, "Patterned Nonadhesive surfaces: Superhydrophobicity and wetting regime transitions," *Langmuir*, vol. 24, no. 4, pp. 1525–1533, 2008.

[66] D. C. Pease, "The Significance of the Contact Angle in Relation to the Solid Surface," *J. Phys. Chem.*, vol. 49, no. 2, pp. 107–110, 1945.

[67] E. Cpc and C. P. Company, "Contact Angles and Hysteresis on Surfaces with Chemically Heterogeneous Islands," no. October, pp. 3793–3796, 2015.

[68] F. E. Bartell and J. W. Shepard, "Surface Roughness as Related to Hysteresis of Contact Angles. II. The Systems Paraffin-3 Molar Calcium Chloride Solution-Air and Paraffin-Glycerol-Air," *J. Phys. Chem.*, vol. 57, no. 2, pp. 455–458, 1953.

[69] L. Gao and T. J. McCarthy, "How Wenzel and Cassie were wrong," *Langmuir*, vol. 23, no. 7, pp. 3762–3765, 2007.

[70] G. McHale, "Cassie and Wenzel: Were they really so wrong?," *Langmuir*, vol. 23, no. 15, pp. 8200–8205, 2007.

[71] L. Gao and T. J. McCarthy, "An attempt to correct the faulty intuition perpetuated by the wenzel and cassie 'laws,'" *Langmuir*, vol. 25, no. 13, pp. 7249–7255, 2009.

[72] L. Gao, A. Y. Fadeev, and T. J. Mccarthy, "S uperhydrophobicity and Contact-Line Issues," *Mater. Res. Soc. Bull.*, vol. 33, no. August, pp. 747–751, 2008.

[73] Y. Kwon, S. Choi, N. Anantharaju, J. Lee, M. V. Panchagnula, and N. A. Patankar, "Is the Cassie-Baxter formula relevant?," *Langmuir*, vol. 26, no. 22, pp. 17528–17531, 2010.

[74] A. J. B. Milne and A. Amirfazli, "The Cassie equation: How it is meant to be used," *Adv. Colloid Interface Sci.*, vol. 170, no. 1–2, pp. 48–55, 2012.

[75] D. Quéré, "Non-sticking drops," *Reports Prog. Phys.*, vol. 68, no. 11, pp. 2495–2532, 2005.

[76] M. Nosonovsky, "Multiscale roughness and stability of superhydrophobic biomimetic interfaces," *Langmuir*, vol. 23, no. 6, pp. 3157–3161, 2007.

[77] N. J. Shirtcliffe, G. McHale, M. I. Newton, G. Chabrol, and C. C. Perry, "Dual-scale roughness produces unusually water-repellent surfaces," *Adv. Mater.*, vol. 16, no. 21, pp. 1929–1932, 2004.

[78] Y. Y. Yan, N. Gao, and W. Barthlott, "Mimicking natural superhydrophobic

surfaces and grasping the wetting process: A review on recent progress in preparing superhydrophobic surfaces," *Adv. Colloid Interface Sci.*, vol. 169, no. 2, pp. 80–105, 2011.

[79] H. J. Ensikat, P. Ditsche-Kuru, C. Neinhuis, and W. Barthlott, "Superhydrophobicity in perfection: The outstanding properties of the lotus leaf," *Beilstein J. Nanotechnol.*, vol. 2, no. 1, pp. 152–161, 2011.

[80] C. Journet, S. Moulinet, C. Ybert, S. T. Purcell, and L. Bocquet, "Contact angle measurements on superhydrophobic Carbon Nanotube Forests®: effect of fluid pressure," *Europhys. Lett.*, vol. 71, pp. 104–109, 2005.

[81] L. Vogelaar, R. G. H. Lammertink, and P. M. Wessling, "Superhydrophobic surfaces having easily adjustable two-fold roughness prepared in a single step .," *Lngmuir*, no. 22, pp. 3125–3130, 2006.

[82] J. P. Yang, Y. D. Jin, P. L. Heremans, R. Hoefnagels, P. Dieltiens, F. Blockhuys, H. J. Geise, M. Van der Auweraer, and G. Borghs, "White light emission from a single layer organic light emitting diode fabricated by spincoating," *Chem. Phys. Lett.*, vol. 325, no. 1–3, pp. 251–256, 2000.

[83] T. R. Hebner, T. R. Hebner, C. C. Wu, C. C. Wu, D. Marcy, D. Marcy, M. H. Lu, M. H. Lu, J. C. Sturm, and J. C. Sturm, "Ink-jet printing of doped polymers for organic light emitting devices," *Appl. Phys. Lett.*, vol. 72, no. 5, p. 519, 1998.

[84] A. Sandström, H. F. Dam, F. C. Krebs, and L. Edman, "Ambient fabrication of flexible and large-area organic light-emitting devices using slot-die coating," *Nat. Commun.*, vol. 3, p. 1002, 2012.

[85] A. Yassar, J. Roncali, and F. Garnier, "Conductivity and conjugation length in poly(3-methylthiophene) thin films," *Macromolecules*, vol. 22, no. 2, pp. 804–809, 1989.

[86] V. I. Arkhipov, E. V. Emelianova, Y. H. Tak, and H. Bässler, "Charge injection into light-emitting diodes: Theory and experiment," *J. Appl. Phys.*, vol. 84, no. 2, pp. 848–856, 1998.

[87] J. C. Scott and G. G. Malliaras, "Charge injection and recombination at the metal–

organic interface," *Chem. Phys. Lett.*, vol. 299, no. 2, pp. 115–119, 1999.

[88] H. Bässler, G. Schönherr, M. Abkowitz, and D. M. Pai, "Hopping transport in prototypical organic glasses," *Phys. Rev. B*, vol. 26, no. 6, pp. 3105–3113, Sep. 1982.

[89] C. Wang, H. Dong, W. Hu, Y. Liu, and D. Zhu, "Semiconducting π-conjugated systems in field-effect transistors: A material odyssey of organic electronics," *Chem. Rev.*, vol. 112, no. 4, pp. 2208–2267, 2012.

[90] N. Karl, "Charge carrier transport in organic semiconductors," *Synth. Met.*, vol. 133–134, pp. 649–657, 2003.

[91] K. Walzer, B. Maennig, M. Pfeiffer, and K. Leo, "on Electrically Doped Transport Layers Highly Efficient Organic Devices Based on Electrically Doped Transport Layers," *Cell*, vol. 107, no. 4, pp. 1233–1271, 2007.

[92] D. Hertel and H. Bässler, "Photophysics of luminescent conjugated polymers," in *Organic light-emitting devices*, K. Müllen and U. Scherf, Eds. Weinheim, Germany: Wiley-VCH, 2006.

[93] Q. Zhang, B. Li, S. Huang, H. Nomura, H. Tanaka, and C. Adachi, "Efficient blue organic light-emitting diodes employing thermally activated delayed fluorescence," *Nat. Photonics*, vol. 8, no. March, pp. 1–7, 2014.

[94] Y. E. Al Baldo, MA; O'Brien, DF; You, "Highly efficient phosphorescent emission from organic electroluminescent devices," *Nature*, vol. 395, no. 6698, pp. 151–154, 1998.

[95] M. A. Baldo, M. E. Thompson, and S. R. Forrest, "Phosphorescent materials for application to organic light emitting devices," *Pure Appl. Chem.*, vol. 71, no. 11, pp. 2095–2106, 1999.

[96] H. Yersin and W. J. Finkenzeller, *Triplet Emitters for Organic Light-Emitting Diodes: Basic Properties*. 2008.

[97] H. Uoyama, K. Goushi, K. Shizu, H. Nomura, and C. Adachi, "Highly efficient organic light-emitting diodes from delayed fluorescence.," *Nature*, vol. 492, no. 7428, pp. 234–8, 2012.

[98] J. Hauß, "Bragg-Gitter für das Lichtmanagement in organischen Leuchtdioden," Dissertation Karlsruher Institut für Technologie, 2014.

[99] G. E. Jabbour, B. Kippelen, N. R. Armstrong, and N. Peyghambarian, "Aluminum based cathode structure for enhanced electron injection in electroluminescent organic devices," *Appl. Phys. Lett.*, vol. 73, no. 9, pp. 1185–1187, 1998.

[100] S. Reineke, M. Thomschke, B. Lüssem, and K. Leo, "White organic light-emitting diodes: Status and perspective," *Rev. Mod. Phys.*, vol. 85, no. 3, pp. 1245–1293, 2013.

[101] J.-S. Kim, P. K. H. Ho, N. C. Greenham, and R. H. Friend, "Electroluminescence emission pattern of organic light-emitting diodes: Implications for device efficiency calculations," *J. Appl. Phys.*, vol. 88, no. 2, pp. 1073–1081, 2000.

[102] M. Ikai, S. Tokito, Y. Sakamoto, T. Suzuki, and Y. Taga, "Highly efficient phosphorescence from organic light-emitting devices with an exciton-block layer," *Appl. Phys. Lett.*, vol. 79, no. 2, pp. 156–158, 2001.

[103] S. R. Forrest, D. D. C. Bradley, and M. E. Thompson, "Measuring the efficiency of organic light-emitting devices," *Adv. Mater.*, vol. 15, no. 13, pp. 1043–1048, 2003.

[104] N. C. Greenham, R. H. Friend, and D. D. C. Bradley, "Angular Dependence of the Emission from a Conjugated Polymer Light-Emitting Diode: Implications for efficiency calculations," *Adv. Mater.*, vol. 6, no. 6, pp. 491–494, Jun. 1994.

[105] M. C. Gather and S. Reineke, "Recent advances in light outcoupling from white organic light-emitting diodes," *J. Photon. Energy*, vol. 5, no. 1, p. 57607, 2015.

[106] L. H. Smith, J. A. E. Wasey, I. D. W. Samuel, and W. L. Barnes, "Light out-coupling efficiencies of organic light-emitting diode structures and the effect of photoluminescence quantum yield," *Adv. Funct. Mater.*, vol. 15, no. 11, pp. 1839–1844, 2005.

[107] D. A. B. Miller, *Quantum Mechanics for Scientists and Engineers*. Cambrigde, 2008.

[108] M. Furno, R. Meerheim, S. Hofmann, B. Lüssem, and K. Leo, "Efficiency and rate

of spontaneous emission in organic electroluminescent devices," *Phys. Rev. B - Condens. Matter Mater. Phys.*, vol. 85, no. 11, pp. 1–21, 2012.

[109] B. Riedel, "Effizienzsteigerung in Organischen Leuchtdioden," Karlruher Institut für Technology, 2011.

[110] P. A. Hobson, J. A. E. Wasey, I. Sage, and W. L. Barnes, "The role of surface plasmons in organic light-emitting diodes," *Sel. Top. Quantum Electron. IEEE J.*, vol. 8, no. 2, pp. 378–386, 2002.

[111] H. Raether, *Surface Plasmons on Smooth and Rough Surfaces and on Gratings*, vol. 111. Berlin, Heidelberg: Springer Berlin Heidelberg, 1988.

[112] J. Lee, N. Chopra, and F. So, "Cavity effects on light extraction in organic light emitting devices," *Appl. Phys. Lett.*, vol. 92, no. 3, pp. 90–93, 2008.

[113] U. Lemmer, R. Hennig, W. Guss, A. Ochse, J. Pommerehne, R. Sander, A. Greiner, R. F. Mahrt, H. Baessler, J. Feldmann, and E. O. Goebel, "Microcavity effects in a spin-coated polymer two-layer system," *Appl. Phys. Lett.*, vol. 66, no. 11, pp. 1301–1303, 1995.

[114] N. Takada, T. Tsutsui, and S. Saito, "Control of emission characteristics in organic thin-film electroluminescent diodes using an optical-microcavity structure," *Appl. Phys. Lett.*, vol. 63, no. 15, pp. 2032–2034, 1993.

[115] V. Bulovic, V. B. Khalfin, G. Gu, P. E. Burrows, D. Z. Garbuzov, and S. Forrest, "Weak microcavity effects in organic light-emitting devices," *Phys. Rev. B. Condens. Matter*, vol. 58, no. 7, pp. 3730–3740, 1998.

[116] Q. Huang, K. Walzer, M. Pfeiffer, K. Leo, M. Hofmann, and T. Stübinger, "Performance improvement of top-emitting organic light-emitting diodes by an organic capping layer: An experimental study," *J. Appl. Phys.*, vol. 100, no. 6, 2006.

[117] M. Thomschke, R. Nitsche, M. Furno, and K. Leo, "Optimized efficiency and angular emission characteristics of white top-emitting organic electroluminescent diodes," *Appl. Phys. Lett.*, vol. 94, no. 8, pp. 1–4, 2009.

[118] G. Björk, S. MacHida, Y. Yamamoto, and K. Igeta, "Modification of spontaneous

emission rate in planar dielectric microcavity structures," *Phys. Rev. A*, vol. 44, no. 1, pp. 669–681, 1991.

[119] R. M. Amos and W. L. Barnes, "Modification of the spontaneous emission rate of Eu3+ ions close to a thin metal mirror," *Phys. Rev. B*, vol. 55, no. 11, pp. 7249–7254, 1997.

[120] W. L. Barnes, "Fluorescence near interfaces: the role of photonic mode density," *J. Mod. Opt.*, vol. 45, no. 4, pp. 661–699, 1998.

[121] R. Meerheim, M. Furno, S. Hofmann, B. Lüssem, and K. Leo, "Quantification of energy loss mechanisms in organic light-emitting diodes," *Appl. Phys. Lett.*, vol. 97, no. 25, pp. 24–27, 2010.

[122] L. M. Siewierski, W. J. Brittain, S. Petrash, and M. D. Foster, "Photoresponsive monolayers containing in-chain azobenzene," *Am. Chem. Soc. Polym. Prepr. Div. Polym. Chem.*, vol. 39, no. 2, pp. 264–265, 1996.

[123] H. S. Lim, J. T. Han, D. Kwak, M. Jin, and K. Cho, "Photoreversibly switchable superhydrophobic surface with erasable and rewritable pattern," *J. Am. Chem. Soc.*, vol. 128, no. 45, pp. 14458–14459, 2006.

[124] X. Pei, A. Fernandes, B. Mathy, X. Laloyaux, B. Nysten, O. Riant, and A. M. Jonas, "Correlation between the structure and wettability of photoswitchable hydrophilic azobenzene monolayers on silicon," *Langmuir*, vol. 27, no. 15, pp. 9403–9412, 2011.

[125] P. A. Lewis, R. K. Smith, K. F. Kelly, L. A. Bumm, S. M. Reed, R. S. Clegg, J. D. Gunderson, J. E. Hutchison, and P. S. Weiss, "The role of buried hydrogen bonds in self-assembled mixed composition thiols on Au{111}," *J. Phys. Chem. B*, vol. 105, no. 43, pp. 10630–10636, 2001.

[126] H. C. Kolb, M. G. Finn, K. B. Sharpless, and D. S. Kemp, "Click-Chemie®: diverse chemische Funktionalität mit einer Handvoll guter Reaktionen."

[127] T. Lummerstorfer and H. Hoffmann, "Click Chemistry on Surfaces: 1,3-Dipolar Cycloaddition Reactions of Azide-Terminated Monolayers on Silica," *J. Phys. Chem. B*, vol. 108, no. 13, pp. 3963–3966, 2004.

[128] M. Ried, "Photoschaltbare Moleküle auf Oberflächen," Dissertation Kiel University, 2012.

[129] M. D. Holz, "Versuche zur photoschaltbaren Zelladhäsion auf Oberflächen," Dissertation Kiel University, 2014.

[130] L. F. Kadem, M. Holz, K. G. Suana, Q. Li, C. Lamprecht, R. Herges, and C. Selhuber-Unkel, "Rapid Reversible Photoswitching of Integrin-Mediated Adhesion at the Single-Cell Level," *Adv. Mater.*, vol. 28, no. 9, pp. 1799–1802, 2016.

[131] M. Rivara, M. K. Patel, L. Amori, and V. Zuliani, "Inhibition of Na V1.6 sodium channel currents by a novel series of 1,4-disubstituted-triazole derivatives obtained via copper-catalyzed click chemistry," *Bioorganic Med. Chem. Lett.*, vol. 22, no. 20, pp. 6401–6404, 2012.

[132] H. S. Lim, W. H. Lee, S. G. Lee, D. Lee, S. Jeon, and K. Cho, "Effect of nanostructure on the surface dipole moment of photoreversibly tunable superhydrophobic surfaces.," *Chem. Commun. (Camb).*, vol. 46, no. 24, pp. 4336–4338, 2010.

[133] K. Stadtherr, H. Wolf, and P. Lindner, "An aptamer-based protein biochip," *Anal. Chem.*, vol. 77, no. 11, pp. 3437–3443, 2005.

[134] J. Groten, C. Bunte, and J. Rühe, "Light-Induced Switching of Surfaces at Wetting Transitions through Photoisomerization of Polymer Monolayers," *Langmuir*, vol. 28, no. 42, pp. 15038–15046, Oct. 2012.

[135] A. Solga, Z. Cerman, B. F. Striffler, M. Spaeth, and W. Barthlott, "The dream of staying clean: Lotus and biomimetic surfaces," *Bioinspir. Biomim.*, vol. 2, pp. 126–134, 2007.

[136] W. Barthlott, M. Mail, B. Bhushan, and K. Koch, "Plant Surfaces: Structures and Functions for Biomimetic Innovations," *Nano-Micro Lett.*, vol. 9, no. 23, pp. 1–40, 2017.

[137] M. Sun, C. Luo, L. Xu, H. Ji, Q. Ouyang, D. Yu, and Y. Chen, "Artificial lotus leaf by nanocasting," *Langmuir*, vol. 21, no. 19, pp. 8978–8981, 2005.

[138] S. L. Peterson, A. McDonald, P. L. Gourley, and D. Y. Sasaki, "Poly(dimethylsiloxane) thin films as biocompatible coatings for microfluidic devices: Cell culture and flow studies with glial cells," *J. Biomed. Mater. Res. - Part A*, vol. 72, no. 1, pp. 10–18, 2005.

[139] D. Bodas and C. Khan-Malek, "Hydrophilization and hydrophobic recovery of PDMS by oxygen plasma and chemical treatment-An SEM investigation," *Sensors Actuators, B Chem.*, vol. 123, no. 1, pp. 368–373, 2007.

[140] and S. G. S. Bhattacharya, A. Datta, J. M. Berg, "Studies on Surface Wettability of Poly (Dimethyl) Siloxane (PDMS) and Glass Under Oxygen-Plasma," *J.MicroElecMechSys*, vol. 14, no. 3, pp. 590–597, 2005.

[141] N. Wagner and P. Theato, "Light-induced wettability changes on polymer surfaces," *Polymer (Guildf).*, vol. 55, no. 16, pp. 3436–3453, 2014.

[142] E. Mele, D. Pisignano, M. Varda, M. Farsari, G. Filippidis, C. Fotakis, A. Athanassiou, and R. Cingolani, "Smart photochromic gratings with switchable wettability realized by green-light interferometry," *Appl. Phys. Lett.*, vol. 88, no. 20, 2006.

[143] K. Ichimura, "Light-Driven Motion of Liquids on a Photoresponsive Surface," *Science*, vol. 288, no. 5471, pp. 1624–1626, 2000.

[144] S.-K. Oh, M. Nakagawa, and K. Ichimura, "Photocontrol of liquid motion on an azobenzene monolayer," *J. Mater. Chem.*, vol. 12, no. 8, pp. 2262–2269, 2002.

[145] Z. Hua, J. Yang, T. Wang, G. Liu, and G. Zhang, "Transparent surface with reversibly switchable wettability between superhydrophobicity and superhydrophilicity," *Langmuir*, vol. 29, no. 33, pp. 10307–10312, 2013.

[146] C. Kallweit, M. Bremer, D. Smazna, T. Karrock, R. Adelung, and M. Gerken, "Photoresponsive hierarchical ZnO-PDMS surfaces with azobenzene-polydopamine coated nanoparticles for reversible wettability tuning Keywords," *Submitt. to Vaccuum*, pp. 1–34, 2017.

[147] S. Schwarzer, D. Ingwersen, R. Herges, and I. Parchmann, "Schüler schalten chemisch," *Nachrichten aus der Chemie*, vol. 62, no. 4, pp. 491–493, 2014.

[148] D. Ingwersen, "Untersuchung von 1',3'-Dihydro-1',3',3'-trimethyl-6-nitrospiro-[2H-1- benzopyran-2,2'-[2H]indol]-funktionalisierten Rußoberflächen hinsichtlich ihrer Photoschaltbarkeit," Bachelor Thesis Kiel University, 2013.

[149] R. Wizinger and H. Wenning, "Über intramolekulare Ionisation," *Helv. Chim. Acta*, vol. 23, no. 1, pp. 247–271, 1940.

[150] C. F. Koelsch and W. R. Workman, "Some Thermochromic Spirans," *J. Am. Chem. Soc.*, vol. 74, no. 24, pp. 6288–6289, 1952.

[151] T. R. Silvia, V. S. L. Ana, and E. a. S. González, "Novel Syntheses of Spiropyran Photochromatic Compounds Using Ultrasound," *Synth. Commun.*, vol. 25, no. 1, pp. 105–110, 1995.

[152] A. R. Jang, E. K. Jeon, D. Kang, G. Kim, B. S. Kim, D. J. Kang, and H. S. Shin, "Reversibly light-modulated Dirac point of graphene functionalized with spiropyran," *ACS Nano*, vol. 6, no. 10, pp. 9207–9213, 2012.

[153] A. Setaro, P. Bluemmel, C. Maity, S. Hecht, and S. Reich, "Non-covalent functionalization of individual nanotubes with spiropyran-based molecular switches," *Adv. Funct. Mater.*, vol. 22, no. 11, pp. 2425–2431, 2012.

[154] Y. Yang, P. Cohn, S.-H. Eom, K. a. Abboud, R. K. Castellano, and J. Xue, "Ultraviolet-violet electroluminescence from highly fluorescent purines," *J. Mater. Chem. C*, vol. 1, no. 16, p. 2867, 2013.

[155] N. Cocherel, C. Poriel, J. Rault-Berthelot, F. Barrière, N. Audebrand, A. M. Z. Slawin, and L. Vignau, "New 3pi-2spiro ladder-type phenylene materials: synthesis, physicochemical properties and applications in OLEDs.," *Chemistry*, vol. 14, no. 36, pp. 11328–11342, 2008.

[156] X. Zhou, Y. Niu, F. Huang, M. S. Liu, A. K. Jen, R. V January, V. Re, M. Recei, and V. March, "Highly Efficient UV - Violet Light-Emitting Polymers Derived from Fluorene and Tetraphenylsilane Derivatives®: Molecular Design toward Enhanced Electroluminescent Performance," *Macromolecules*, vol. 40, no. iii, pp. 3015–3020, 2007.

[157] T.-G. Kim, H.-S. Oh, Y.-H. Kim, and W.-Y. Kim, "Study of Deep Blue Organic

Light-Emitting Diodes Using Doped BCzVBi with Various Blue Host Materials," *Trans. Electr. Electron. Mater.*, vol. 11, no. 2, pp. 85–88, 2010.

[158] B. M. Lee, H. H. Yu, Y. H. Kim, N. H. Kim, J. A. Yoon, W. Y. Kim, and P. Mascher, "Highly efficient blue organic light-emitting diodes using dual emissive layers with host-dopant system," *J. Photonics Energy*, vol. 3, p. 33598, 2013.

[159] M. T. Greiner, M. G. Helander, W. M. Tang, Z. B. Wang, J. Qiu, and Z. H. Lu, "Universal energy-level alignment of molecules on metal oxides," *Nat. Mater.*, vol. 11, no. 1, pp. 76–81, 2011.

[160] T. Matsushima, G. H. Jin, and H. Murata, "Marked improvement in electroluminescence characteristics of organic light-emitting diodes using an ultrathin hole-injection layer of molybdenum oxide," *J. Appl. Phys.*, vol. 104, no. 5, 2008.

[161] T. Matsushima, G.-H. Jin, Y. Kanai, T. Yokota, S. Kitada, T. Kishi, and H. Murata, "Interfacial charge transfer and charge generation in organic electronic devices," *Org. Electron.*, vol. 12, no. 3, pp. 520–528, 2011.

[162] X. Yu, T. J. Marks, and A. Facchetti, "Metal oxides for optoelectronic applications," *Nat. Mater.*, vol. 15, no. 4, pp. 383–396, 2016.

[163] H. You, Y. Dai, Z. Zhang, and D. Ma, "Improved performances of organic light-emitting diodes with metal oxide as anode buffer," *J. Appl. Phys.*, vol. 101, no. 2, pp. 3–6, 2007.

[164] T. Furukawa, H. Nakanotani, M. Inoue, and C. Adachi, "Dual enhancement of electroluminescence efficiency and operational stability by rapid upconversion of triplet excitons in OLEDs," *Sci. Rep.*, vol. 5, p. 8429, 2015.

[165] H. Nakanotani, T. Higuchi, T. Furukawa, K. Masui, K. Morimoto, M. Numata, H. Tanaka, Y. Sagara, T. Yasuda, and C. Adachi, "High-efficiency organic light-emitting diodes with fluorescent emitters," *Nat. Commun.*, vol. 5, no. May, p. 4016, 2014.

[166] M. Kim, S. K. Jeon, S. H. Hwang, and J. Y. Lee, "Stable blue thermally activated delayed fluorescent organic light-emitting diodes with three times longer

lifetime than phosphorescent organic light-emitting diodes," *Adv. Mater.*, vol. 27, no. 15, pp. 2515–2520, 2015.

[167] S. Möller and S. R. Forrest, "Improved light out-coupling in organic light emitting diodes employing ordered microlens arrays," *J. Appl. Phys.*, vol. 91, no. 5, pp. 3324–3327, 2002.

[168] M.-K. Wei, I.-L. Su, Y.-J. Chen, M. Chang, H.-Y. Lin, and T.-C. Wu, "The influence of a microlens array on planar organic light-emitting devices," *J. Micromechanics Microengineering*, vol. 16, no. 2, pp. 368–374, 2006.

[169] J. Zhou, N. Ai, L. Wang, H. Zheng, C. Luo, Z. Jiang, S. Yu, Y. Cao, and J. Wang, "Roughening the white OLED substrate's surface through sandblasting to improve the external quantum efficiency," *Org. Electron. physics, Mater. Appl.*, vol. 12, no. 4, pp. 648–653, 2011.

[170] B. Riedel, J. Hauss, U. Geyer, J. Guetlein, U. Lemmer, and M. Gerken, "Enhancing outcoupling efficiency of indium-tin-oxide-free organic light-emitting diodes via nanostructured high index layers," *Appl. Phys. Lett.*, vol. 96, no. 24, pp. 2008–2011, 2010.

[171] Z. B. Wang, M. G. Helander, J. Qiu, D. P. Puzzo, M. T. Greiner, Z. M. Hudson, S. Wang, Z. W. Liu, and Z. H. Lu, "Unlocking the full potential of organic light-emitting diodes on flexible plastic," *Nat. Photonics*, vol. 5, no. 12, pp. 753–757, 2011.

[172] T. Bocksrocker, N. Hülsmann, C. Eschenbaum, A. Pargner, S. Höfle, F. Maier-Flaig, and U. Lemmer, "Highly efficient fully flexible indium tin oxide free organic light emitting diodes fabricated directly on barrier-foil," *Thin Solid Films*, vol. 542, pp. 306–309, 2013.

[173] S. Lenk, T. Schwab, S. Schubert, L. Müller-Meskamp, K. Leo, M. C. Gather, and S. Reineke, "White organic light-emitting diodes with 4 nm metal electrode," *Appl. Phys. Lett.*, vol. 107, no. 16, pp. 1–5, 2015.

[174] Y. K. Mishra, S. Kaps, A. Schuchardt, I. Paulowicz, X. Jin, D. Gedamu, S. Freitag, M. Claus, S. Wille, A. Kovalev, S. N. Gorb, and R. Adelung, "Fabrication of

macroscopically flexible and highly porous 3D semiconductor networks from interpenetrating nanostructures by a simple flame transport approach," *Part. Part. Syst. Charact.*, vol. 30, no. 9, pp. 775–783, 2013.

[175] Y. K. Mishra, G. Modi, V. Cretu, V. Postica, O. Lupan, T. Reimer, I. Paulowicz, V. Hrkac, W. Benecke, L. Kienle, and R. Adelung, "Direct Growth of Freestanding ZnO Tetrapod Networks for Multifunctional Applications in Photocatalysis, UV Photodetection, and Gas Sensing," *ACS Appl. Mater. Interfaces*, vol. 7, no. 26, pp. 14303–14316, 2015.

[176] L. Xu, Y. L. Hu, C. Pelligra, C. H. Chen, L. Jin, H. Huang, S. Sithambaram, M. Aindow, R. Joesten, and S. L. Suib, "ZnO with different morphologies synthesized by solvothermal methods for enhanced photocatalytic activity," *Chem. Mater.*, vol. 21, no. 13, pp. 2875–2885, 2009.

[177] M. Bremer, A. Cojocaru, I. Hölken, I. Paulowicz, M. Köpke, R. Adelung, H. Schmidt-Niepenberg, and M. Gerken, "Tetrapodal ZnO Particles for Substrate Mode Scattering in Flexible Organic Light-Emitting Diodes," in *Light, Energy and the Environment*, 2016, p. JW4A.8.

[178] I. Hölken, M. Hoppe, Y. K. Mishra, S. N. Gorb, R. Adelung, and M. Baum, "Complex shaped ZnO nano-and microstructure based polymer composites: mechanically stable and environmentally friendly coatings for potential antifouling applications," *Phys. Chem. Chem. Phys.*, vol. 122, pp. 50–58, 2016.

[179] K. Jäger, O. Isabella, R. A. C. M. M. van Swaaij, and M. Zeman, "Angular resolved scattering measurements of nano-textured substrates in a broad wavelength range," *Meas. Sci. Technol.*, vol. 22, no. 10, p. 105601, 2011.

[180] P. A. Van Nijnatten, "An automated directional reflectance/transmittance analyser for coating analysis," *Thin Solid Films*, vol. 442, no. 1–2, pp. 74–79, 2003.

[181] B. R. Stevenson, "The LEDs Dark Secret," pp. 1–8, 2014.

[182] Y. C. Shen, G. O. Mueller, S. Watanabe, N. F. Gardner, A. Munkholm, and M. R. Krames, "Auger recombination in InGaN measured by photoluminescence," *Appl. Phys. Lett.*, vol. 91, no. 14, pp. 10–11, 2007.

[183] C. Murawski, K. Leo, and M. C. Gather, "Efficiency roll-off in organic light-emitting diodes," *Adv. Mater.*, vol. 25, no. 47, pp. 6801–6827, 2013.

[184] H.-H. Huang, S.-Y. Chu, P.-C. Kao, Y.-C. Chen, M.-R. Yang, and Z.-L. Tseng, "Enhancement of hole-injection and power efficiency of organic light emitting devices using an ultra-thin ZnO buffer layer," *J. Alloys Compd.*, vol. 479, no. 1–2, pp. 520–524, 2009.

[185] X. Jiang, F. L. Wong, M. K. Fung, and S. T. Lee, "Aluminum-doped zinc oxide films as transparent conductive electrode for organic light-emitting devices," *Appl. Phys. Lett.*, vol. 83, no. 9, pp. 1875–1877, 2003.

[186] B. Riedel, Y. Shen, J. Hauss, M. Aichholz, X. Tang, U. Lemmer, and M. Gerken, "Tailored highly transparent composite hole-injection layer consisting of pedot:PSS and SiO 2 nanoparticles for efficient polymer light-emitting diodes," *Adv. Mater.*, vol. 23, no. 6, pp. 740–745, 2011.

[187] J. Hauss, T. Bocksrocker, B. Riedel, U. Geyer, U. Lemmer, and M. Gerken, "Metallic Bragg-gratings for light management in organic light-emitting devices," *Appl. Phys. Lett.*, vol. 99, no. 10, pp. 5–8, 2011.

[188] J. Hauss, B. Riedel, S. Gleiss, U. Geyer, U. Lemmer, and M. Gerken, "Periodic nanostructuring for guided mode extraction in organic light-emitting diodes," *J. Photonics Energy*, vol. 1, no. 1, pp. 11012–11019, 2011.

[189] U. Geyer, J. Hauss, B. Riedel, S. Gleiss, U. Lemmer, and M. Gerken, "Large-scale patterning of indium tin oxide electrodes for guided mode extraction from organic light-emitting diodes," *J. Appl. Phys.*, vol. 104, no. 9, pp. 1–5, 2008.

[190] Y. Qu, M. Slootsky, and S. R. Forrest, "Enhanced light extraction from organic light-emitting devices using a sub-anode grid," *Nat. Photonics*, vol. 9, no. 11, pp. 758–763, 2015.

[191] Christian Kluge, "Nanostructures for emission control in organic light-emitting layers," Dissertation Kiel University, 2014.

[192] K. Saxena, V. K. Jain, and D. S. Mehta, "A review on the light extraction techniques in organic electroluminescent devices," *Opt. Mater. (Amst).*, vol. 32,

no. 1, pp. 221–233, 2009.

[193] H. Lim, G. Kim, K. B. Choi, M. Jeong, J. Ryu, and J. Lee, "Nanoimprint lithography with a soft roller and focused UV light for flexible substrates," *Microelectron. Eng.*, vol. 98, pp. 279–283, 2012.

[194] S. H. Ahn and L. J. Guo, "High-speed roll-to-roll nanoimprint lithography on flexible plastic substrates," *Adv. Mater.*, vol. 20, no. 11, pp. 2044–2049, 2008.

[195] C. C. Yu and H. L. Chen, "Nanoimprint technology for patterning functional materials and its applications," *Microelectron. Eng.*, vol. 132, pp. 98–119, 2015.

[196] C. Kluge, "Nanostructures for emission control in organic light-emitting layers," Dissertation Kiel University, 2014.

[197] T. Karrock and M. Gerken, "Pressure sensor based on flexible photonic crystal membrane," *Biomed. Opt. Express*, vol. 6, no. 12, pp. 392–399, 2014.

[198] G. A. Turnbull, P. Andrew, W. L. Barnes, and I. D. W. Samuel, "Photonic mode dispersion of a two-dimensional distributed feedback polymer laser," pp. 1–8, 2003.

[199] H. Lüder, M. Bremer, and M. Gerken, "Simulation of nanostructured emission layers for tailoring the angular radiation pattern of OLEDs," in *ICEAA to be published*, 2017.

[200] A. Pradana and M. Gerken, "Photonic crystal slabs in flexible organic light-emitting diodes," *Photon. Res.*, vol. 3, no. 2, pp. 32–37, 2015.

[201] A. Pradana, C. Kluge, and M. Gerken, "Tailoring the refractive index of nanoimprint resist by blending with TiO_2 nanoparticles," *Opt. Mater. Express*, vol. 4, no. 2, p. 329, 2014.

[202] M. Yao and J. Fang, "Hydrophilic PEO-PDMS for microfluidic applications," *J. Micromechanics Microengineering*, vol. 22, p. 25012, 2012.

[203] C. Kluge, M. Rädler, A. Pradana, M. Bremer, P.-J. Jakobs, N. Barié, M. Guttmann, and M. Gerken, "Extraction of guided modes from organic emission layers by compound binary gratings," *Optics Letters*, vol. 37, no. 13. p. 2646, 2012.

[204] R. Rosario, D. Gust, M. Hayes, F. Jahnke, J. Springer, and A. A. Garcia, "Photon-

modulated wettability changes on spiropyran-coated surfaces," *Langmuir*, vol. 18, no. 21, pp. 8062–8069, 2002.

[205] A. Athanassiou, M. I. Lygeraki, D. Pisignano, K. Lakiotaki, M. Varda, E. Mele, C. Fotakis, R. Cingolani, and S. H. Anastasiadis, "Photocontrolled variations in the wetting capability of photochromic polymers enhanced by surface nanostructuring," *Langmuir*, vol. 22, no. 5, pp. 2329–2333, 2006.

[206] S. Samanta and J. Locklin, "Formation of Photochromic Spiropyran Polymer Brushes via Surface-Initiated , Ring-Opening Metathesis Polymerization©: Reversible Photocontrol of Wetting Behavior and Solvent Dependent Morphology Changes," *Langmuir*, no. 16, pp. 9558–9565, 2008.

[207] R. Rosario, D. Gust, A. a. Garcia, M. Hayes, J. L. Taraci, T. Clement, J. W. Dailey, and S. T. Picraux, "Lotus effect amplifies light-induced contact angle switching," *J. Phys. Chem. B*, vol. 108, no. 34, pp. 12640–12642, 2004.

List of figures

Abbreviations

BS	Beam splitter
CA	Contact angle
e. g.	For example
EBL	Electron blocking layer
EL	Electroluminescence
EQE	External quantum efficiency
etc.	And so on
ETL	Electron transport layer
eV	Electron Volt
FDTD	Finite difference time domain
FRET	Förster resonant energy transfer
HBL	Hole blocking layer
HOMO	Highest occupied molecular orbital
HTL	Hole transport layer
IQE	Internal quantum efficiency
ISC	Inter system crossing
LED	Light-emitting diode
LUMO	Lowest unoccupied molecular orbital
ND	Neutral density (filter)
NIL	Nano imprint lithography
NP	Nanoparticle
OLED	Organic light-emitting diode
PC	Photonic crystal
PD	Photodiode
PL	Photoluminescence

RISC	Reverse inter system crossing
rpm	Rotations per minute
SAM	Self-assembled molecule
sccm	Standard cubic centimeters
SEM	Scanning electron microscope
SMU	Source measurement unit
SP	Short pass
SPP	Surface plasmon polariton
TADF	Thermally activated delayed fluorescence
TE	Transversal electric
TM	Transversal magnetic
UV	Ultraviolet
VIS	Visible

Materials

Abbr.	Name	Supplier
Ag	Silver	Kurt J. Lesker
Al	Aluminum	Kurt J. Lesker
Alq_3	Tris(8-hydroxyquinoline)aluminium	Sigma Aldrich
Amonil	Amonil MMS4 photoresist	Amo GmbH
Amoprime	Primer to Amonil	Amo GmbH
APTES	(3-Aminopropyl)triethoxysilane	Sigma Aldrich
Au	Gold	Kurt J. Lesker
BCP	Bathacuproin,2,9-Dimethyl-4,7-diphenyl-1,10-phenanthroline	Sigma Aldrich
BCzVBi	4,4′-Bis(9-ethyl-3-carbazovinylene)-1,1′-biphenyl	BOC-Sciences
BPhen	Bathophenanthroline	Sigma Aldrich
DCzTrz	9,9'-(5-(4,6-Diphenyl-1,3,5-triazin-2-yl)-1,3-phenylene)bis(9H-carbazole)	Lumtec
DMF	Dimethylformamide	Sigma Aldrich
DMSO	Dimethyl sulfoxide, normal and anhydrous	Sigma Aldrich
DPEPO	Bis[2-(diphenylphosphino)phenyl]ether oxide	Lumtec
DPVBi	4,4′-Bis(2,2-diphenylvinyl)-1,1′-biphenyl	BOC-Sciences
FC-4430	Fluorosurfactant	3M Germany
ITO	Indium tin oxide (sputtered on glass)	PGO
LiF	Lithium fluoride	Sigma Aldrich
mCBP	3,3'-Di(9H-carbazol-9-yl)-1,1'-biphenyl	TCI
$MgCl_2$	Magnesium chloride	Sigma Aldrich
MoO_3	Molybdenum(VI) oxide	Sigma Aldrich
NaCl	Sodium chloride	Sigma Aldrich

NPB	N,N′-Di-[(1-naphthyl)-N,N′-diphenyl]-1,1′-biphenyl)-4,4′-diamine	Sigma Aldrich, Lumtec
OCF_3-AZO	(4-pent-4-ynyloxy-phenyl)-(4-trifluoromethoxy-phenyl)-diazene	ChiroBlock GmbH (special synthesis)
PDC	1,4-Phenylene Diisothiocyanat	Sigma Aldrich
PDMS	Polydimethylsiloxane; Sylgard 184	Dow Corning
PDMS-PEO	poly(dimethylsiloxane)-b-poly(ethylene oxide)	Polysciences
PEDOT:PSS	Poly(3,4-ethylenedioxythiophene)poly(styrenesulfonate)	Sigma Aldrich
PMMA	Polymethyl methacrylate	Polymer Source
SiO	Silicon monoxide	Kurt J. Lesker
Super Yellow	PDY-132	Merck
TAZ	3-(Biphenyl-4-yl)-5-(4-tert-butylphenyl)-4-phenyl-4H-1,2,4-triazole	Sigma Aldrich
TEOS	Tetraethyl orthosilicate	Sigma Aldrich
TiO_2 NP	Titanium dioxide nanoparticle (in Xylene)	Sigma Aldrich
ZnO NP	Zinc oxide nanoparticles (in H_2O)	Sigma Aldrich
-	11-bromoundecyltrichlorosilane	ABCR GmbH
-	2-[4-(4-trifluoromethoxy phenylazo) phenoxy]ethanamine	Squarix (special synthesis)
-	2-hydroxy-5-methylbenzaldehyde	Sigma Aldrich
-	2-methylene-1,3,3-trimethylindoline	Sigma Aldrich
-	3-phenyl-1-propyne	Sigma Aldrich
-	(4‘-Hexyl-phenyl)-[4(propyl-butoxy)-phenyl]-diazene (ether-2).	Squarix GmbH (special synthesis)
-	Acetone	Roth, Merck

-	Aqueous ammonia solition, 28 %	VWR
-	Copper(II)-sulfate-pentahydrate	Sigma Aldrich
-	Ethanol	Roth
-	Glutaraldehyde	Sigma Aldrich
-	Isopropanol	Roth
-	Methanol	Sigma Aldrich
-	Sodium ascorbate	Sigma Aldrich
-	Sodium azide	Sigma Aldrich
-	Sodium hydrogen phosphate	Sigma Aldrich
-	Toluene, normal and anhydrous	Sigma Aldrich

Appendix A

Flowcharts

A1. Azobenzene coupling with „click chemistry"

#	**Process step**	**Parameters**
1	Clean	Ultrasonic bath 5 min acetone, 5 min isopropanol
2	Oxygen plasma treatment	30 s 50 W 8 sccm O_2
3	Silanization	In glovebox 25 mL toluene + 0,125 mL 11-bromoundecyltrichlorosilane, Incubation time: 30 min
4	Purge	2x with dry toluene, 1x with standard toluene
5	Clean	Leave for 10 min each in toluene and in DMSO
6	Preparation of saturated sodium azide solution	Give one spoon of sodium azide into 150 mL tried DMSO; stir for 30 min to 55 min at 400 rpm
7	Azide introduction	Decant azide-saturated DMSO into lockable glass vessel; put in samples; close and leave it for two days at room temperature
8	Clean	Ultrasonic bath 5 min DMSO, 5 min double distilled water, 5 min isopropanol

9	Preparation of sulotion with azobenzene and alkyne	6.8 mg (4-pent-4-ynyloxy-phenyl)-(4-trifluoromethoxy-phenyl)-diazene + 2.5 μL 3-Phenyl-1-propyne + 22 mL ethanol
10	Preparation Copper(II) sulfate-sodium ascorbate solution	30 mg copper(II)-sulfate-pentahydrate + 30 mg sodium ascorbate + 3 mL double distilled water
11	„Click“	Put samples into small glass vessels with all of the azobenzene solution + 800 μL Copper(II) sulfate sodium ascorbate solution, Close and stir with 200 rpm at room temperature for two days
12	Clean	Ultrasonic bath 9 min ethanol, 9 min acetone, 9 min isopropanol, 30 min double dist. H_2O

A2. Azobenzene coupling to surface with APTES and glutaraldehyde

#	**Process step**	**Parameters**
1	Oxygen plasma treatment	30 s 50 W 8 sccm O_2
2	Clean	In glovebox 5 min in ethanol, 5 min in methanol
3	Preparation silanization solution	In glovebox methanol: 24.75 mL + APTES: 0.260 mL
4	Silanization – Incubation of substrates in solution	In glovebox 60 min at room temperature
5	Cleaning	In glovebox 3x washing with methanol (with 5 mL syringe)
6	Dry	In glovebox 30 min at 110 °C on hotplate, 1 min cooling
7	Crosslinker- Preparation	25ml DI-water + 2,5 mL 25 % Glutaraldehyde solution + 0,0355 g (= 100 mM) Na_2HPO_4 + 0,219 g (= 150 mM) NaCl
8	Crosslinker – Incubation of substrates in solution	Under fume hood, 1 h at room temperature
9	Clean	With 0,25L PBS solution (one pellet PBS + 0,095 g/L (= 1 mM) $MgCl_2$)
10	Dry	15 min at room temperature
11	Preparation of azobenzene solution	13 mg 2-[4-(4-trifluoromethoxy phenylazo) phenoxy]ethanamine + 22 mL ethanol
12	Azobenzene coupling to substrate	Over night in closed small glass vessel

13	Clean	1x ethanol, 1x isopropanol, 1x DI-water; each in ultrasonic bath

A3. Fabricating PDMS copies of a lotus leaf

#	**Process step**	**Parameters**
1	Leaf preparation	Put Teflon frame on leaf, cut leaf around it, Use strong adhesive tape to make sure the PDMS cannot leave the frame
2	Mixing Polydimethylsiloxane (PDMS)	Sylgard 184 + Curing Agent, 10:1 20 min in IKA Tube Drive Pour PDMS on leaf
3	Outgassing	Evacuate for 10 min in vacuum
4	Curing	2 days at room temperature, Cut negative lotus leaf afterwards
5	Gold evaporation	5 nm on PDMS
6	Prepare form for positive copy	Mark negative lotus PDMS on the back , put Teflon form on negative leaf copy
7	PDMS filling	Pour little amount of PDMS inside form
8	Outgassing	Evacuate for 30 min to 45 min in vacuum until all bubbles disappeared
9	PDMS curing	1.5 h to 2 h at 90 °C, Cut edges of PDMS, separate positive from negative lotus PDMS

Appendix B

Photoluminescence experiments on simplified OLED stacks

1 Variation of emitter position

In stack with fixed height – Silver electrode, no grating

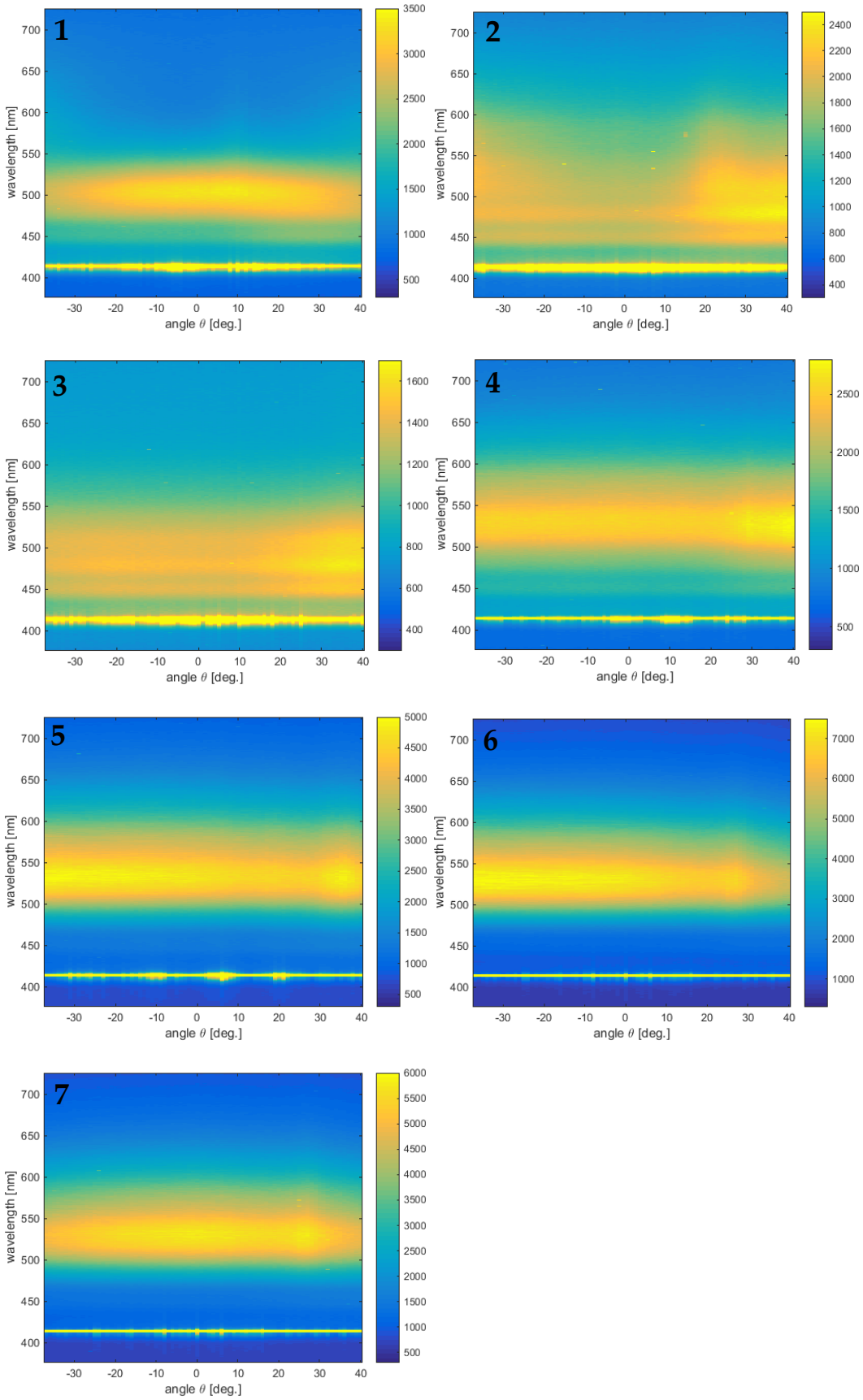

2 Variation of emitter position

In stack with fixed height – Silver electrode, grating period: 350 nm

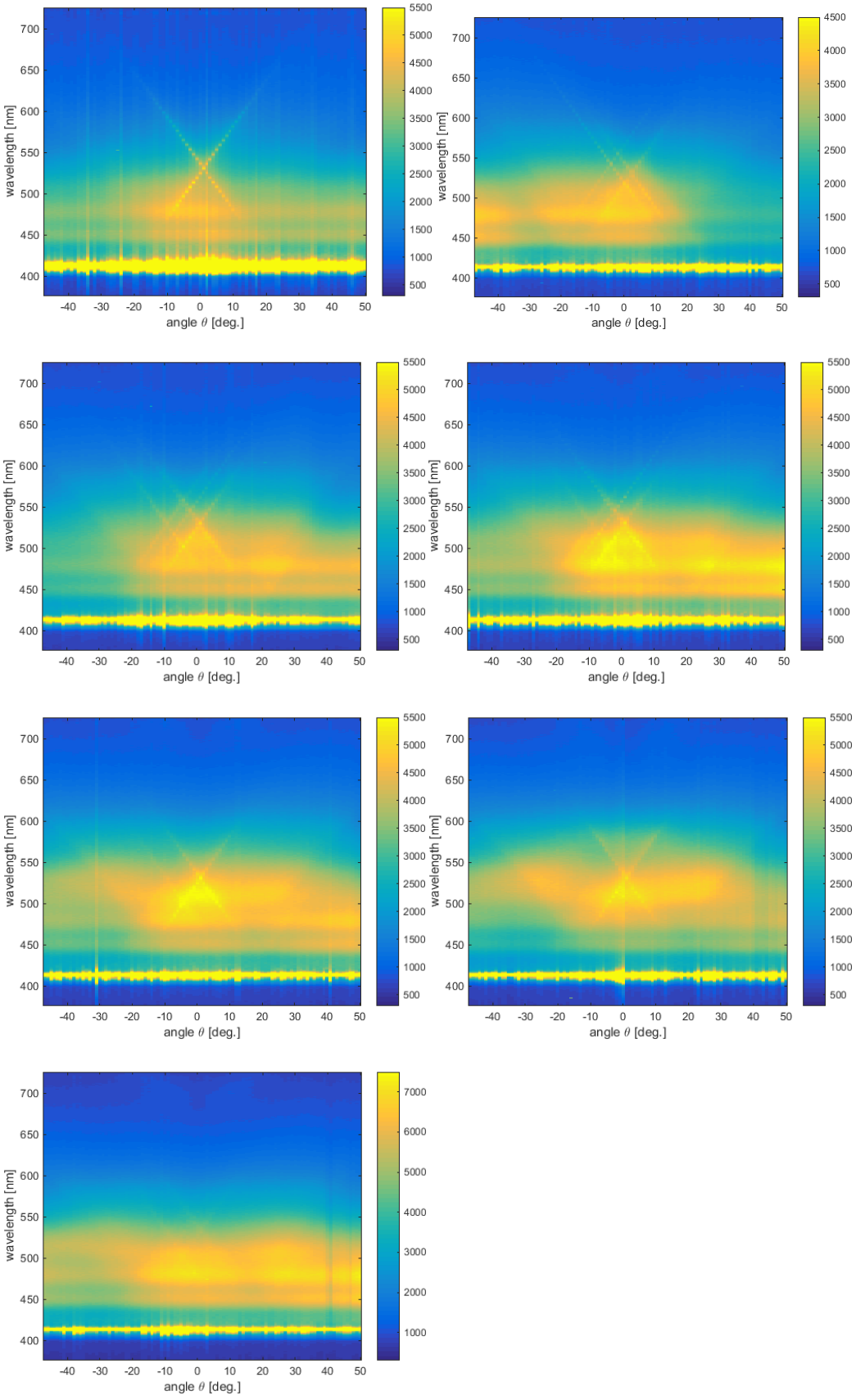

3 Variation of emitter position

Stack with fixed height – Ag, grating: 350 nm, luminescence of epoxy subtracted

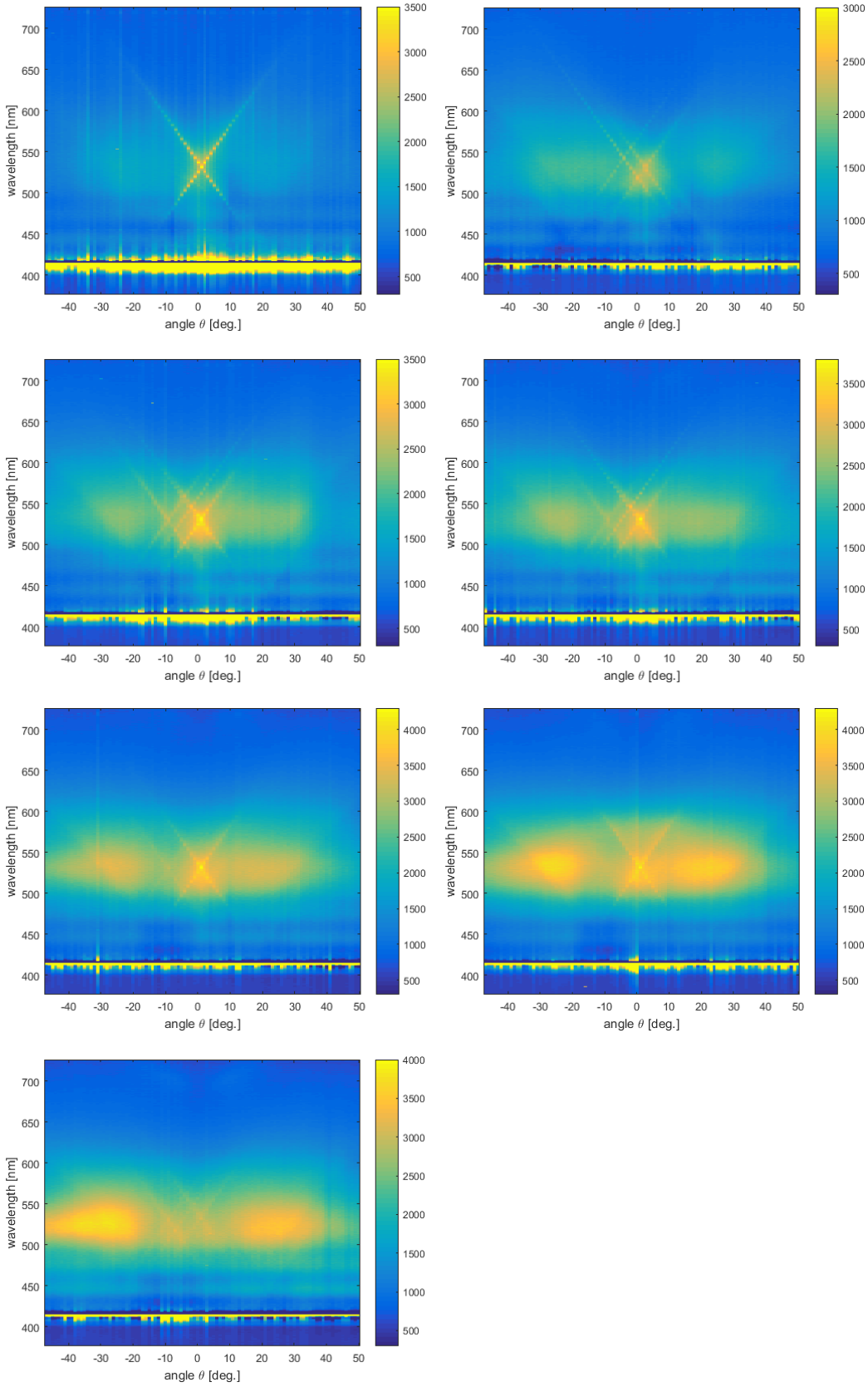

4 Variation of emitter position

In stack with fixed height – Silver electrode, grating period: 350 nm, rotated

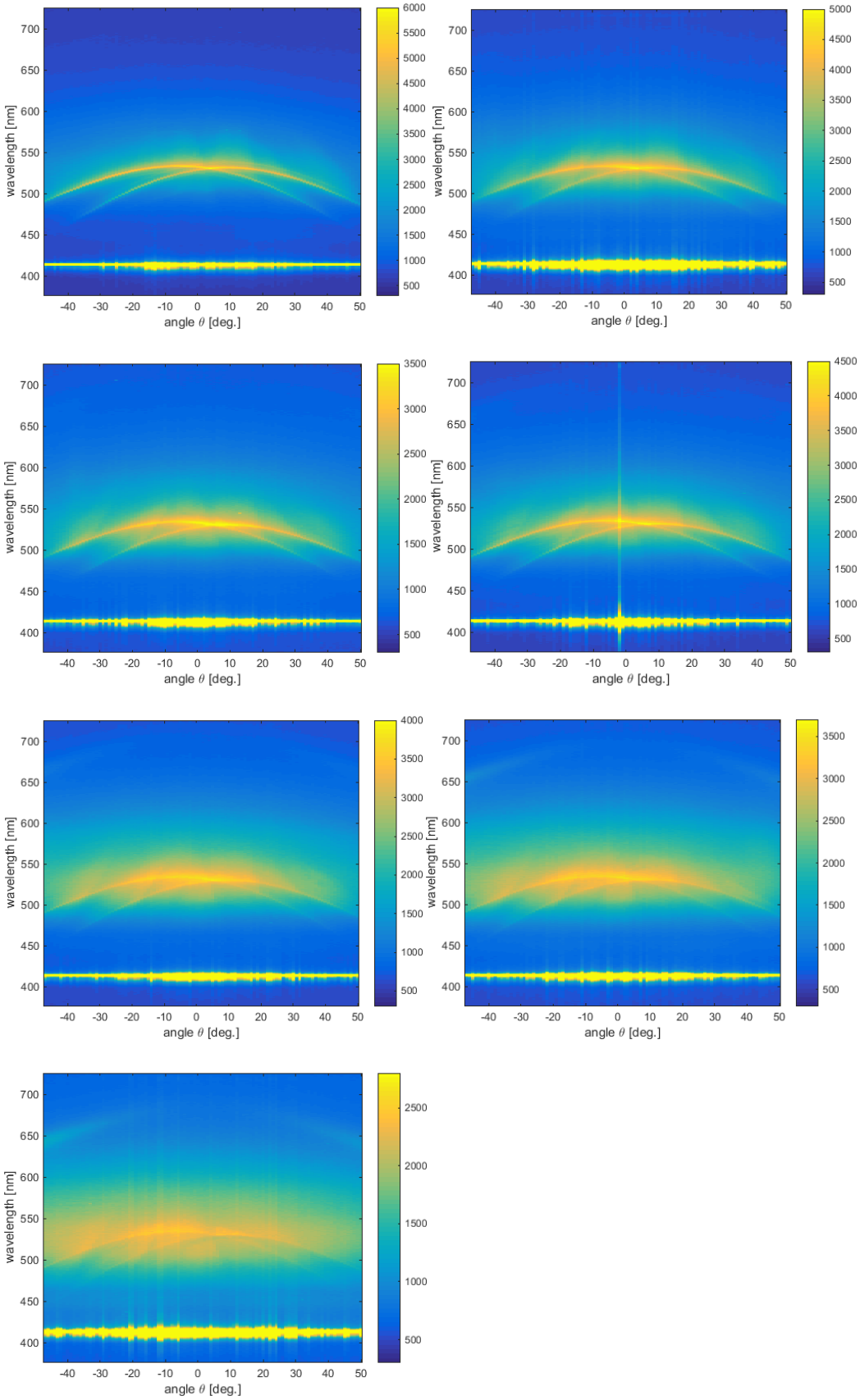

5 Variation of emitter position

In stack with fixed height – Aluminum electrode, no grating

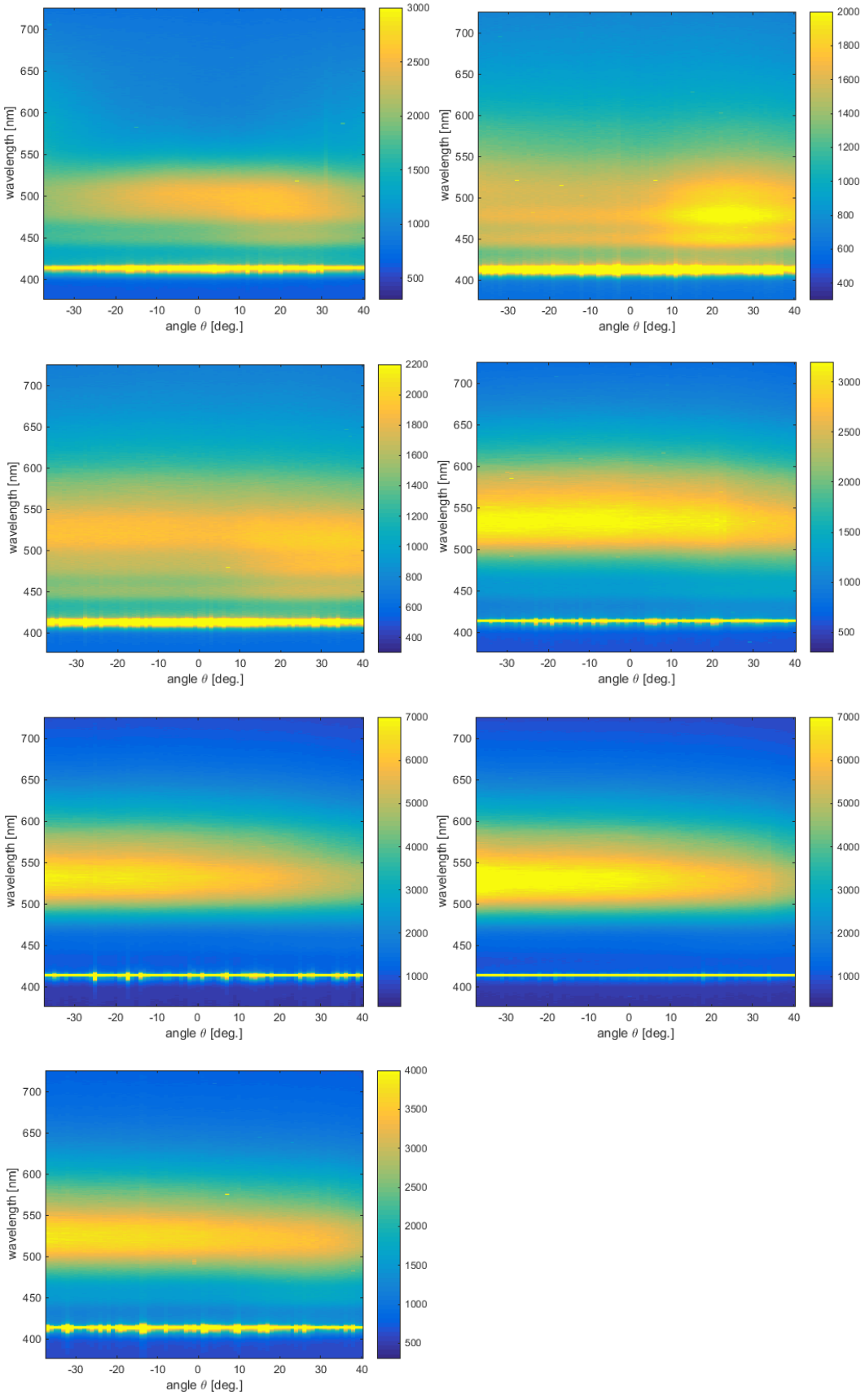

6 Variation of emitter position

In stack with fixed height – Aluminum electrode, grating period: 350 nm

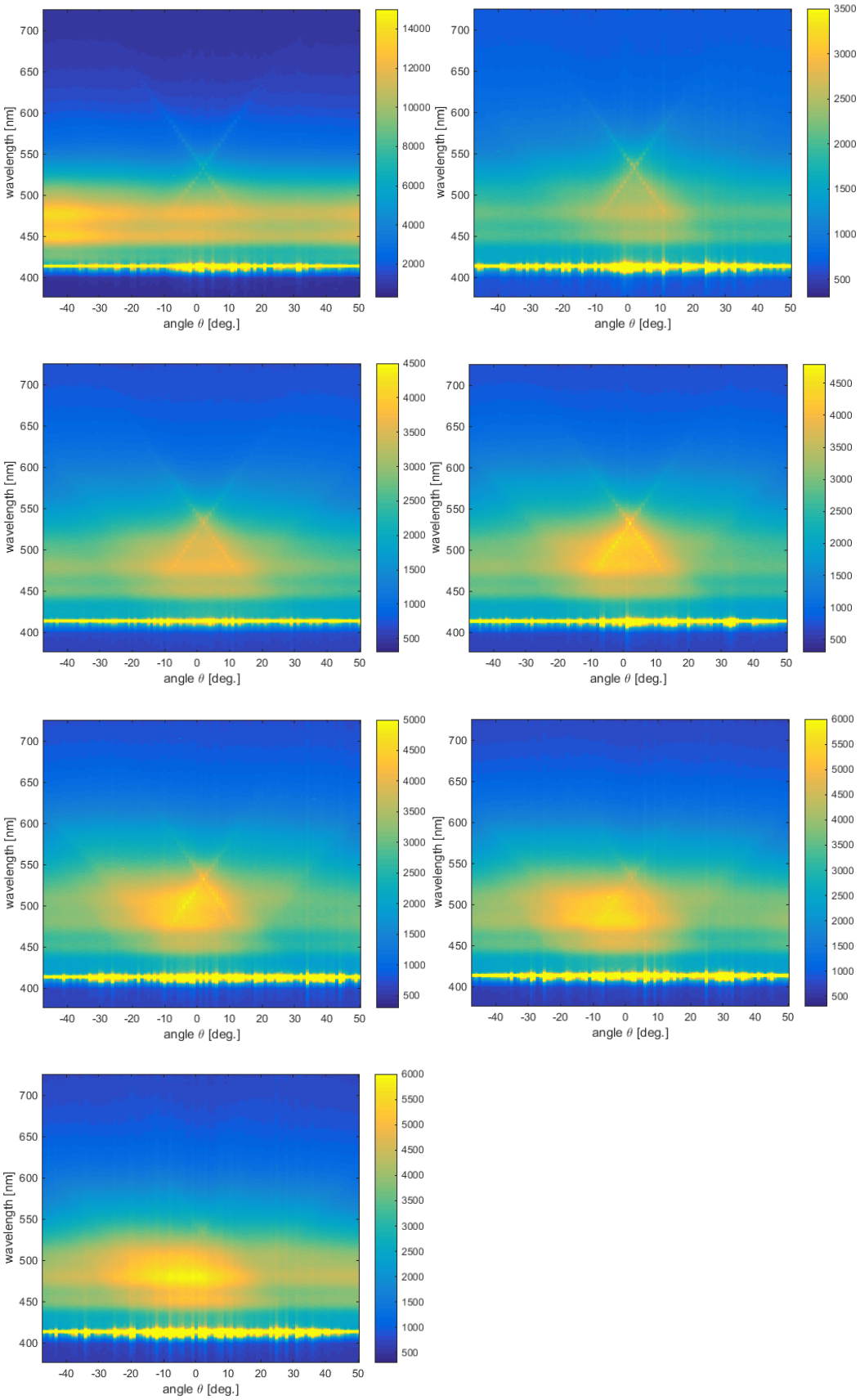

7 Variation of emitter position

In stack with fixed height – Aluminum electrode, grating period: 350 nm, rotated

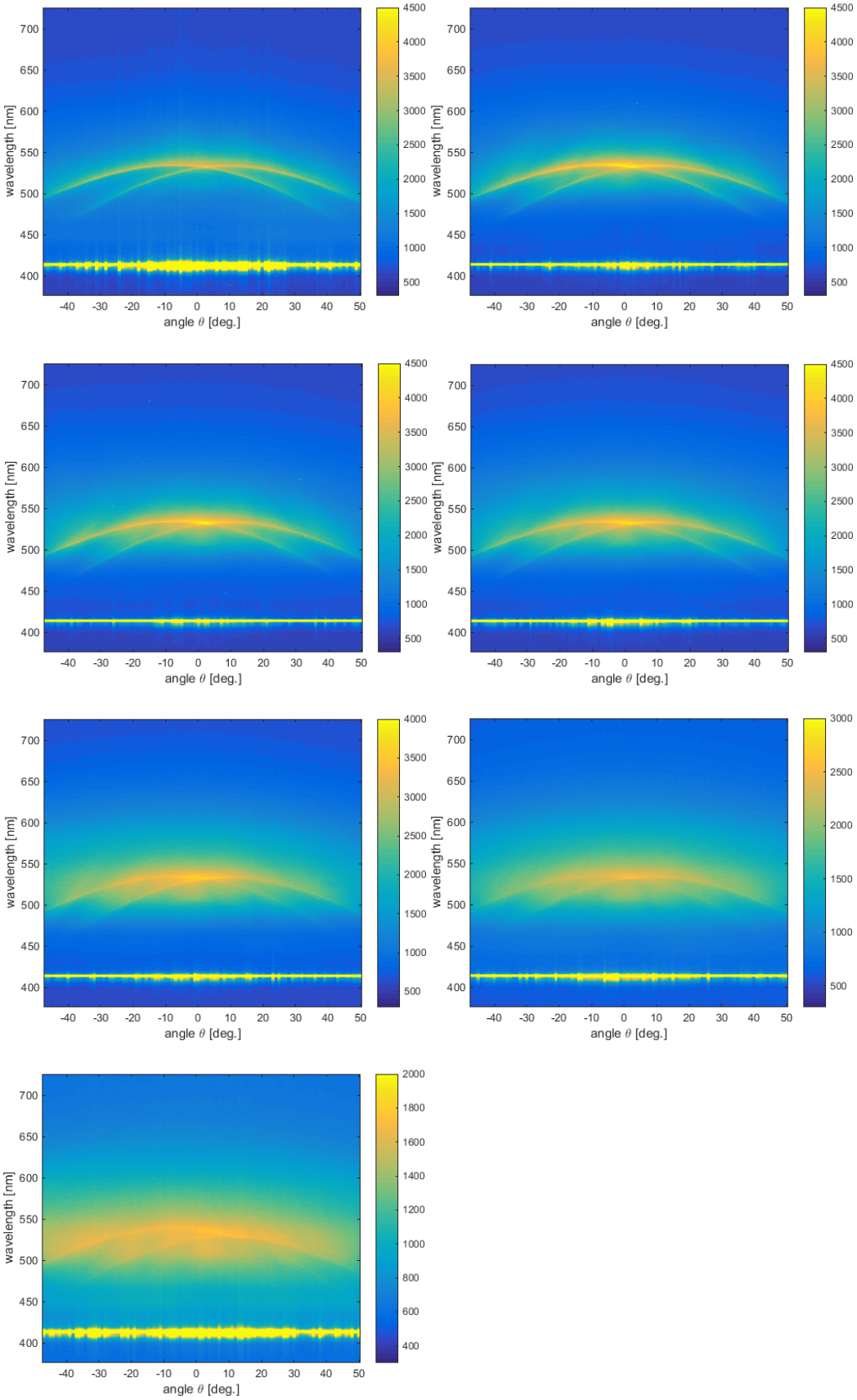

8 Distance variation between substrate and emitter

Aluminum electrode, no grating

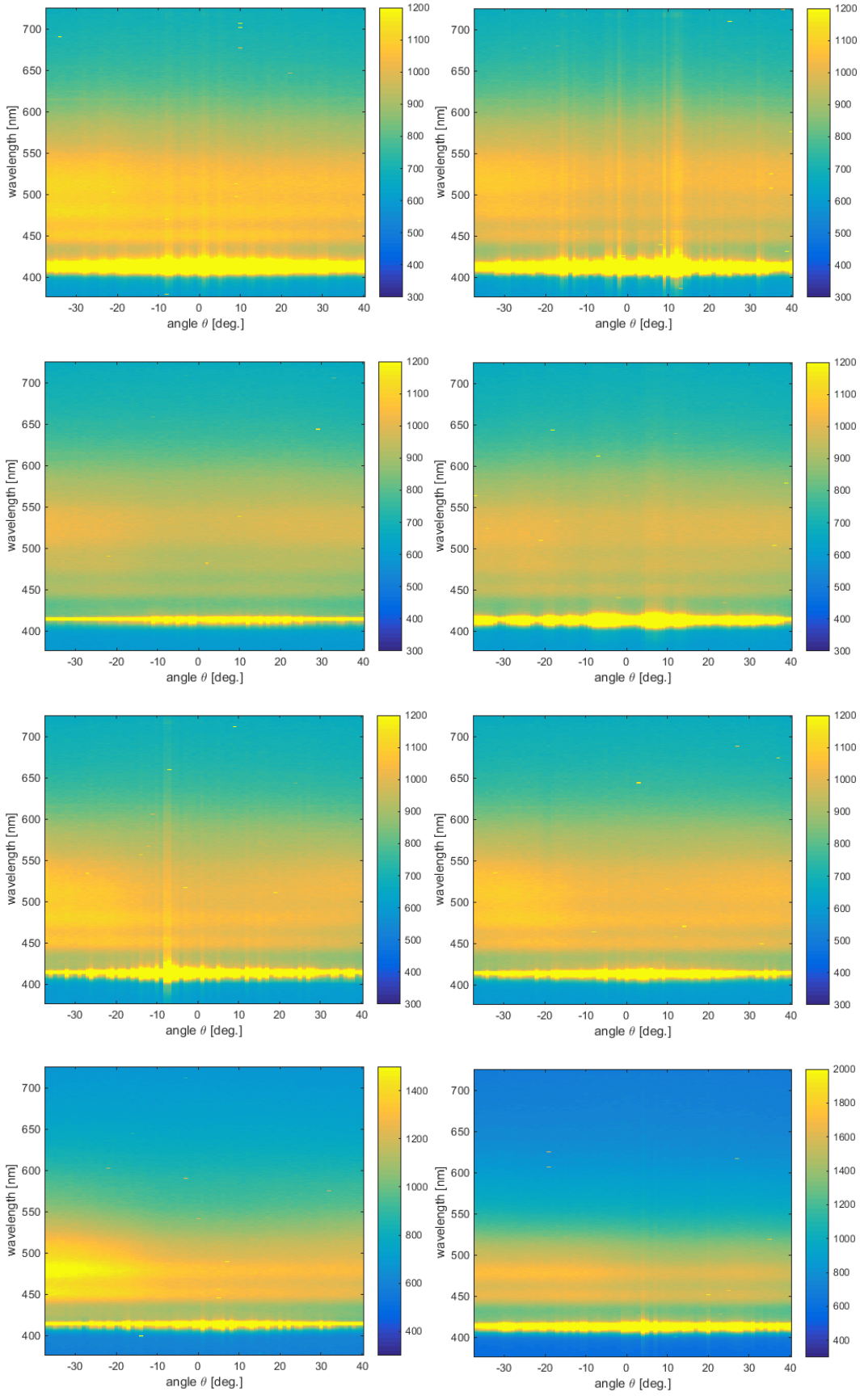

9 Distance variation between substrate and emitter

Aluminum electrode, grating period: 350 nm

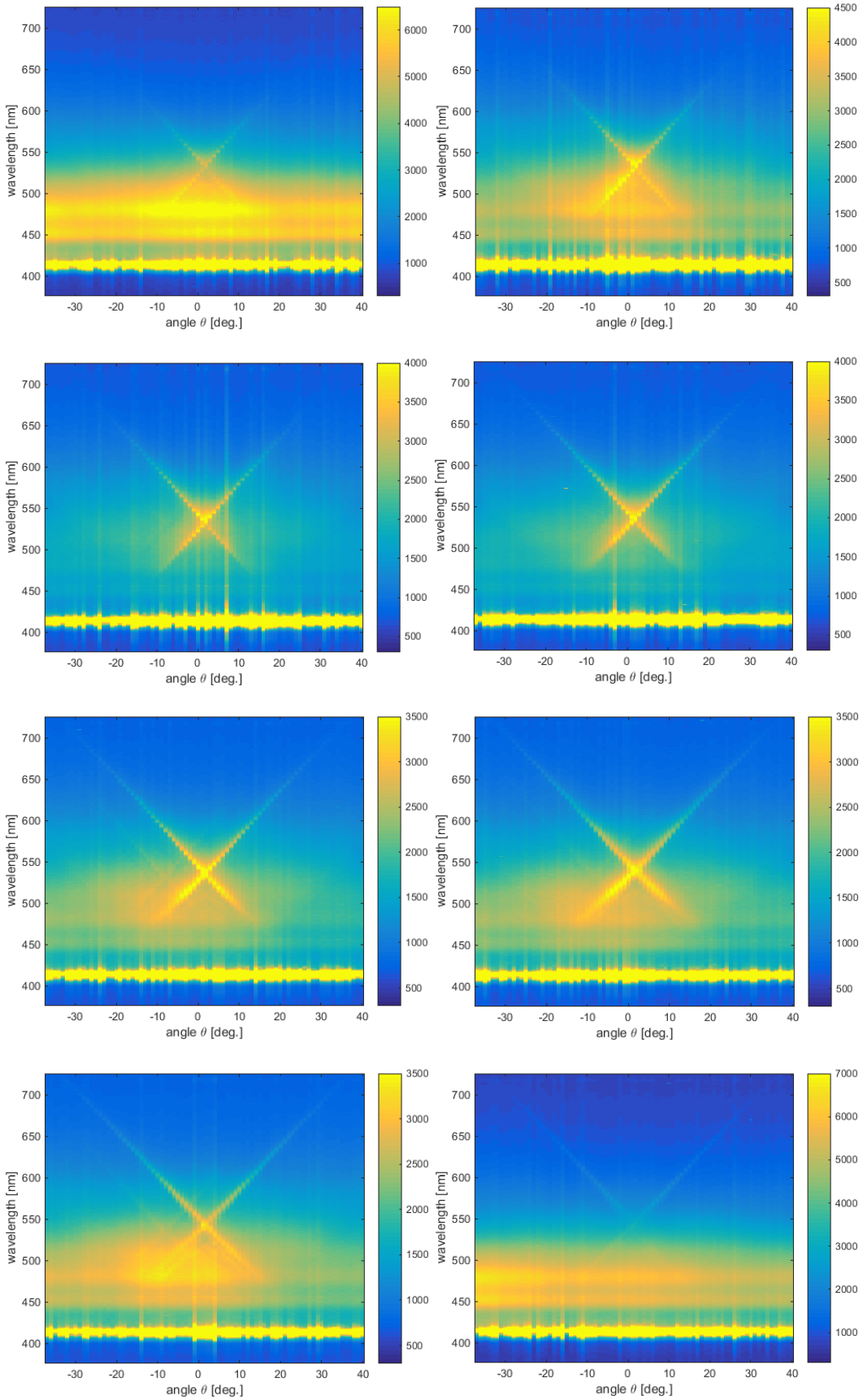

10 Distance variation between substrate and emitter

Aluminum electrode, grating period: 350 nm, turned

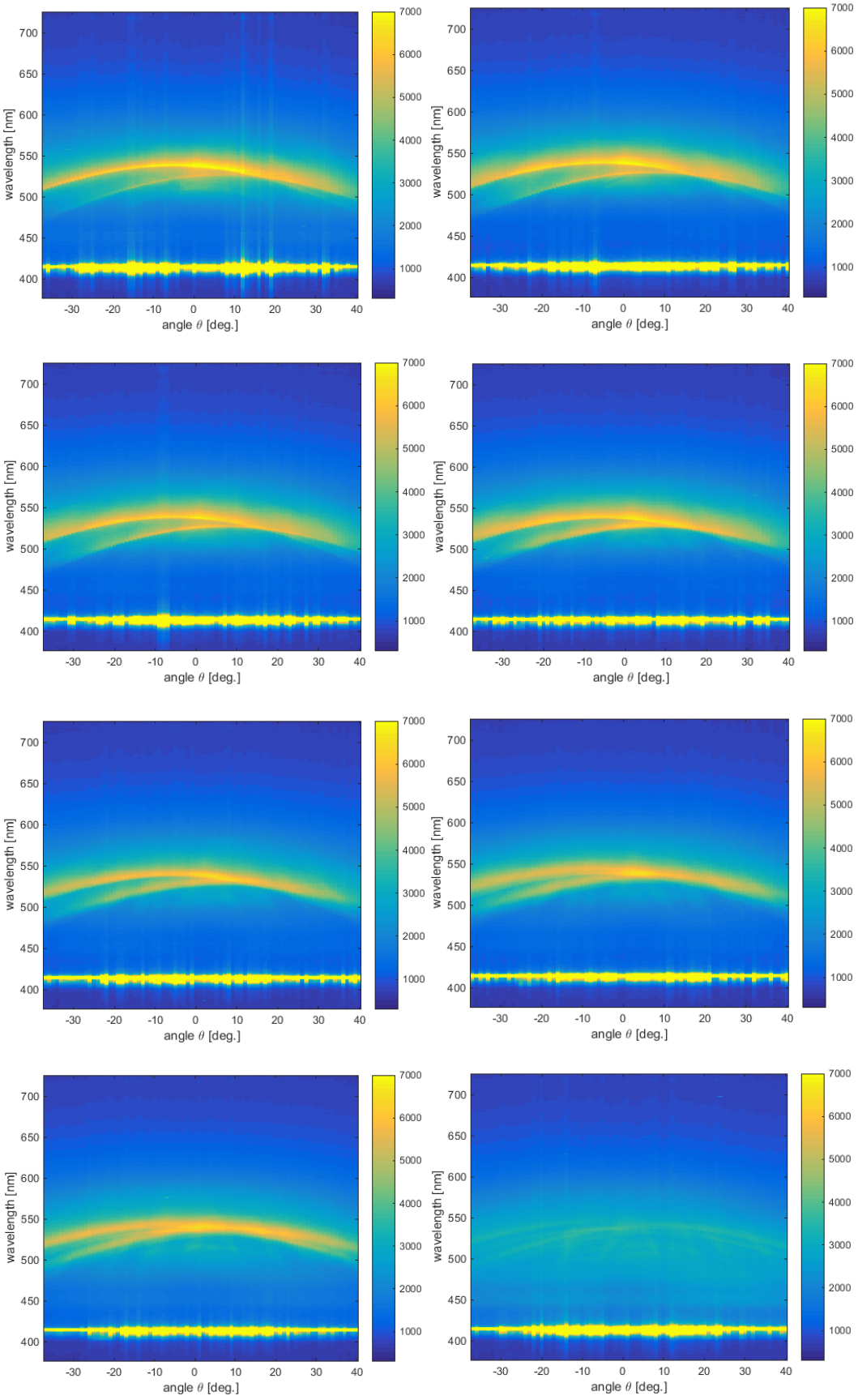

11 Variation of electrode thickness

Emitter position fixed – Silver electrode, no grating

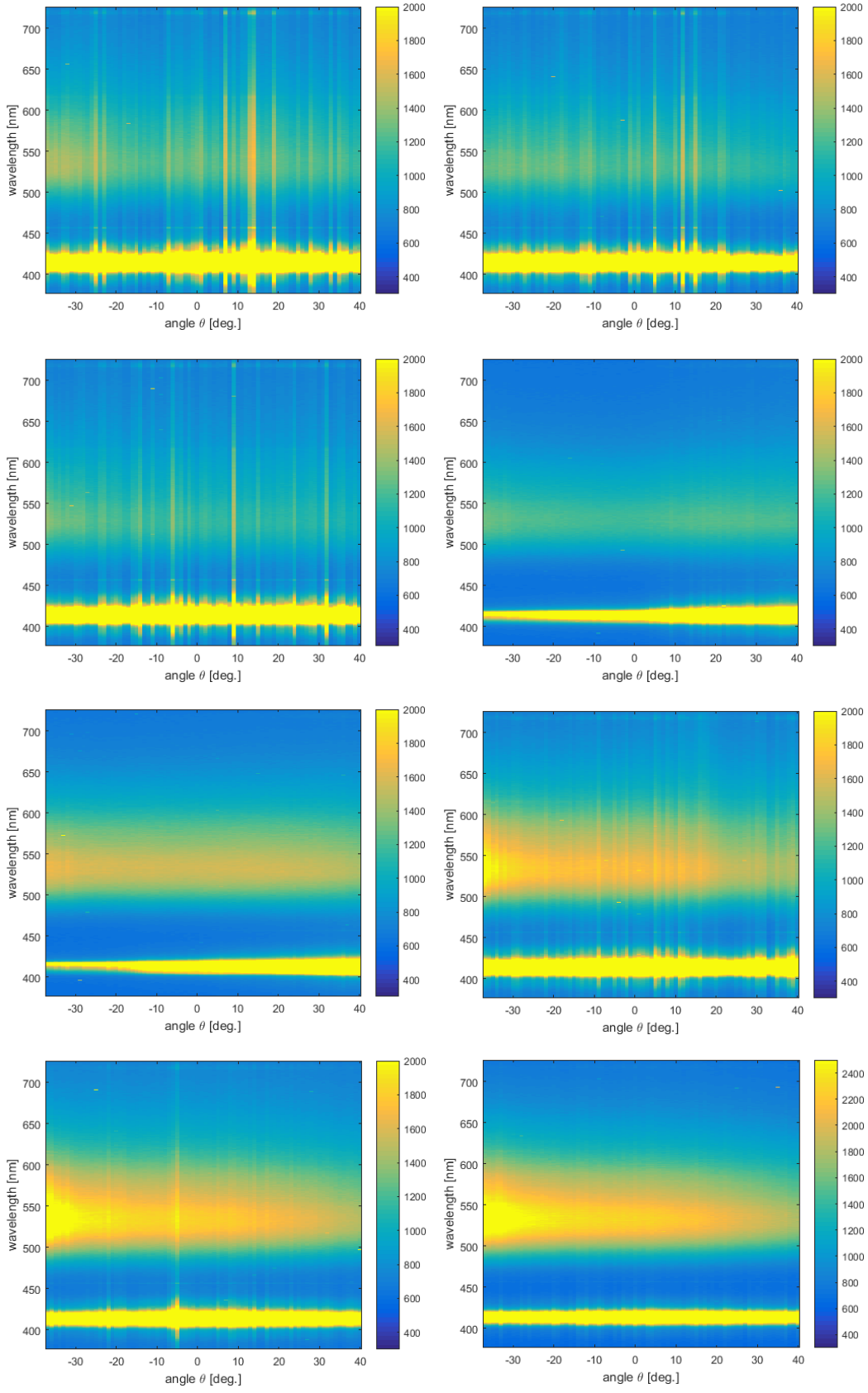

12 Variation of electrode thickness

Emitter position fixed – Silver electrode, grating period: 350 nm

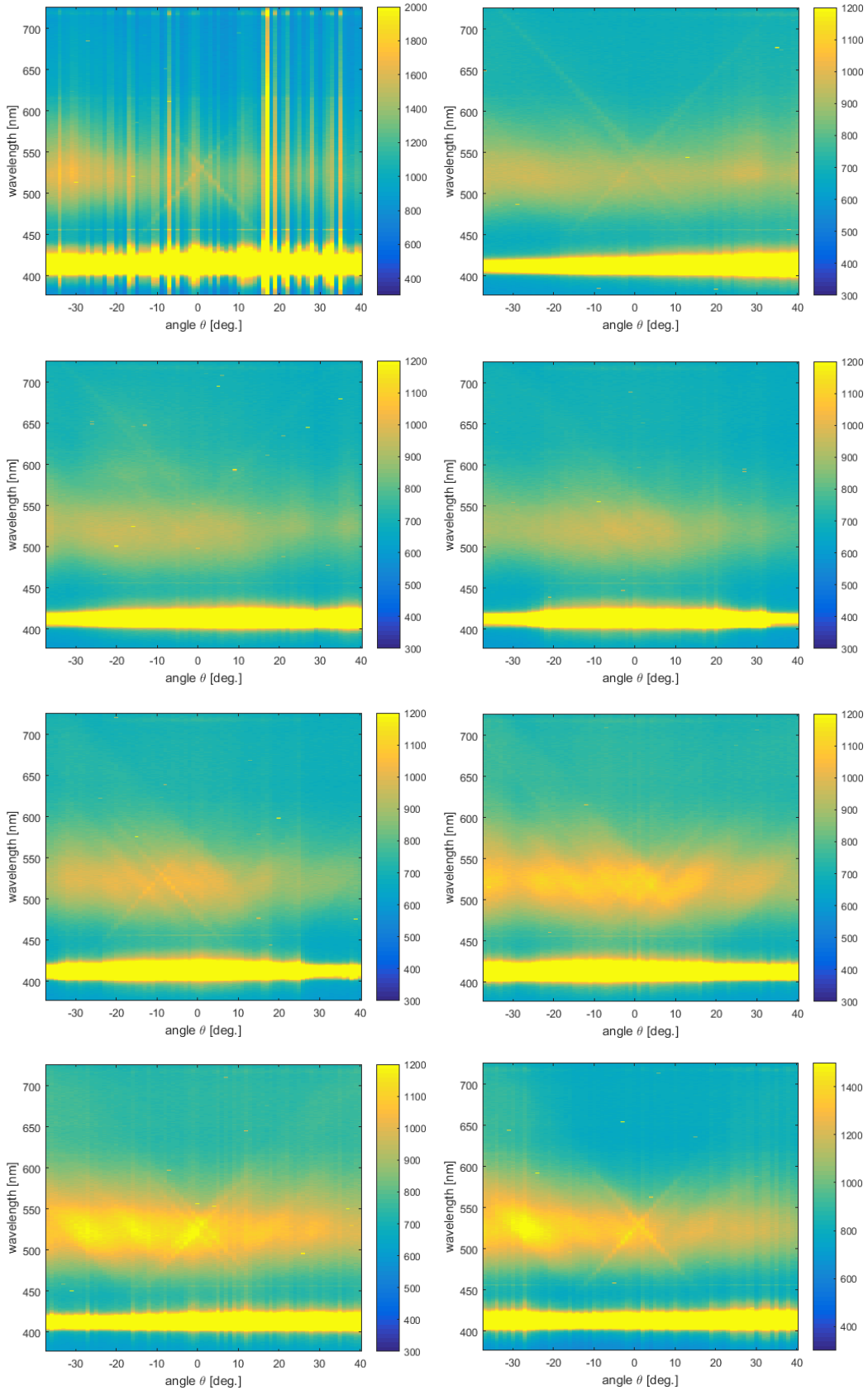

13 Variation of electrode thickness

Emitter position fixed – Silver electrode, grating period: 350 nm, turned